Audible Noise Reduction in the High Frequency Injection based Sensorless Torque Control for EPS Applications

Hui Jiang, MSc.

Thesis submitted to the University of Nottingham

for the degree of Doctor of Philosophy

March 2012

To my dear wife,my parents,parents in law

for their full support to my study and life in the UK

Acknowledgements

I would like to express my most sincere gratitude to my supervisor Prof. Mark Sumner for his persistent support and enlightening guidance throughout this research.

I am also very thankful to all the friends and colleagues that I have worked with in the Power Electronics, Machines and Control Group for their support, discussion, help and kindness.

Finally, I would like to express my appreciation to the external examiner, Prof. Chris Bingham, from the University of Lincoln, UK, and the internal examiner, Prof. Greg Asher, for their advice to the corrections to this thesis.

Abstract

This thesis has investigated the reduction of audible noise in low speed sensorless controlled drives for automotive electrical power steering (EPS) applications. The specific methods considered employ saliency tracking high frequency (*hf*) voltage injection in the machine's estimated d axis. In terms of the audible noise reduction, a novel random sinusoidal *hf* injection sensorless method has been proposed. The perceived audible noise due to the *hf* injection can be reduced by randomly distributing the injection frequencies around a centre frequency, such that it is perceived as a background hiss rather than the fixed tone heard with fixed *hf* injection methods. By analysing the A-weighting scales used to classify human perception of audible noise and frequency analysis of the recorded noise, an injection frequency of (1500±328) Hz is found to have the lowest audible noise level compared to other random frequencies and other fixed frequencies methods. A 10 kHz square wave *hf* injection sensorless method has also been implemented. The frequency analysis of the recorded audible noise indicates that it also may be lower than for the fixed *hf* sinusoidal injection. In terms of control performance, sensorless torque control for these methods has been achieved from zero speed to ±240rpm with up to ±60A load (about 63% rated load). Similar position estimate quality has been demonstrated. Dynamic performance for a step change in torque current demand and for a speed reversal has been performed, and the random injection method with (1500±328) Hz frequency has been found to be able to control a step change in torque demand current of 50A whilst for the 10 kHz square wave injection method only a 40A step change can be achieved. On the other hand, the average position error after the speed transient has settled is less for the 10 kHz square ewave injection than for the random injection.

List of Contents

List of Figures

List of Tables

Nomenclature

$\wedge$	The symbol (hat) denotes an estimated value
$*$	Supercript which denotes a reference value
$\_$	Underscore which denotes a vector
$\frac{d}{dt}, p$	The symbols denote a derivation function
P	The pole pair number of the machine
$\underline{\psi}_s^{ref}, \underline{\psi}_s^{adp}$	The stator flux linkage vector obtained from the reference model and from the adaptive model respectively
$\underline{\psi}_{dq}$	The flux vector in the d-q rotor reference frame
ψ_m, ψ_{ad} and ψ_{aq}	The magnet flux, the d and q axis armature current induced flux
i_a, i_b and i_c	The three-phase stator phase currents
$\underline{i}_{\alpha\beta}$	Stator current vector in the stationary α-β frame
$\underline{i}_{\alpha\beta h}$	The high frequency carrier current vector in the stationary α-β frame
$\underline{i}_{dq}$	Stator current vector in the rotating d-q frame
$\underline{i}_{dqh}$	The high frequency carrier current vector in the rotating d-q frame
$\hat{\underline{i}}_{\delta\gamma h}$	The high frequency carrier current vector in the estimated saliency reference frame
$\underline{i}_{\delta\gamma}^m$	The high frequency current vector in the measurement δ^m-γ^m frame
v_a, v_b and v_c	The three-phase stator phase voltages
$\underline{v}_{\alpha\beta}$	Stator voltage vector in the stationary α-β frame
$\underline{v}_{\alpha\beta h}$	The high frequency carrier voltage vector in the stationary α-β frame

$\underline{v}_{dq}$	Stator voltage vector in the rotating *d-q* frame
$\underline{v}_{dqh}$	The high frequency carrier voltage vector in the rotating *d-q* frame
$\hat{\underline{v}}_{\delta\gamma h}$	The high frequency carrier voltage vector in the estimated saliency reference frame
e_a, e_b and e_c	The three-phase stator phase back-EMFs
r_s	The stator phase resistor
L_d, L_q	*d* and *q* axis stator self-inductances
L_{dq}	*d-q* axis mutual inductance
L_s	Average inductance in the saliency frame
ΔL_s	Incremental inductance in the saliency frame
$\Delta L_s^{'}$	Incremental inductance accounting for the cross-coupling effect in the saliency frame
l_a, l_b and l_c	The stator phase inductances
θ_r	The electrical rotor position
$\hat{\theta}_r$	The estimated electrical rotor position
θ_δ	The saliency position
$\hat{\theta}_\delta$	The estimated saliency position
$\Delta\hat{\theta}_\delta$	The angle difference between the real and the estimated saliency position
ω_r	The electrical rotor speed
$\hat{\omega}_r$	The estimated electrical rotor speed
ω_i	The injection angular velocity
T_e^*	The demanded electrical torque

ξ	The error signal to enable the estimation

Chapter 1 Introduction

1.1 Electrically Powered Steering in Automotive applications

Power steering systems are used to provide steering torque assistant to the driver to steer vehicles. It is particularly helpful when the vehicle is running at very slow speed or at standstill.

In Hydraulically Powered Steering systems (HPS) [1], the power is provided by a pump directly connected to the car engine and is delivered to the steering column through the opening and closing of valves in the hydraulic system to provide the torque assistance on the steering rack. One of the most important drawbacks of the HPS system is that since the pump is connected to the engine, hydraulic pressure is constantly produced whenever the engine is running regardless of whether the steering assistance is required, causing a waste in fuel consumption. In addition, the torque assist is proportional to the speed of the hydraulic pump which is controlled by the engine, i.e. is not a variable or independently controllable. Another problem of HPS is that it requires a significant space to mount the hydraulic system, adding extra effort for the design and assembly of the vehicles.

An improved version of the HPS, namely Electric-Hydraulic Powered Steering (EHPS) [2], uses an electrical machine supplied from the car battery and a motor controller rather than the engine to drive the pump, such that the power steering system can be disengaged when assistance is not needed and therefore the system efficiency is improved (up to 5% of fuel saving [3]). However, the hydraulic system is still in place, which means the size of the EHPS remains quite large.

An Electrically Powered Steering (EPS) [4] replaces the pump and the hydraulic system with an electrical machine and coupled via gearing to the steering column to provide the assistance. Therefore, the space for the pump and the pipes with an HPS system is no longer required and a more compact design and a higher efficiency can be achieved. Assistance is provided only when it is required. Also it is controllable and can be varied regardless of the speed of the vehicle. Another advantage is that with proper gearing, when the EPS fails, no additional resistance torque (opposing the motion of the steering) is created. When an HPS is unavailable, e.g. due to failure, a resistance torque is added to the steering by the hydraulic fluid back pressure, making the steering more difficult than if an HPS were not employed.

The main drawback of EPS is that in order to give a high torque for assistance the current needs to be very large due to the small voltage available from the batteries used in vehicles. This limits the application of EPS in large vehicles and shortens the life cycle of the batteries due to frequently high current being drawn from the batteries. To improve the performance, a higher voltage battery or some voltage boost procedure [5] can be used.

1.2 Sensorless control of EPS

The present commercial types of EPS mainly use DC motors and synchronous

PMAC motors. The former one is beneficial for its ease of control and it does not need an additional position sensor. The latter is advantageous as it has a higher power density, longer maintenance cycle (it has no brushes) and higher efficiency compared to the DC motor. The problem with the PMAC motor is that the rotor position needs to be known accurately to apply high performance torque control and adding a position sensor means added cost, reduced reliability due to the fragile position sensor and extra space is required for mounting it. As a result, obtaining the rotor position without a position sensor, namely sensorless control, is attracting interest from the research community [6-20]. Model based sensorless control methods which estimate speed and position from a mathematical model of the motor, have been commercialized in some EHPS systems, where the accuracy of the position signal does not need to be very high, at low and zero speed [10]. However, with the EPS systems, good control performance is needed especially at low and zero speed. Model based methods deteriorate or fail in such situations. Sensorless control methods which aim to track a geometric or magnetic saliency within the machine are now being considered for EPS systems. Saliency tracking methods, such as *hf* injection methods, current derivative methods, which are suitable in low and zero speeds, unfortunately induce extra torque ripple and increase the audible noise emitted by the drive system, making the direct use of these methods undesirable.

1.3 Aims and Objectives of the project

The aim of this research is to further investigate the application of low speed (0-240 rpm) sensorless control methods to a PMAC machine used in EPS systems. The key objectives are:

- To obtain good performance of the sensorless torque control both in steady state and transient conditions, angle error below 15 electrical

degrees in steady states but can be higher in large transients

- To reduce audible noise from the sensorless operation so that a comparable hearing experience can be achieved for the driver with and without a position sensor
- To ensure the current distortion due to sensorless operation is kept low to maintain a high efficiency and low ripple torque
- To achive a system with low cost and ease of implementation; i.e., with minimum sensors, simple control procedures which requires a relatively low power microprocessor (usually a fixed-point processor) and minimum pre-commissioning effort

Previous work at the University of Nottingham [13, 21] compared the high frequency (*hf*) *d-axis* injection method and the current derivative method for low speed control for EPS, including sensorless control performance, torque ripple due to current distortion and the audible noise produced. It was found that the current derivative method has a better position estimate since additional processing for disturbance elimination can be used. However, the *d-axis* method is cheaper and easier to implement, since no additional hardware or software processing effort are needed, and it can be easily used in an existing system. In terms of audible noise, [13] concluded that the current derivative has a better sound experience than *d-axis* method due to its spread of high frequency components. However, neither of these two methods can be applied directly to commercial EPS products as yet. A method combining the advantages of these two methods with minimum side effects needs to be investigated.

This thesis has focused on the reduction of the audible noise, making the realization of a simple, quiet sensorless torque controlled EPS system with good control performance possible.

The following has not been done before:

- A novel random *hf* (high frequency) *d-axis* injection based sensorless control method has been proposed and implemented for the EPS application in this research.
- A square wave type *hf* injection sensorless control method has been applied for EPS applications for the first time.
- The behaviour of these two techniques has been compared in terms of audible noise reduction and sensorless control performance.

1.4 Outlines of the thesis

Chapter 2 gives an overview of the sensorless methods that have been developed for vector controlled AC motors. Chapter 3 highlights the random high frequency sinusoidal *d-axis* injection method and square wave high frequency *d-axis* injection method selected for this research in order to improve the sound experience. Chapter 4 describes the experimental rig with its structure, control platform and the power electronics. Chapter 5 deals with further issues related to the sensorless control including the initial magnet polarity detection and armature reaction effects. Chapter 6 presents the results of the sensorless torque control of the system, comparing the control performance and the sound experience for the methods investigated. Chapter 7 provides the conclusion to the current work and gives suggestions for possible future work. It should be noted that all the results presented in this thesis have been obtained from experiment, and if not specified, all position signals in this thesis are referred to electrical angles.

Chapter 2 Sensorless Vector Control of Permanent Magnet Machines

2.1 Introduction

For industrial application, the vector controlled permanent magnet machine has been widely used due to its high power density and small size compared to other machines of comparable power rating. However, the use of a speed/position sensor mounted onto the shaft of the machine is undesirable for applications where low cost and high reliability is required, which leads to the increasing demands for a high performance position sensorless drive system. In this chapter, various methods of sensorless vector control have been reviewed, and they can be classified into two main categories, namely model based methods and saliency tracking based methods. Details of these methods will be given in the following sections.

2.2 Model of the PM synchronous machine (PMSM)

Field oriented vector control permits a PMSM machine to be controlled as a seperately excited DC machine where the field and torque control are

decoupled so that high dynamic torque response can be obtained.

By making use of the state space theory [22], the individual quantities in a three-phase system can be combined into a single space vector which will be discussed in more details in 4.8 from page 102. In this thesis, a peak stator convention was used for this transformation to preserve the amplitude of the quantities, e.g. a current vector is defined as:

$$\begin{aligned} \underline{i}_s &= \frac{2}{3}(i_a \cdot e^{j0} + i_b \cdot e^{j\frac{2\pi}{3}} + i_c \cdot e^{j\frac{4\pi}{3}}) \\ &= \begin{bmatrix} i_\alpha \\ i_\beta \end{bmatrix} = \begin{bmatrix} i_a \\ \frac{\sqrt{3}}{3}(i_b - i_c) \end{bmatrix} \end{aligned} \tag{2-1}$$

where $\underline{i}_s$ represents the current space vector in a stationary reference frame, i_a, i_b, i_c are the three phase currents, i_α and i_β are the α and β components of the current vector in the stationary α-β frame. Other vectors such as voltage and stator flux linkage vectors can be defined similarly.

To achieve field orientation, the current vector in the stationary frame needs to be rotated by an angle of θ_r which is the electrical rotor position with respect to the positive α axis and the vector in the *d-q* rotating frame can be written as:

$$\underline{i}_{dq} = \underline{i}_{\alpha\beta} \cdot e^{-j\theta_r} \tag{2-2}$$

where $\underline{i}_{dq}$ is the current vector in the rotating *d-q* frame.

Then the dynamic model of the PMSM in a rotating *d-q* frame can be written as:

$$\begin{bmatrix} v_d \\ v_q \end{bmatrix} = \begin{bmatrix} r_s + pL_d & -\omega_r L_q \\ \omega_r L_d & r_s + pL_q \end{bmatrix} \begin{bmatrix} i_d \\ i_q \end{bmatrix} + \psi_m \omega_r \begin{bmatrix} 0 \\ 1 \end{bmatrix} \tag{2-3}$$

where L_d and L_q are the d and q parts of the stator inductance, r_s is the stator resistance, p is the differentiator, ω_r is the electrical speed of the rotor, and ψ_m is the rotor permanent magnet flux.

The developed torque can be written in terms of the rotating variables as [23]:

$$T_e = \frac{3P}{2}[\psi_m i_q + (L_d - L_q) i_d i_q] \tag{2-4}$$

where P is the number of poles of the PMSM.

2.3 Model based sensorless vector control

The method of using a machine's fundamental electrical equations to derive the rotor position and speed is defined as Model based Sensorless Control. It can be classified into the following types.

2.3.1 Model based reference adaptive system method (MRAS)

A MRAS method [8, 19, 24] consists of two models: a reference model which is the voltage model in the stator reference frame and an adaptive model which is the flux model in the rotor reference frame, to generate two estimates for the same vector (usually the stator flux linkage for PM machines), which are defined in (2-5) and (2-6), respectively.

$$\underline{\psi}_s^{ref} = \int (\underline{v}_s - r_s \cdot \underline{i}_s) dt \tag{2-5}$$

$$\underline{\psi}_s^{adp} = (\psi_m + L_d i_d + j L_q i_q) \cdot e^{j\hat{\theta}_r} \tag{2-6}$$

where $\underline{\psi}_s^{ref}$ is the stator flux linkage obtained from the reference model; $\underline{v}_s$ and

$\underline{i}_s$ are the stator voltage and current vectors respectively; r_s is the stator resistor; $\underline{\psi}_s^{adp}$ is the stator flux linkage obtained from the adaptive model; ψ_m is the magnetic flux linkage; L_d and L_q are the dq axis inductances in the estimated rotating reference frame; i_d and i_q are the dq axis currents; $e^{j\hat{\theta}_r}$ is a unit vector which enables the transformation from the estimated rotating reference frame to the stationary reference frame.

A cross product is performed between the two estimates and the result is regarded as an error signal which can drive an adaptation mechanism. The resultant position estimate is then fed back to the adaptive model for tuning the rotor position $\hat{\theta}_r$ to achieve zero estimation error. The schematic of a MRAS is shown in Figure 2.1.

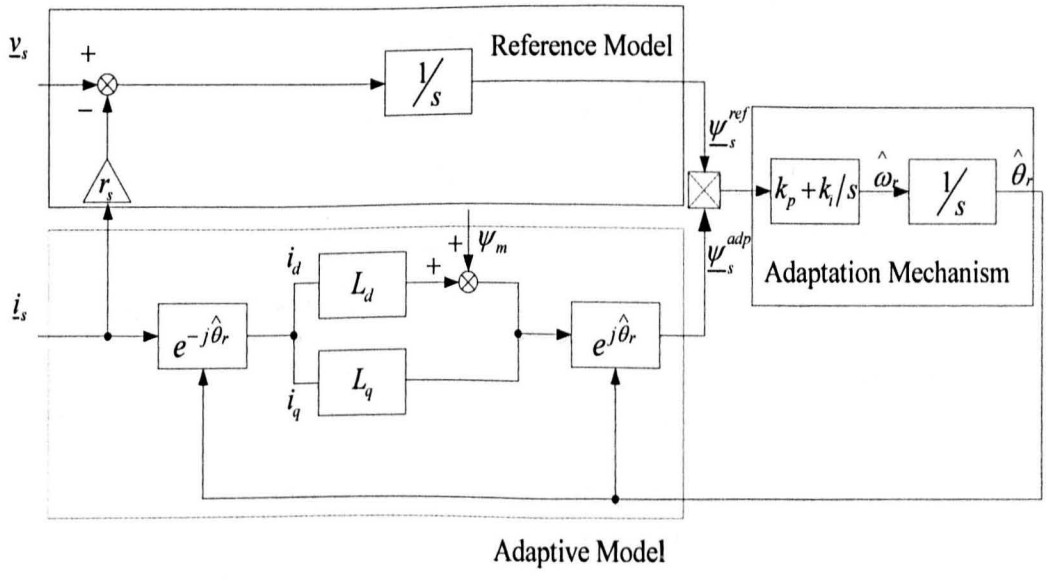

Figure 2.1: System Schematic of a MRAS with a PLL type adaptation mechanism

In the schematic of Figure 2.1, a PLL (Phase Locked Loop [6]) type adaptation law has been chosen to estimate the rotor speed/position and the drive orientation error to zero. However, a better dynamic performance can be

achieved by replacing the PLL with a Luenberger observer which uses a feed-forward term of (the torque reference), which will be discussed in detail later in this chapter.

However, the method suffers from drift problems due to the pure integration required for obtaining the flux vectors in (2-5). Several alternatives have been introduced to overcome these problems. In [25], a first order low pass filter with a carefully chosen cut-off frequency replaces the pure integrator. At frequencies much higher than the filter's cut-off frequency, the filter behaves as a pure integrator with its dc offset significantly attenuated compared with that of a pure integrator, and this is shown by the frequency response plotted in Figure 2.2.

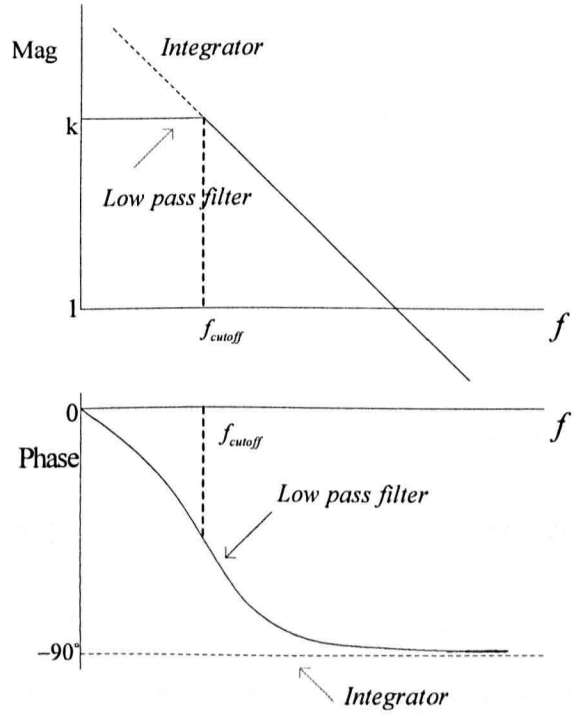

Figure 2.2: Bode plot of a pure integrator (dashed) and a low pass filter (solid)

However, this approach fails at low frequencies, because the information used falls within the bandwidth of the low pass filter making it difficult to extract due to reduced gain. Furthermore, the fact that the 90 degrees lagging property is no longer valid also affects the use of this method in the low frequency region.

Adding a high pass filter after the pure integration has a similar effect as the low pass filter approximation method mentioned above, which in other words, also fails below certain frequencies.

Another solution was proposed in [26-28] to avoid the drift problems, by adding proper compensation for the dc offset remaining in the voltage or current measurements, namely a closed loop flux observer, as shown in Figure 2.3.

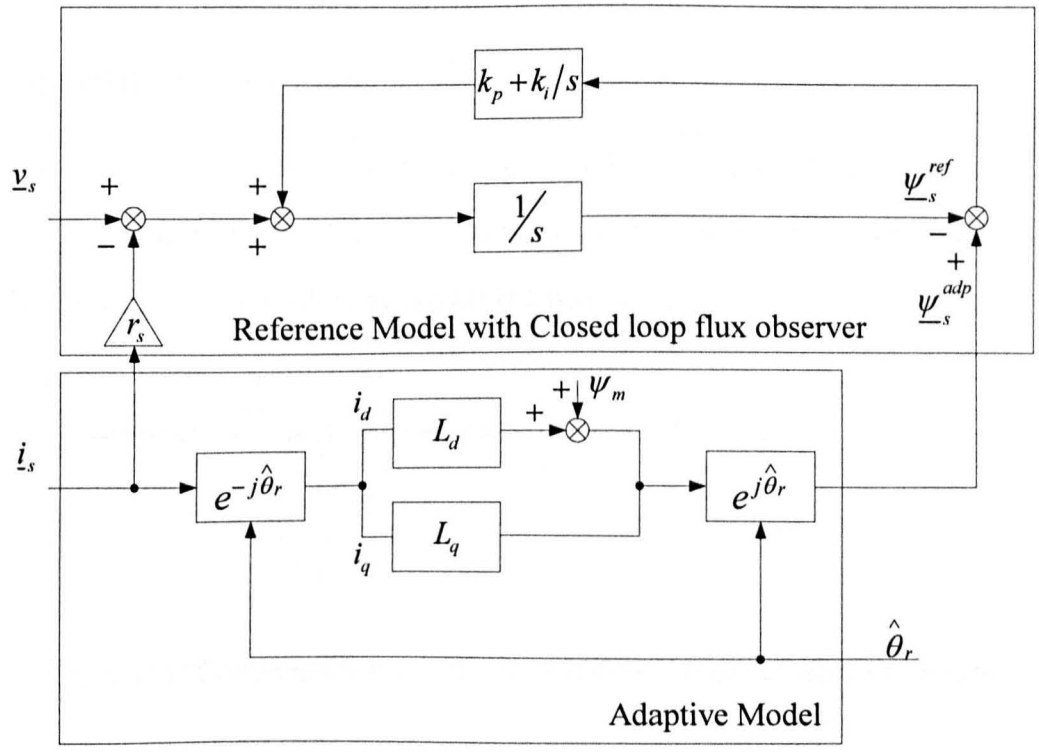

Figure 2.3: Structure of reference model with closed loop flux observer

This topology helps the system achieve reasonable estimation under 2Hz operational frequencies by forcing the reference model to follow the adaptive model estimation which does not have the integration that the voltage equation uses in the reference model.

All the above methods are based on measured phase/line voltages. However it is preferable to avoid this because it relies on accurate measurements and will contain extra offsets and noise. Alternatively, the voltage reference $\underline{v}_s^*$ can be used for the calculations. However, when speed decreases, the reference voltage

drops accordingly, even to the extent that its amplitude is similar as or smaller than the voltage drops across the power semiconductors. Thus, a suitable compensation scheme [29] needs to be considered at low frequency, especially for the low speed, heavy loaded situation when power MOSFET switches are used, this is because a power MOSFET switch can be approximated by a small resistor when conducting. So the voltage drop across the device can be simply modelled as a function of the conducting current, $(i_s \cdot r_{on})$, and is therefore very influential under heavy load.

The compensation scheme for the power MOSFET voltage drop is implemented by feeding forward the device voltage drop to the reference voltage calculated from the current controller, as shown in Figure 2.4.

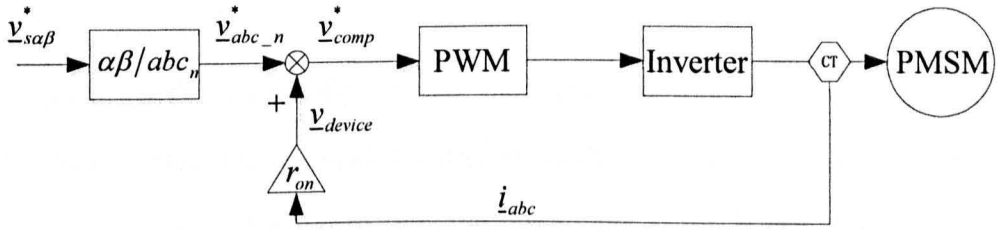

Figure 2.4: Compensation scheme for MOSFET-type switch voltage drop

2.3.2 State Observer based method

This method [30, 31] basically makes use of a state observer to model the system. The states are defined as stator currents in the *dq* synchronous frame and the rotor position and speed. The latest estimation of the rotor position is used to perform the frame transformation. The reduced order observer and other types of observers such as sliding mode observer were also reported in [32, 33], aiming to reduce the influence of uncertainty of the machine's parameters (e.g. thermal and flux level changes).

2.3.3 Extended Kalman Filter method

The Kalman filter method can be generally categorized as a state observer type of method. It models the system with rotor speed as one state variable, and the Kalman filter is used to first predict this variable and then correct it in a recursive manner to achieve the final estimate. The difference between this method and other observer based methods is that not only is the state variable estimated, but the error covariance is also calculated so that noise can be removed from the measurements [25]. The basic implementation of the Kalman filter method is only applicable for a linear system, while an Extended Kalman filter (EKF) [10, 34] can deal with non-linear systems at the expense of increased computational effort. This can however be reduced by integrating a predefined look up table [10, 35].

Compared with other model-based methods, the EKF method has a less tolerance to machine parameter variation such as stator resistance, and has a poorer dynamic performance, but the advantage is its better noise rejection ability over the other methods [2, 10, 35, 36].

2.3.4 Other model based methods

In [37], a different method was proposed which also makes use of the fundamental machine equations. It relies on injecting a low frequency current signal on to the stator current, and constructs an error signal by investigating the back-EMF induced by the injection current. This error is forced to zero to reduce the oscillation to zero if correct orientation achieved. This method was claimed to improve the low frequency performance and provide a wider operation range combined with other model based methods but few implementations were presented.

There are other methods based on machine fundamental model, such as those based on neural networks [9] and fuzzy logic observers [7]. The low frequency performance still remains poor.

2.4 Speed/position estimation by saliency tracking

2.4.1 Saliencies in the PMAC machines

There are several types of Permanent Magnet Synchronous Machines (PMSM). With different ways of mounting the permanent magnets, they can be classified into the following two groups: the Interior Permanent Magnets Machines (IPM) and the Surface Mounted Permanent Magnets Machines (SMPM). IPM machines have the magnets buried in the rotor iron, while SMPM machines have their magnets attached on the surface of the rotor. These two designs can be illustrated for a four-pole machine as shown in Figure 2.5.

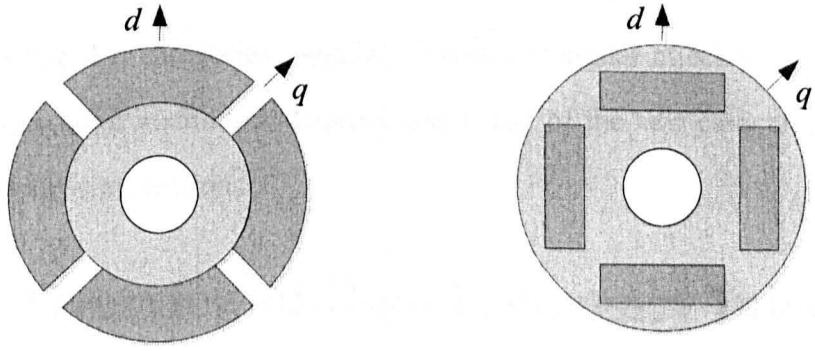

(*a*) (*b*)

Figure 2.5: Rotor magnets arrangements for two types of PMSM machines:

(a), Surface Mounted machine (SMPM); (b), Interior machine (IPM)

Since the permeance of the magnet is almost the same as air, the effective air-gap length along the *d-axis* for an IPM machine is much longer than that along the

q-axis. As a result, the *d-axis* inductance is much lower than the *q-axis* inductance. This saliency is called the Geometric saliency and is the main saliency for the IPM machines.

While for the SMPM machines, the effective length of the air-gap along either *d* or *q* axis are the same, indicating that no Geometric saliency is present in SMPM machines. The saliency in this type of machines is Saturation Induced saliency. It is due to the flux saturating the iron core causing a reduction of the inductance. The resulting spatial inductance variation is $l_{md} < l_{mq}$ when the saturation affects the main flux path, or $l_{\sigma d} > l_{\sigma q}$ when the saturation affects the leakage flux path. One of the effects is normally the main source of saturation for SMPM machines.

The saliency tracking method makes use of these saliencies to identify the rotor position. These saliencies appear as a rotor position dependent variation of inductance as described ealier, and therefore if this can be measured electrically, the saliency and rotor position can be tracked. The methods can be classified into the following two categories: high/low frequency signal injection method and current derivative method. A detailed discussion of the two categories will be given in following sections.

2.4.2 Overview of High Frequency Injection methods

This method involves superimposing a high frequency sinusoidal (*hf*) signal (usually several hundred Hz to several kHz) onto the fundamental components of the machine. The response of this signal is also revealed as an *hf* component and its amplitude is modulated by the machine's saliency, allowing the tracking of the saliency by a proper demodulation scheme. The injecting signal can be

either a voltage component added to the demanded voltage output from the current controller, or a current component directly fed into the current controller as part of the current demand. However, *hf* current signal injection is often not desirable since it requires a high bandwidth current controller to allow the measurement of the induced high frequency voltage signal which increases the complexity of the controller design. Thus, the *hf* voltage injection is more preferable in practice.

Many different types of voltage injection schemes have been proposed. They can be broadly classified into $\alpha\beta$ rotating injection, *d/q-axis* pulsating injection and *d-q* synchronous frame rotating injection.

2.4.3 Saliency tracking by high frequency $\alpha\beta$ rotating signal injection

The $\alpha\beta$ injection method [38-40] is widely adopted due to its simplicity of implementation and it does not require frame transformation. This method superimposes the *hf* voltage signal onto the stationary reference frame ($\alpha\beta$ frame). The *hf* injection voltage vector is given as:

$$\begin{bmatrix} v_\alpha \\ v_\beta \end{bmatrix} = V_i \cdot \begin{bmatrix} -\sin(\omega_i t) \\ \cos(\omega_i t) \end{bmatrix} \tag{2-7}$$

where V_i is the amplitude and ω_i is the frequency of the injected *hf* voltage vector. For a PM synchronous machine with either geometric saliency or saturation saliency, the voltage equation in the $\alpha\beta$ frame is derived as [19]:

$$\begin{bmatrix} v_\alpha \\ v_\beta \end{bmatrix} = r_s \begin{bmatrix} i_\alpha \\ i_\beta \end{bmatrix} + \frac{d}{dt} \begin{bmatrix} L_s - \Delta L_s \cdot \cos(2\theta_\delta) & -\Delta L_s \cdot \sin(2\theta_\delta) \\ -\Delta L_s \cdot \sin(2\theta_\delta) & L_s + \Delta L_s \cdot \cos(2\theta_\delta) \end{bmatrix} \begin{bmatrix} i_\alpha \\ i_\beta \end{bmatrix} + \omega_r \psi_m \begin{bmatrix} -\sin(\theta_\delta) \\ \cos(\theta_\delta) \end{bmatrix} \tag{2-8}$$

where, r_s is the stator resistance, and $\omega_r\psi_m(-\sin(\theta_\delta)+j\cos(\theta_\delta))$ is the back-EMF term. It is noted that rather than using the actual rotor position θ_e (assuming a one pole pair machine for easily understanding), the saliency angle is used, quoted as θ_δ. This is because the saliency position is not always aligned to the real rotor position and the degree of misalignment increases proportional to the load current applied to the machine due to the "armature reaction" effect [19]. The corresponding saliency frame is denoted as the $\delta\gamma$ frame, and the average inductance L_s and inductance variation ΔL_s can be specified as [19]:

$$L_s = \frac{L_\delta + L_\gamma}{2}, \quad \Delta L_s = -\frac{L_\delta - L_\gamma}{2} \tag{2-9}$$

and assumes a sinusoidal variation at twice the electrical frequency. Higher order effects are ignored at this stage.

When an *hf* voltage signal such as (2-7) is applied to the machine at a low rotating speed, the back-emf term of (2-8) can be neglected. The voltage drop across the stator resistor can be also neglected since the induced *hf* inductance term dominates the voltage equation. An approximation of (2-8) can therefore be written as:

$$\begin{bmatrix} v_{\alpha h} \\ v_{\beta h} \end{bmatrix} = \frac{d}{dt}\begin{bmatrix} L_s - \Delta L_s \cdot \cos(2\theta_\delta) & -\Delta L_s \cdot \sin(2\theta_\delta) \\ -\Delta L_s \cdot \sin(2\theta_\delta) & L_s + \Delta L_s \cdot \cos(2\theta_\delta) \end{bmatrix} \cdot \begin{bmatrix} i_{\alpha h} \\ i_{\beta h} \end{bmatrix} \tag{2-10}$$

where the notation *h* means that the values are the *hf* components.

By integrating both sides of the equation, the induced *hf* current is obtained:

$$\begin{bmatrix} i_{\alpha h} \\ i_{\beta h} \end{bmatrix} = \frac{V_i}{\omega_i L_\delta L_\gamma}\begin{bmatrix} L_s \cos(\omega_i t) + \Delta L_s \cos(2\theta_\delta - \omega_i t) \\ L_s \sin(\omega_i t) + \Delta L_s \sin(2\theta_\delta - \omega_i t) \end{bmatrix} \tag{2-11}$$

Clearly, it shows that the induced *hf* current signal can be regarded as the

combination of a positive sequence component rotating at a frequency of ω_i and a negative sequence component rotating at a frequency of $-\omega_i$. The saliency information ($2\theta_\delta$) is modulated in the negative sequence of the current and can be extracted to acquire the rotor position. Typical demodulation techniques are described in the following sections.

2.4.3.1 Heterodyne demodulation

To better understand the heterodyne demodulation method [38] described in this section, it is worthwhile rewriting (2-11) in complex notation, given by:

$$\underline{i}_{\alpha\beta h} = \frac{V_i}{\omega_i L_\delta L_\gamma}(L_s e^{j\omega_i t} + \Delta L_s e^{j(2\theta_\delta - \omega_i t)}) \tag{2-12}$$

The main idea is to extract the saliency component $2\theta_\delta$ contained in the negative sequence current. An estimated saliency angle is assumed and a unity vector $e^{-j(2\hat{\theta}_\delta - \omega_i t)}$ can be formed. The multiplication of the unity vector and (2-12) yields:

$$\underline{i}_{\alpha\beta h} \cdot e^{-j(2\hat{\theta}_\delta - \omega_i t)} = \frac{V_i}{\omega_i L_\delta L_\gamma}(L_s e^{j(2\omega_i t - 2\hat{\theta}_\delta)} + \Delta L_s e^{j(2\theta_\delta - 2\hat{\theta}_\delta)}) \tag{2-13}$$

The resultant current consists of a high frequency term and a low frequency term and the latter can be extracted by passing the vector through a low pass filter (LPF). The result is a current component which is only dependent on the real and estimated saliency angle as:

$$LPF\{\underline{i}_{\alpha\beta h} \cdot e^{-j(2\hat{\theta}_\delta - \omega_i t)}\} = \frac{V_i}{\omega_i L_\delta L_\gamma}\Delta L_s e^{j(2\theta_\delta - 2\hat{\theta}_\delta)} \tag{2-14}$$

The imaginary part of the above signal forms an error signal which can be fed to a tracking mechanism, and can be written as:

$$\xi = \mathrm{Im}\{\frac{V_i}{\omega_i L_\delta L_\gamma}\Delta L_s e^{j(2\theta_\delta - 2\hat{\theta}_\delta)}\} = \frac{V_i}{\omega_i L_\delta L_\gamma}\Delta L_s \sin(2\theta_\delta - 2\hat{\theta}_\delta) \qquad (2\text{-}15)$$

Assuming that the error between the estimated saliency angle and the real saliency angle $(\theta_\delta - \hat{\theta}_\delta)$ is sufficiently small, the 'sine' term of the error signal can be approximated by $(2\theta_\delta - 2\hat{\theta}_\delta)$. The final form of the error signal is given as:

$$\xi \cong \frac{2V_i}{\omega_i L_\delta L_\gamma}\Delta L_s(\theta_\delta - \hat{\theta}_\delta) \qquad (2\text{-}16)$$

The scheme for this demodulation method is presented in Figure 2.6.

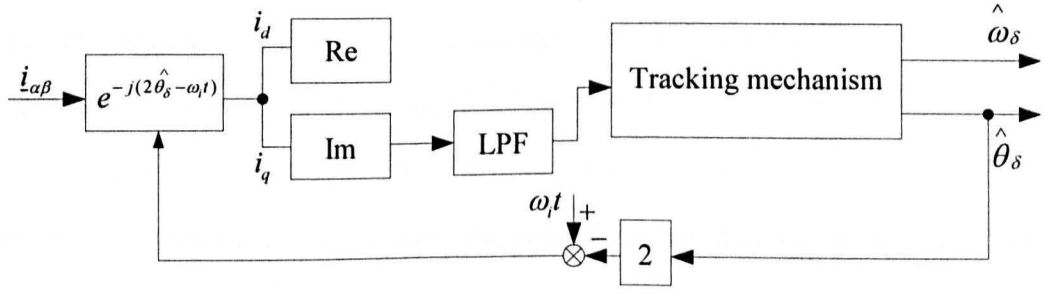

Figure 2.6: Scheme of heterodyne demodulation for $\alpha\beta$ injection method

The tracking mechanism can be either a PLL or a Luenberger type position and speed observer [39]. The latter is preferable due to its better dynamic performance brought by including the demand torque as a feed forward term.

The limitation of this demodulation scheme is that it relies on the amplitude of the error signal obtained in (2-16), and it is rather small in a surface mounted PM machine (the type typically used for EPS). Note that the inductance variation which causes the error signal is much smaller in a suface mounted PM machine than in an interior PM machine. The error signal is therefore difficult to identify after the low pass filter. In addition, noise and other distortions induced by, for example, dead time and zero crossing effects in the power converter can be

difficult to remove when this scheme is adopted.

2.4.3.2 Homodyne demodulation method

The homodyne demodulation scheme [41] is outlined in Figure 2.7.

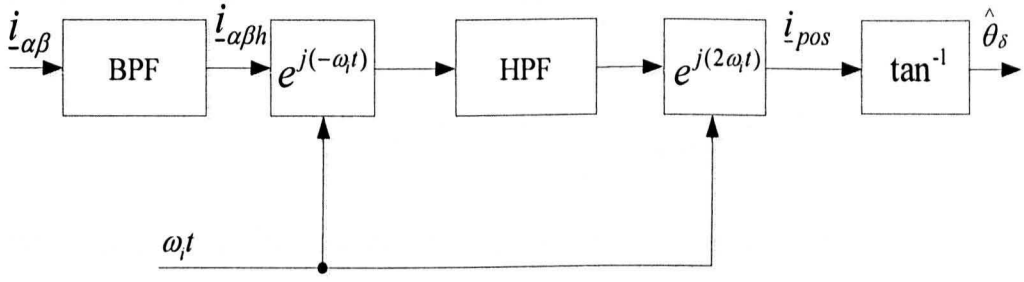

Figure 2.7: Scheme of homodyne demodulation for $\alpha\beta$ injection method

As shown in Figure 2.7, the homodyne method is an open loop demodulation scheme, which does not need the estimated angle information for demodulating the useful signal from the induced *hf* current signals. The advantage of this approach is that it does not rely on the accuracy of the estimated position signal (which is critical for a heterodyne demodulation method which uses the assumption that the estimated position is close to the real position). The signal processing of the homodyne demodulation method is discussed below.

The current vector in the stationary $\alpha\beta$ frame, $\underline{i}_{\alpha\beta}$ is first passed through a band pass filter, centred at the injection high frequency ω_i. The induced high frequency current vector in the $\alpha\beta$ frame, $\underline{i}_{\alpha\beta h}$ is obtained and then transformed to an arbitrary frame rotating at a frequency of ω_i as:

$$\underline{i}_{\alpha\beta h} \cdot e^{-j\omega_i t} = \frac{V_i}{\omega_i L_\delta L_\gamma}(L_s + \Delta L_s e^{j(2\theta_\delta - 2\omega_i t)}) \qquad (2\text{-}17)$$

A high pass filter (HPF) is then used to remove the DC value from the above equation and only the saliency associated component is left as:

$$HPF\{\underline{i}_{\alpha\beta h} \cdot e^{-j\omega_i t}\} = \frac{V_i}{\omega_i L_\delta L_\gamma} \Delta L_s e^{j(2\theta_\delta - 2\omega_i t)} \tag{2-18}$$

The signal is then passed through a further frame transformation with a synchronous frequency of $(-2\omega_i)$, giving:

$$\underline{i}_{pos} = HPF\{\underline{i}_{\alpha\beta h} \cdot e^{-j\omega_i t}\} \cdot e^{j2\omega_i t} = \frac{V_i}{\omega_i L_\delta L_\gamma} \Delta L_s e^{j2\theta_\delta} \tag{2-19}$$

This term contains the saliency information.

The next step is to extract the saliency position. Since it is the phase of the $\underline{i}_{pos}$ vector containing the saliency information, a simple $\tan^{-1}$ function can be used to derive $2\theta_\delta$. Noticing that the product of a $\tan^{-1}$ function ranges from $-\pi$ to $+\pi$, the saliency angle θ_δ cannot be directly obtained by dividing $2\theta_\delta$ by 2. A remainder function is therefore introduced [41] to give the correct position signal. A PLL or Luenberger observer can be used to replace the $\tan^{-1}$ function to improve the quality of the extraction scheme since both benefit from the low pass property of the PI controller, resulting a saliency angle θ_δ with reduced noise.

Unlike the heterodyne demodulation method mentioned in the previous section, it is possible to remove distortions contained in the saliency angle θ_δ due to disturbances such as higher order saliencies and inverter non-linearity. This is because the signal used for extracting θ_δ is a vector having both amplitude and phase information, which makes the separation of this signal from disturbances with other frequencies possible, whereas the signal used in a heterodyne type method varies only with extracted amplitude information. Different methods to reduce such distortions will be outlined in the next section.

2.4.4 Methods for disturbance removal for $\alpha\beta$ *hf* signal injection

Position/speed signals obtained using the demodulation schemes themselves cannot give optimal performance for orientation and speed control in a vector controlled system. In fact, the raw position/speed estimations are distorted by several disturbances. The disturbances originate from higher order saliencies in the machine [42], the inverter non-linearity effect resulting from the dead time and zero current crossing situations [43], and also the load current which introduces further shift of the saliency position due to armature reaction [44]. Several techniques for eliminating these distortions have been proposed in [40, 45, 46].

2.4.4.1 Disturbance elimination by Space Modulation Profiling (SMP)

This technique is proposed in [19, 45, 46]. It involves using a 3-D look-up table in which the distortion information is stored and accessed using the estimated current angle and load. A pre-commissioning procedure is needed for the creation of such a look-up table. The system needs to be operated in sensored mode at certain speeds and different load conditions. The measured position signal i_{pos} (refer to Fig. 2.6) passes through a band stop filter [45] centred at saliency frequency $2\theta_s$ (note this is available as we are in the sensored mode) or a combination of a band pass filter and a low pass filter to extract the distortion information. The disturbances and associated load current and estimated current angle are then stored in the look-up table to compensate the raw signal for sensorless control. The scheme for the SMP technique is shown in Figure 2.8.

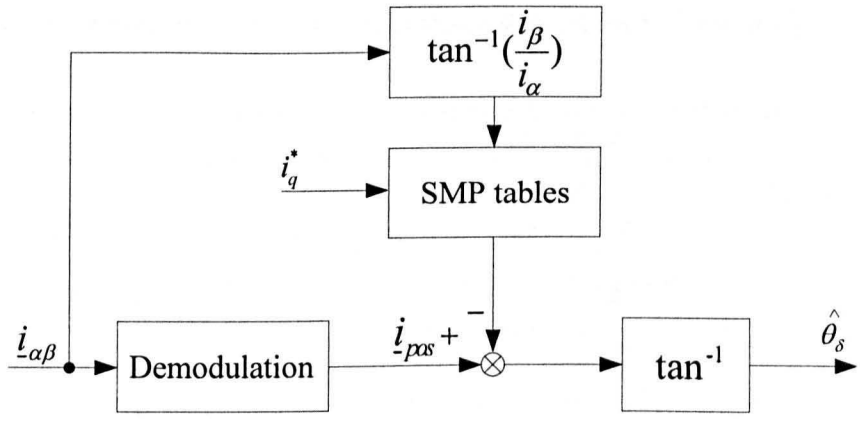

Figure 2.8: Implementation of SMP compensation scheme

In [19] a combined SMP technique with extra armature reaction compensation is proposed to improve the quality of position estimation.

It is noted that the SMP technique assumes that there is little difference in the disturbance information at different speeds and the SMP table obtained at a certain speed can be extrapolated to a wide speed range. Another disadvantage is that it requires intensive commissioning efforts before being applied for compensation. The space of memory required is also costly especially for a high current machine as used in this work.

2.4.4.2 Disturbance elimination by Spatial Filtering

The spatial filtering [40] method can be regarded as a simplified SMP. Rather than storing all disturbance information in the SMP, it extracts higher order saturation saliencies by passing the position signal $\underline{i}_{pos}$ to several band pass filters centred at these saliency frequencies. The outputs of these filters are the disturbances and are stored in a look-up table. They are subtracted in a similar manner as for the SMP technique.

2.4.4.3 Disturbance elimination by the Synchronous Filter and Memory method

The synchronous filter technique [17, 20, 29, 43, 47] is an online approach to

remove disturbances at any appointed frequency, shown as Figure 2.9.

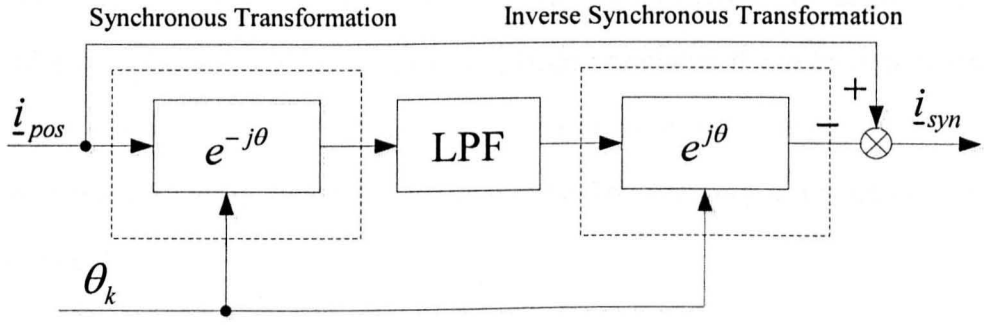

Figure 2.9: Structure of a Synchronous Filter

The raw position signal $\underline{i}_{pos}$ first transforms to arbitrary frames rotating synchronously with designated frequencies f_k at the disturbance frequencies which need to be removed, denoted as a Synchronous Transformation. The disturbance components of the specific frequencies become DC values in the newly defined frames, and narrow bandwidth low pass filters can be applied to filter out other frequency components leaving only the DC values. The DC values are d and q values and contain information about both amplitude and phase of the disturbance components. The original disturbance signals can be reconstructed by inverse synchronous transformations. For the final stage the reconstructed disturbance signals are subtracted from the raw position signal resulting in a clean position estimate.

The angle used for the synchronous transformation and its inverse θ_k can be set to zero to remove a DC offset, or a higher order saturation saliency, or a combination of *hf* carrier angle $\pm n\omega_i t$ and higher order saturation saliency $\pm m \cdot \hat{\theta}_\delta$ (known as sideband filter [29]).

However, the synchronous filter approach fails at very low speed due to overlap of the pass bands of the low pass filters used to extract disturbances. A memory

method is therefore incorporated in the system [43]. The drive should be initially operated at higher speeds to allow the synchronous filter to fill the memory with suitable values. After the memory has been populated it can be applied to low speed sensorless control for disturbance elimination since the current distortion is considered to be dependent on load only. The memory structure is shown in Figure 2.10.

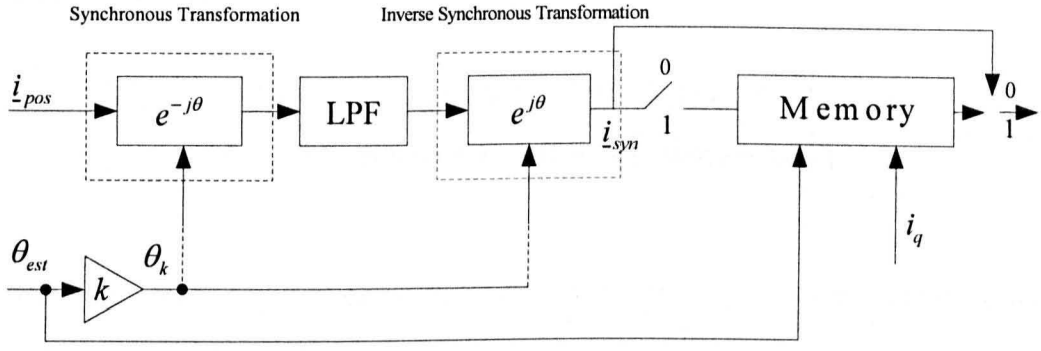

Figure 2.10: Filling process of memory method

A low memory method was proposed in [47] which put the memory cell in the synchronous frame. In such a way, the contents in the memory are DC values allowing the reduction of memory space consumption.

2.4.5 Saliency tracking by *d-axis* pulsating injection

Unlike the rotating vector used in the *hf* $\alpha\beta$ injection method, the *d-axis* pulsating injection method uses a pulsating signal superimposed onto the estimated saliency axis $\hat{\delta}$ only, as:

$$\begin{bmatrix} \hat{v}_{\delta h} \\ \hat{v}_{\gamma h} \end{bmatrix} = V_i \cdot \begin{bmatrix} -\sin(\omega_i t) \\ 0 \end{bmatrix} \tag{2-20}$$

where $\hat{\delta}$-$\hat{\gamma}$ refers to the estimated saliency reference frame. The advantage of

this pulsating injection over the rotating vector injection is that it only injects an additional voltage onto the flux axis and not onto the torque producing axis, which reduces the torque ripple significantly.

The analysis is based on the *d-q* model of the PM machine with the estimated saliency frame $\hat{\delta}$-$\hat{\gamma}$ replacing the *d-q* frame, neglecting the resistor voltage drop and the back-EMF term, shown as:

$$\begin{bmatrix} \hat{v}_{\delta h} \\ \hat{v}_{\gamma h} \end{bmatrix} = \frac{d}{dt} \begin{bmatrix} L_s - \Delta L_s \cdot \cos(2\Delta\theta_\delta) & \Delta L_s \cdot \sin(2\Delta\theta_\delta) \\ \Delta L_s \cdot \sin(2\Delta\theta_\delta) & L_s + \Delta L_s \cdot \cos(2\Delta\theta_\delta) \end{bmatrix} \cdot \begin{bmatrix} \hat{i}_{\delta h} \\ \hat{i}_{\gamma h} \end{bmatrix} \tag{2-21}$$

where L_s and ΔL_s are given in (2-9), $\Delta\theta_\delta = \hat{\theta}_\delta - \theta_\delta$ is the estimation error angle. Applying the voltage injection of (2-20) to the equation above, the resultant current response is given as:

$$\begin{bmatrix} \hat{i}_{\delta h} \\ \hat{i}_{\gamma h} \end{bmatrix} = \frac{V_i \cos(\omega_i t)}{\omega_i L_\delta L_\gamma} \begin{bmatrix} L_s + \Delta L_s \cos(2\Delta\theta_\delta) \\ -\Delta L_s \sin(2\Delta\theta_\delta) \end{bmatrix} \tag{2-22}$$

Different demodulation methods have been implemented [15, 16, 48, 49] and are discussed below.

2.4.5.1 Measurement axis demodulation method

The "Measurement Axis" method proposed by Sul [16] introduces a new axis namely the measurement axis δ^m-γ^m at 45 degrees from the estimated saliency axis, as shown in Figure 2.11.

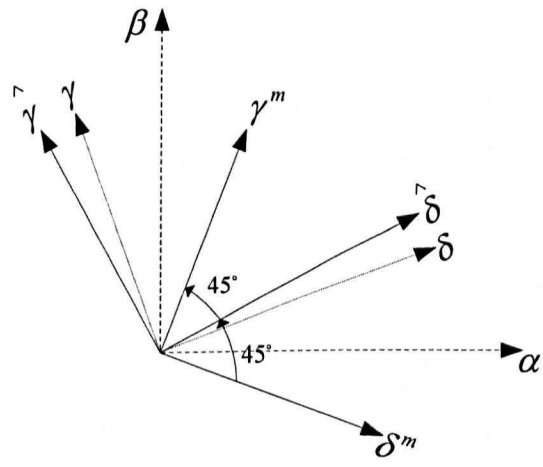

Figure 2.11: Axis arrangement of measurement axis demodulation method

Assuming the estimated saliency axis is superimposed on the real saliency axis, the measurement axis is therefore 45 degrees from the real saliency axis. The magnitude of the real δ axis impedance split along δ^m axis and γ^m axis should be the same. The resulting *hf* current amplitude i_δ^m and i_γ^m should also remain the same. Any difference between these two measurements indicates misalignment of the estimated and real saliency axis and can be used as an error signal to adjust the saliency estimation. The overall scheme of measurement axis method is given in Figure 2.12.

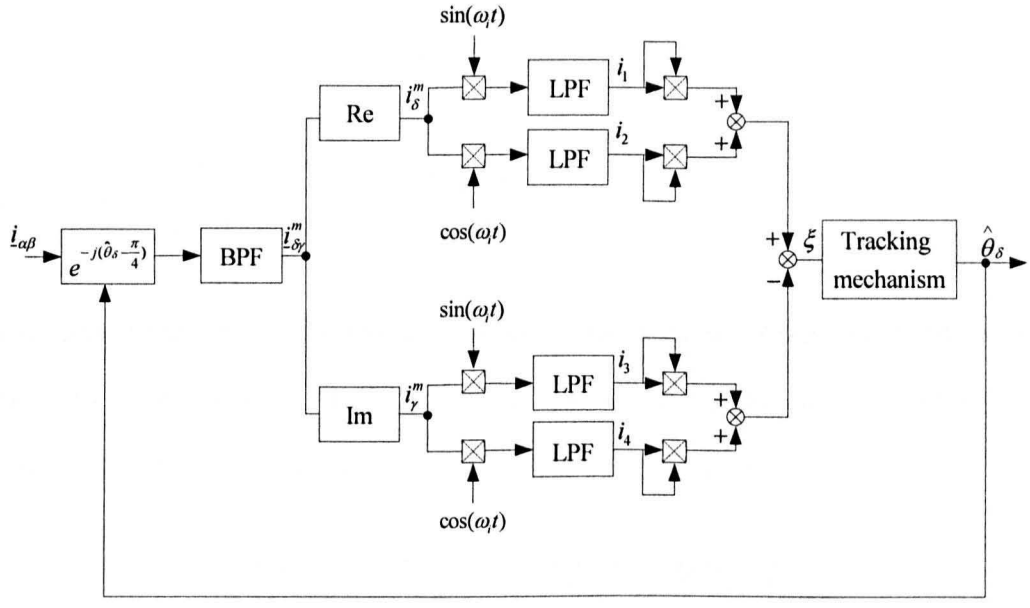

Figure 2.12: Structure of measurement axis demodulation method

The measured *hf* current vector is transformed to the measurement frame δ^m-γ^m yielding:

$$\begin{bmatrix} i_\delta^m \\ i_\gamma^m \end{bmatrix} = \frac{-\sqrt{2}\cdot V_i \cos(\omega_i t)}{2\omega_i L_\delta L_\gamma} \begin{bmatrix} L_s + \Delta L_s \cos(2\Delta\theta_\delta) - \Delta L_s \sin(2\Delta\theta_\delta) \\ L_s + \Delta L_s \cos(2\Delta\theta_\delta) + \Delta L_s \sin(2\Delta\theta_\delta) \end{bmatrix} \tag{2-23}$$

The current vector is then multiplied by the carrier component to create a DC component and a twice injection frequency component. After low pass filtering the twice injection frequency component can be removed and only the saliency related signal is left as:

$$i_1 = i_2 = \frac{-\sqrt{2}\cdot V_i}{4\omega_i L_\delta L_\gamma}(L_s + \Delta L_s \cos(2\Delta\theta_\delta) - \Delta L_s \sin(2\Delta\theta_\delta)) \tag{2-24}$$

$$i_3 = i_4 = \frac{-\sqrt{2}\cdot V_i}{4\omega_i L_\delta L_\gamma}(L_s + \Delta L_s \cos(2\Delta\theta_\delta) + \Delta L_s \sin(2\Delta\theta_\delta)) \tag{2-25}$$

The squaring of the saliency related current magnitude is obtained as:

$$\frac{\left|i_\delta^m\right|^2}{4} = i_1^2 + i_2^2 = \frac{1}{4}[I_0 + I_1 \cos(2\Delta\theta_\delta) - I_1 \sin(2\Delta\theta_\delta)]^2 \tag{2-26}$$

$$\frac{\left|i_{\gamma}^{m}\right|^{2}}{4}=i_{3}^{2}+i_{4}^{2}=\frac{1}{4}[I_{0}+I_{1}\cos(2\Delta\theta_{\delta})+I_{1}\sin(2\Delta\theta_{\delta})]^{2} \tag{2-27}$$

where $I_0=\frac{-\sqrt{2}\cdot V_i L_s}{2\omega_i L_\delta L_\gamma}$, $I_1=\frac{-\sqrt{2}\cdot V_i \Delta L_s}{2\omega_i L_\delta L_\gamma}$.

As mentioned above, the two magnitudes should be the same if the estimated saliency lies upon the real one. Thus, an error signal can be formed by comparing the two magnitudes in (2-26) and (2-27), giving:

$$\xi=\frac{\left|i_{\delta}^{m}\right|^{2}}{4}-\frac{\left|i_{\gamma}^{m}\right|^{2}}{4}=I_{0}I_{1}\sin(2\Delta\theta_{\delta})+\frac{I_{1}^{2}}{2}\sin(4\Delta\theta_{\delta}) \tag{2-28}$$

The difference between the two axes can be approximated by the amplitude of the error signal. The error signal can be used to drive a tracking mechanism, either a PLL or a Luenberger observer, to force the alignment of the two axes and give the saliency estimation.

As with the heterodyne demodulation for the $\alpha\beta$ injection method described in the previous section, this method requires a high enough value of difference of the δ-γ inductances, ΔL_s, which is sometimes very small in the surface mounted types of machines, resulting in difficulty in determining the saliency angle.

2.4.5.2 Direct demodulation method

As observed from (2-22), $\hat{i}_{\gamma h}$ directly relates to the saliency information. After demodulating to remove the carrier information contained in this current, the saliency angle can be obtained by forcing its amplitude to zero. A direct demodulation scheme [48] is shown in Figure 2.13.

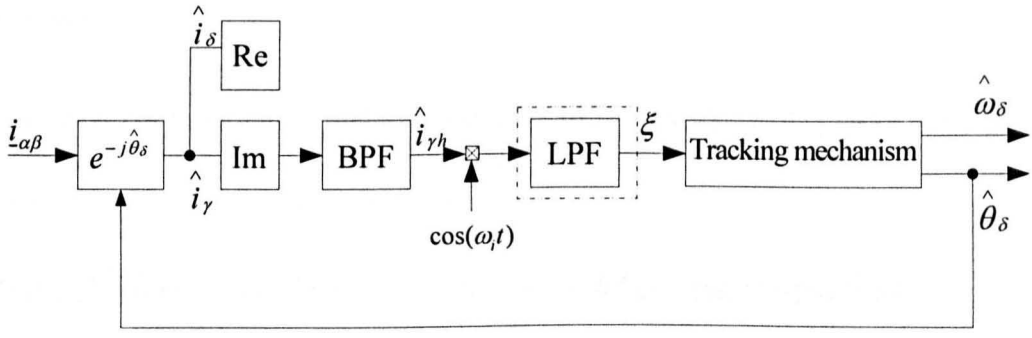

Figure 2.13: Direct demodulation scheme for *d-axis* injection

The measured current vector in the stationary frame first is transformed to the estimated saliency frame. Then the imaginary part of the new vector is band pass filtered to give the *hf* current at $\hat{\gamma}$ axis, i.e. $\hat{i}_{\gamma h}$. Multiplication by the carrier component, $\cos(\omega_i t)$, is made afterwards to give a DC component and a twice injection frequency component, illustrated as:

$$\hat{i}_{\gamma h} \cdot \cos(\omega_i t) = \frac{V_i \cdot \Delta L_s \cdot \sin(2\Delta\theta_\delta)}{2\omega_i L_\delta L_\gamma}(1+\cos(2\omega_i t)) \tag{2-29}$$

By passing this signal through a low pass filter, the twice injection frequency component can be removed, and assuming the estimation error is sufficiently small, this yields:

$$\xi = \frac{V_i \cdot \Delta L_s \cdot \sin(2\Delta\theta_\delta)}{2\omega_i L_\delta L_\gamma} \cong \frac{V_i \cdot \Delta L_s \cdot \Delta\theta_\delta}{\omega_i L_\delta L_\gamma} \tag{2-30}$$

The signal ξ is used to drive the mechanism to track the saliency angle. Alternatively, the low pass filter can be removed to avoid the phase shift introduced by this filter. Owing to the low pass property of the PI controller used in the tracking mechanism, the twice injection frequency component can also be removed. However, this arrangement requires an adequately low bandwidth of the controller, which weakens the dynamic performance of the control. Otherwise a large magnitude of twice injection frequency component still

remains.

The direct demodulation method also faces difficulty when ΔL_s is very small as with the measurement axis method.

2.4.5.3 Demodulation without use of *hf* carrier information

This method proposed in [15] is similar to the direct demodulation method mentioned above except for the separation technique of the injection frequency information and the saliency information. The diagram of this method is shown in Figure 2.14.

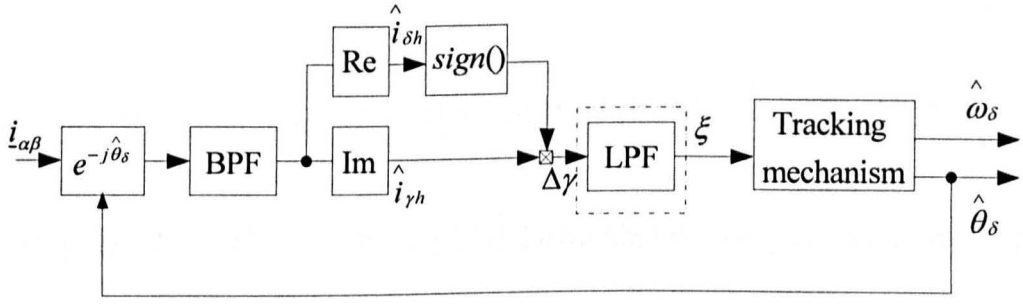

Figure 2.14: Scheme of carrier separation without using injection frequency information

The method used in this scheme for demodulating the saliency information from the carrier introduces another variable, namely $\Delta\gamma$, obtained by:

$$\Delta\gamma = \hat{i}_{\gamma h} \cdot sign(\hat{i}_{\delta h}) \tag{2-31}$$

This new variable is the angular error between the estimated axis $\hat{\delta}$ and the induced current vector $\underline{\hat{i}}_{\delta\gamma h}$, and can be shown in Figure 2.15.

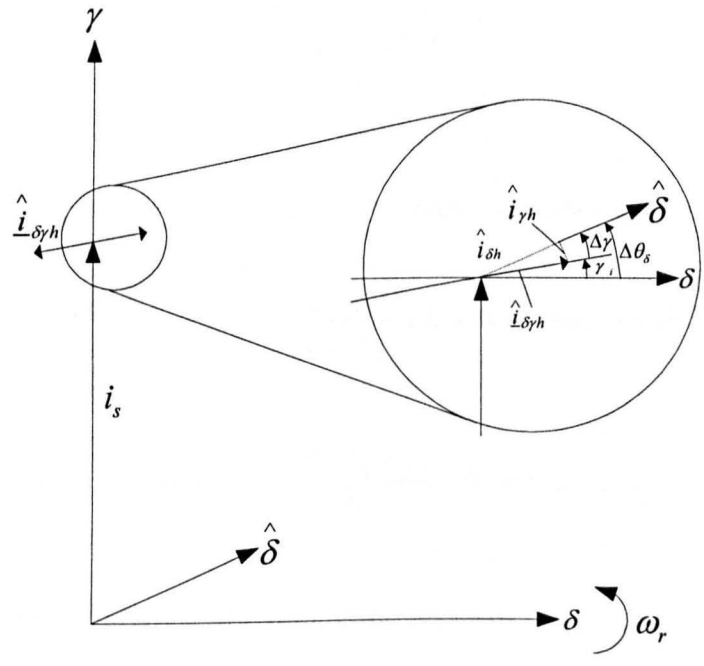

Figure 2.15: Diagram to show where $\Delta\gamma$ and γ_i are found [50]

In Figure 2.15, angle γ_i is the angle of the rotating vector $\hat{i}_{\delta\gamma h}$, and is given [15] as:

$$\gamma_i = \arctan(\frac{l_d}{l_q}\tan(\Delta\theta_\delta)) \tag{2-32}$$

and the angle relationship of $\Delta\gamma$, γ_i and $\Delta\theta_\delta$ can be obtained by:

$$\Delta\theta_\delta = \Delta\gamma + \gamma_i \tag{2-33}$$

It is found that if $\Delta\gamma = 0$, then $\Delta\theta_\delta = \gamma_i = 0$. Therefore, the signal $\Delta\gamma$ can be used to track the saliency. The detail of the demodulation is explained mathematically below.

For ease of analysis, the injection vector in (2-20) is shifted by 90°, giving:

$$\begin{bmatrix} \hat{v}_{\delta h} \\ \hat{v}_{\gamma h} \end{bmatrix} = V_i \cdot \begin{bmatrix} \cos(\omega_i t) \\ 0 \end{bmatrix} \tag{2-34}$$

The real and imaginary parts of the current vector are obtained:

$$\mathrm{Re}(\hat{\underline{i}}_{\delta\gamma h}) = \hat{i}_{\delta h} = \frac{V_i \sin(\omega_i t)}{\omega_i L_\delta L_\gamma}(L_s + \Delta L_s \cos(2\Delta\theta_\delta)) \tag{2-35}$$

$$\mathrm{Im}(\hat{\underline{i}}_{\delta\gamma h}) = \hat{i}_{\gamma h} = -\frac{V_i \sin(\omega_i t)}{\omega_i L_\delta L_\gamma}\Delta L_s \sin(2\Delta\theta_\delta) \tag{2-36}$$

Since $L_s >> \Delta L_s \cos(2\Delta\theta_\delta)$, the sign of the real part, $\mathrm{Re}(\hat{\underline{i}}_{\delta\gamma h})$, is dependent on the sign of $\sin(\omega_i t)$, as illustrated in Figure 2.16.

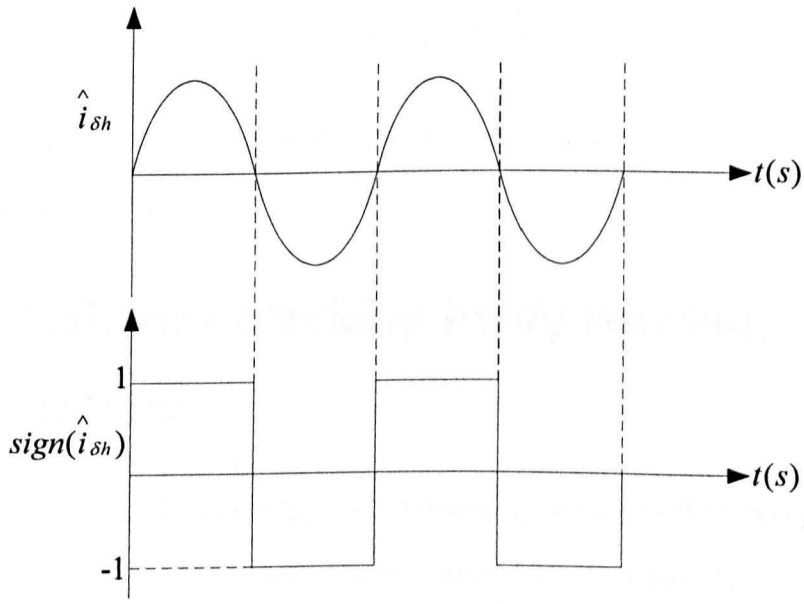

Figure 2.16: Illustration of sign function of the real part of *hf* current

The multiplication of the imaginary part and the sign of the real part, i.e. $\Delta\gamma$ can be written as:

$$\Delta\gamma = -\frac{V_i |\sin(\omega_i t)|}{\omega_i L_\delta L_\gamma}\Delta L_s \sin(2\Delta\theta_\delta) \tag{2-37}$$

The term of $|\sin(\omega_i t)|$ can be written in the form of Fourier series as:

$$|\sin(\omega_i t)| = \frac{2}{\pi} - \frac{2}{3\pi} \cdot \cos(2\omega_i t) + \ldots \tag{2-38}$$

If only the twice injection frequency component and DC component are considered, then (2-37) can be rewritten as:

$$\Delta\gamma = -\frac{V_i}{\omega_i L_\delta L_\gamma} \Delta L_s \sin(2\Delta\theta_\delta) \cdot (\frac{2}{\pi} - \frac{2}{3\pi} \cdot \cos(2\omega_i t)) \tag{2-39}$$

With the help of a low pass filter or with a low bandwidth controller, the twice injection frequency component can be filtered off leaving only saliency information similar to the other demodulation schemes.

$$\Delta\gamma \approx -\frac{4V_i \cdot \Delta L_s}{\omega_i L_\delta L_\gamma \pi} \Delta\theta_\delta \tag{2-40}$$

The signal of (2-40) can be driven to zero by a tracking scheme to achieve correct angle estimation.

2.4.6 Saliency tracking by *dq* rotating injection

This method [49] is similar to the $\alpha\beta$ rotating injection method except that the injected voltage vector is imposed on the estimated dq frame as:

$$\begin{bmatrix} \hat{v}_{\delta h} \\ \hat{v}_{\gamma h} \end{bmatrix} = V_i \cdot \begin{bmatrix} -\sin(\omega_i t) \\ \cos(\omega_i t) \end{bmatrix} \tag{2-41}$$

The current response is obtained as [19]:

$$\begin{bmatrix} \hat{i}_{\delta h} \\ \hat{i}_{\gamma h} \end{bmatrix} = \frac{V_i}{\omega_i L_\delta L_\gamma} \begin{bmatrix} L_s \cos(\omega_i t) + \Delta L_s \cos(-\omega_i t - 2\Delta\theta_\delta) \\ L_s \sin(\omega_i t) + \Delta L_s \sin(-\omega_i t - 2\Delta\theta_\delta) \end{bmatrix} \tag{2-42}$$

Again, the negative component contains the position information and the error between the estimated and real saliency axis can be obtained. This error is then tuned to zero to give an accurate estimate of the saliency angle. By compensating for the armature reaction, a final dq frame is obtained for vector control.

This method can produce better error signal compared to the *d-axis* injection method [49]. However, the voltage injection along the *q-axis* causes additional torque ripple which is disadvantageous to the *d-axis* injection method.

2.4.7 Saliency tracking by square wave injection

The square wave injection method was introduced in [51, 52] where a pulsating square wave was injected into the estimated *d-axis* for PM machine sensorless control. It was claimed to have less time delay due to the elimintation of the low pass filter employed in sinusoidal types of injection methods. In [53], the method was applied to an induction machine and injection axis was switched to the estimated *q-axis* to give a better estimate of the flux compared with a *d-axis* injection. In [54], the square wave signal was injected to the stationary reference α-β frame as a rotating form for the sensorless control of an IPM machine with similar performance to that of a pulsating type of square wave injection. This method was implemented in this thesis for the EPS applications and it will be discussed further in Chapter 3.

2.4.8 Overview of saliency tracking by measuring Current derivatives (di/dt)

The current derivative (di/dt) methods are generally linked with PWM transient excitation. Most of them involve modification of the PWM sequence, and the transient current response, termed the di/dt signals, is then measured which contains the saliency position information used to track the rotor position. The main methods categorized in this group are the INFORM method, the EM method, the Fundamental PWM excitation method and the Zero vector method, which will be discussed later. The advantage of these methods is that a higher signal-to-noise ratio (SNR) than that for the *hf* injection methods can be achieved and some of the methods can provide accurate estimation over a wide range of speed. The other advantage is that similar disturbance removal methods such as the synchronous filter and memory method as mentioned in 2.4.4 for the *αβ hf* rotating injection methods can be applied to obtain a clean position estimate. However, all of these methods involve the modification of the A/D sampling circuitry and increase the sampling rate. The modification of the PWM sequence will introduce extra torque ripple and more audible noise.

2.4.9 Saliency tracking by the INFORM method

The INFORM (Indirect Flux Detection by On-line Reactance Measurement) method introduced in [55] utilizes active voltage vectors (referred as test vectors) in addition to the fundamental PWM sequence to excite the machine, and the position signal can be constructed by examining the transient current (current derivative) response to the active voltage vectors.

A star connected machine with saturation induced saliency is considered here.

The inductance of each phase can be modelled as [29]:

$$l_a = l_0 + \Delta l \cos(2\theta_\delta) \tag{2-43}$$

$$l_b = l_0 + \Delta l \cos(2\theta_\delta - \frac{2\pi}{3}) \tag{2-44}$$

$$l_c = l_0 + \Delta l \cos(2\theta_\delta - \frac{4\pi}{3}) \tag{2-45}$$

where l_0 is the average stator inductance and Δl is the inductance variation due to saturation, $2\theta_\delta$ is the saturation saliency which needs to be tracked.

Supposing the demanded voltage vector resides in Sector I as shown in Figure 2.17,

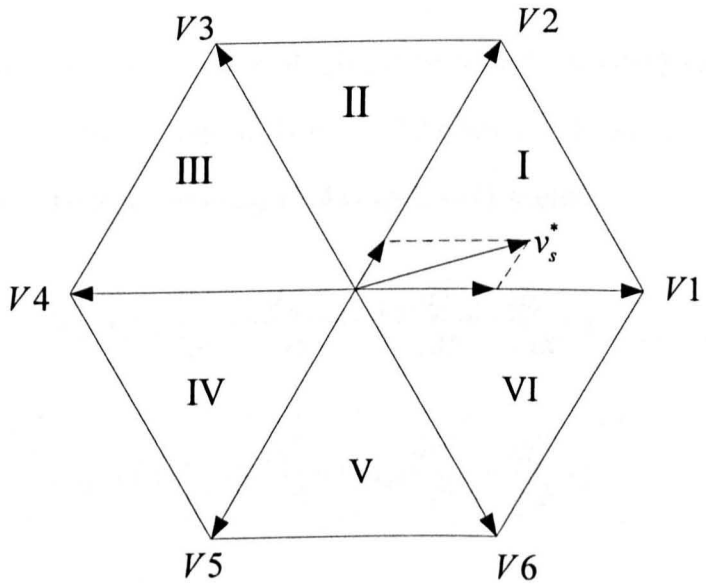

Figure 2.17: Vector diagram when the demanded voltage resides in sector I

when active vector $V1$ is applied, the following equations can be derived [29]:

$$V_{dc} = i_a^{(V1)} r_a + l_a \frac{di_a^{(V1)}}{dt} + e_a^{(V1)} - (i_b^{(V1)} r_b + l_b \frac{di_b^{(V1)}}{dt} + e_b^{(V1)}) \tag{2-46}$$

$$-V_{dc} = i_c^{(V1)} r_c + l_c \frac{di_c^{(V1)}}{dt} + e_c^{(V1)} - (i_a^{(V1)} r_a + l_a \frac{di_a^{(V1)}}{dt} + e_a^{(V1)}) \tag{2-47}$$

where the superscript $(V1)$ denotes the instantaneous value when the active vector $V1$ is applied (similar notation for the other 6 vectors including the zero vectors), i_a, i_b and i_c are the three phase currents, l_a, l_b and l_c are the three phase inductances, r_a, r_b and r_c are the three phase resistances, and e_a, e_b and e_c are the three phase back-EMFs.

Similarly, the equations when vector V4 is applied to the machine are:

$$-V_{dc} = i_a^{(V4)} r_a + l_a \frac{di_a^{(V4)}}{dt} + e_a^{(V4)} - (i_b^{(V4)} r_b + l_b \frac{di_b^{(V4)}}{dt} + e_b^{(V4)}) \tag{2-48}$$

$$V_{dc} = i_c^{(V4)} r_c + l_c \frac{di_c^{(V4)}}{dt} + e_c^{(V4)} - (i_a^{(V4)} r_a + l_a \frac{di_a^{(V4)}}{dt} + e_a^{(V4)}) \tag{2-49}$$

If the two test vectors are applied within a short period, then the back-EMF terms can be assumed equal, and the difference of the voltage drops across the resistor can be ignored. Then, combining (2-46) to (2-49), yields:

$$2V_{dc} = l_a(\frac{di_a^{(V1)}}{dt} - \frac{di_a^{(V4)}}{dt}) - l_b(\frac{di_b^{(V1)}}{dt} - \frac{di_b^{(V4)}}{dt}) \tag{2-50}$$

$$-2V_{dc} = l_c(\frac{di_c^{(V1)}}{dt} - \frac{di_c^{(V4)}}{dt}) - l_a(\frac{di_a^{(V1)}}{dt} - \frac{di_a^{(V4)}}{dt}) \tag{2-51}$$

Also, for a balanced system,

$$\frac{di_a}{dt} + \frac{di_b}{dt} + \frac{di_c}{dt} = 0 \tag{2-52}$$

Combining (2-50) to (2-52) gives:

$$\frac{di_a^{(V1)}}{dt} - \frac{di_a^{(V4)}}{dt} = \frac{l_b + l_c}{l_a l_b + l_b l_c + l_a l_c} \cdot 2V_{dc} \tag{2-53}$$

$$\frac{di_b^{(V1)}}{dt}-\frac{di_b^{(V4)}}{dt}=-\frac{l_c}{l_a l_b+l_b l_c+l_a l_c}\cdot 2V_{dc} \tag{2-54}$$

$$\frac{di_c^{(V1)}}{dt}-\frac{di_c^{(V4)}}{dt}=-\frac{l_b}{l_a l_b+l_b l_c+l_a l_c}\cdot 2V_{dc} \tag{2-55}$$

Then substituting the inductances from (2-43) to (2-45) into (2-53) yields:

$$\frac{di_a^{(V1)}}{dt}-\frac{di_a^{(V4)}}{dt}=\frac{2}{c_1}(2-\frac{\Delta l}{l_0}\cos(2\theta_\delta)) \tag{2-56}$$

where $c_1=3l_0(1-\frac{\Delta l^2}{4l_0^2})\cdot\frac{1}{V_{dc}}$, and can be considered constant.

Similar equations can be derived when other opposite vector pairs, V2/V5 and V3/V6 are applied to the machine, as:

$$\frac{di_b^{(V2)}}{dt}-\frac{di_b^{(V5)}}{dt}=\frac{2}{c_1}(2-\frac{\Delta l}{l_0}\cos(2\theta_\delta-\frac{2\pi}{3})) \tag{2-57}$$

$$\frac{di_c^{(V3)}}{dt}-\frac{di_c^{(V6)}}{dt}=\frac{2}{c_1}(2-\frac{\Delta l}{l_0}\cos(2\theta_\delta-\frac{4\pi}{3})) \tag{2-58}$$

A position vector can be constructed as:

$$\underline{p}=p_a+\alpha p_b+\alpha^2 p_c \tag{2-59}$$

Where $\alpha=e^{-j\frac{2\pi}{3}}$ represents the frame transformation, and $p_{a/b/c}$ are defined as:

$$p_a=\frac{\Delta l}{l_0}\cos(2\theta_\delta)=2-\frac{c_1}{2}(\frac{di_a^{(V1)}}{dt}-\frac{di_a^{(V4)}}{dt}) \tag{2-60}$$

$$p_b=\frac{\Delta l}{l_0}\cos(2\theta_\delta-\frac{2\pi}{3})=2-\frac{c_1}{2}(\frac{di_b^{(V2)}}{dt}-\frac{di_b^{(V5)}}{dt}) \tag{2-61}$$

$$p_c = \frac{\Delta l}{l_0}\cos(2\theta_\delta - \frac{4\pi}{3}) = 2 - \frac{c_1}{2}(\frac{di_c^{(V3)}}{dt} - \frac{di_c^{(V6)}}{dt}) \tag{2-62}$$

The resultant orthogonal components of this position vector $\underline{p}$ are obtained:

$$p_\alpha = p_a - \frac{1}{2}p_b - \frac{1}{2}p_c = \frac{3\Delta l}{2l_0}\cos(2\theta_\delta) \tag{2-63}$$

$$p_\beta = \frac{\sqrt{3}}{2}(p_b - p_c) = \frac{3\Delta l}{2l_0}\sin(2\theta_\delta) \tag{2-64}$$

The saliency angle is the angle of this position vector and can be obtained by:

$$2\theta_\delta = \arctan(\frac{p_\beta}{p_\alpha}) \tag{2-65}$$

It can be noticed that in order to establish the position vector $\underline{p}$, three pairs of opposite active vectors need to be applied while keeping the VTA (voltage time area) unaltered by the test vectors. Consequently, the test vectors are injected in null vectors ($V0$ and $V7$) whenever the position estimation is required. However, due to the high frequency oscillation of the di/dt signals induced by parasitic effects within the machine itself after each switching state, a minimum duration $t_{\min}$ of each test vector is required for accurate measurement of the di/dt signals. Therefore, there is not enough time for the three pairs of test vectors to be within one PWM cycle. The alternative is to put them in three neighbouring PWM periods [14], and the arrangement is illustrated in Figure 2.18. The disadvantage of this arrangement is that at higher frequencies the positions can be very different from neighbouring PWM periods and the estimation can be largely affected. Reference [14] reported a compensation scheme with estimation error reduced significantly.

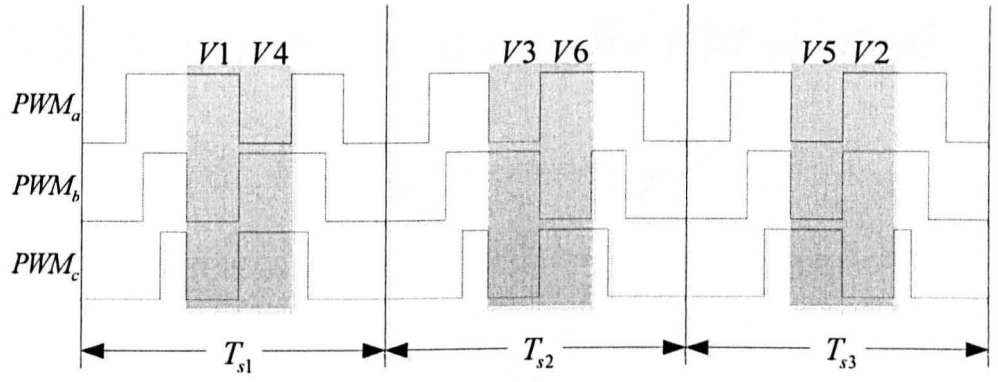

Figure 2.18: INFORM method test vectors injecting arrangement

An improved vector sequence for the INFORM method is proposed in [56], which introduces an extra pair of test vectors. For instance, when the pair of test vectors is $V3$ and $V6$, another pair of these vectors is added with half-length of each test vector as the sequence shown in Figure 2.19. With these extra vectors, current distortions due to the injection of test vectors can be reduced while the VTA remains unchanged.

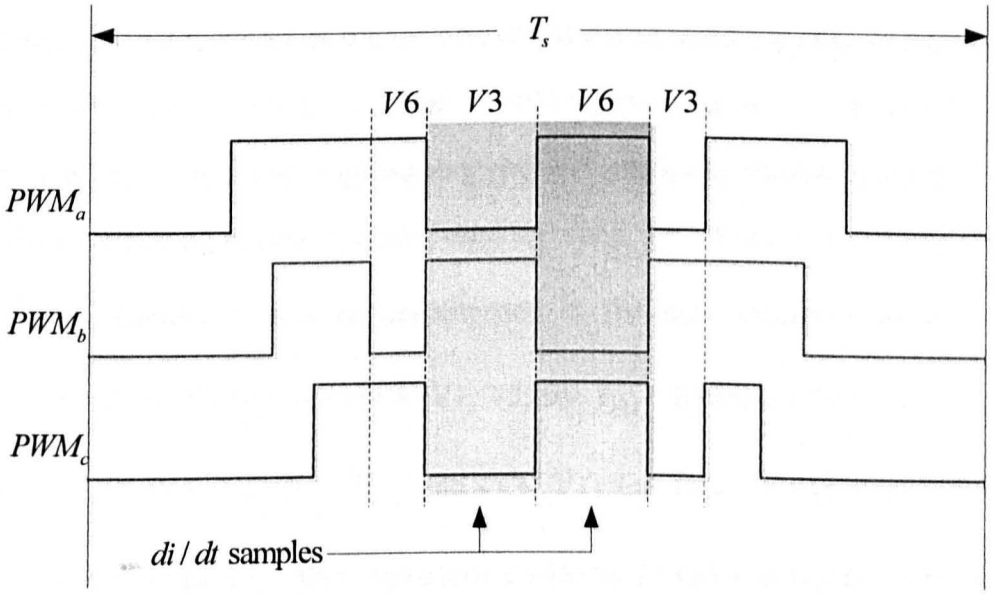

Figure 2.19: Improved test vector sequence of INFORM method

The INFORM method is not applicable in the full frequency range, since at higher frequencies, null vectors are generally very short resulting difficulty in injecting test vectors in the PWM sequence.

2.4.10 Saliency tracking by EM method

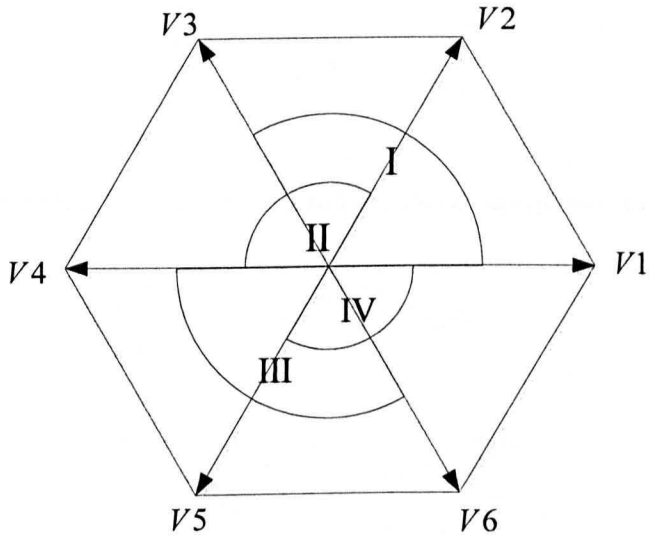

Figure 2.20: Definition of sectors for EM method

The INFORM method makes use of test vectors in addition to the fundamental PWM sequence, whilst the Extended modulation (EM) method proposed in [57] integrates the test vectors within a modified PWM sequence. Rather than using the standard six sector divisions of a SVPWM, four sectors (I, II , III , and IV) are defined by combining neighbouring two 60° sectors as shown in Figure 2.20. The overlapping regions are only used by I and IV. When a reference voltage $\underline{v}^{*}$ is demanded, it can be decomposed in the new extended sectors. The combination of active vectors is (V1, V3) for I_{EM} (Extended Sector I), (V2, V4) for II_{EM} , (V4, V6) for III_{EM} and (V5, V1) for IV_{EM}. Supposing a voltage demand falls in I_{EM}, then equations (2-66) to (2-68) can be derived for the application of active vector V1, neglecting the voltage drop across resistors and the back-EMF terms as only low frequency operation is considered.

$$\frac{di_a^{(V1)}}{dt} = \frac{l_b + l_c}{l_a l_b + l_b l_c + l_a l_c} \cdot V_{dc} \tag{2-66}$$

$$\frac{di_b^{(V1)}}{dt} = -\frac{l_c}{l_a l_b + l_b l_c + l_a l_c} \cdot V_{dc} \tag{2-67}$$

$$\frac{di_c^{(V1)}}{dt} = -\frac{l_b}{l_a l_b + l_b l_c + l_a l_c} \cdot V_{dc} \tag{2-68}$$

Then, substituting the inductances (2-43) to (2-45) into above equations, yields:

$$\frac{di_a^{(V1)}}{dt} = \frac{1}{c_1}(2 - \frac{\Delta l}{l_0}\cos(2\theta_\delta)) \tag{2-69}$$

$$\frac{di_b^{(V1)}}{dt} = -\frac{1}{c_1}(1 + \frac{\Delta l}{l_0}\cos(2\theta_\delta - \frac{2\pi}{3})) \tag{2-70}$$

$$\frac{di_c^{(V1)}}{dt} = -\frac{1}{c_1}(1 + \frac{\Delta l}{l_0}\cos(2\theta_\delta - \frac{4\pi}{3})) \tag{2-71}$$

where $c_1 = 3l_0(1 - \frac{\Delta l^2}{4l_0^2}) \cdot \frac{1}{V_{dc}}$, and again can be considered constant.

Consequently, the scalar position signals can be defined as:

$$p_{a1} = 2 - c_1 \frac{di_a^{(V1)}}{dt} \tag{2-72}$$

$$p_{b1} = -1 - c_1 \frac{di_c^{(V1)}}{dt} \tag{2-73}$$

$$p_{c1} = -1 - c_1 \frac{di_b^{(V1)}}{dt} \tag{2-74}$$

A similar approach can be applied to derive the position signals for the application of V3, giving:

$$p_{a3} = -1 - c_1 \frac{di_c^{(V3)}}{dt} \tag{2-75}$$

$$p_{b3} = 2 - c_1 \frac{di_b^{(V3)}}{dt} \tag{2-76}$$

$$p_{c3} = -1 - c_1 \frac{di_a^{(V3)}}{dt} \tag{2-77}$$

By carefully choosing appropriate position signals to apply to (2-59), a position vector can be obtained as:

$$\begin{aligned} p_\alpha &= -(p_{c3} - \frac{1}{2}p_{b1} - \frac{1}{2}p_{c1}) \\ &= -(-1 - c_1 \frac{di_a^{(V3)}}{dt}) + \frac{1}{2}[(-1 - c_1 \frac{di_c^{(V1)}}{dt}) + (-1 - c_1 \frac{di_b^{(V1)}}{dt})] \\ &= c_1(\frac{di_a^{(V3)}}{dt} - \frac{1}{2}\frac{di_c^{(V1)}}{dt} - \frac{1}{2}\frac{di_b^{(V1)}}{dt}) \\ &= \frac{3}{2}\frac{\Delta l}{l_0}\cos(2\theta_\delta) \end{aligned} \tag{2-78}$$

$$\begin{aligned} p_\beta &= \frac{\sqrt{3}}{2}(p_{b1} - p_{c1}) \\ &= \frac{\sqrt{3}}{2}[(-1 - c_1 \frac{di_c^{(V1)}}{dt}) - (-1 - c_1 \frac{di_b^{(V1)}}{dt})] \\ &= \frac{3}{2}\frac{\Delta l}{l_0}\sin(2\theta_\delta) \end{aligned} \tag{2-79}$$

It can be seen that by constructing this vector and applying to (2-65), the term $\frac{\Delta l}{l_0}$ can be eliminated to derive the final estimation of the saliency angle, which means no knowledge of machine inductance required. The selection of the position signals to form the vector is not unique, as in this case p_α can be also calculated as (2-80), and results remain the same.

$$p_\alpha = -\frac{1}{2}(p_{a1} + 2p_{c3}) \tag{2-80}$$

In addition to the modification of the sector division, a minimum time of at least

$t_{\min}$ for each active vector for accurate measurements of di/dt signals is required similar to that of the INFORM method mentioned before. For narrow vectors, the durations need to be extended to $t_{\min}$ and therefore compensation vectors need to be applied as well to provide the same VTA as demanded by the fundamental control scheme.

Figure 2.21 illustrates the final modified PWM sequence and the associated di/dt measurements when $\underline{v}^*$ resides in I_{EM}, with vector V4 compensating for extra V1 duration and V6 for that of V3.

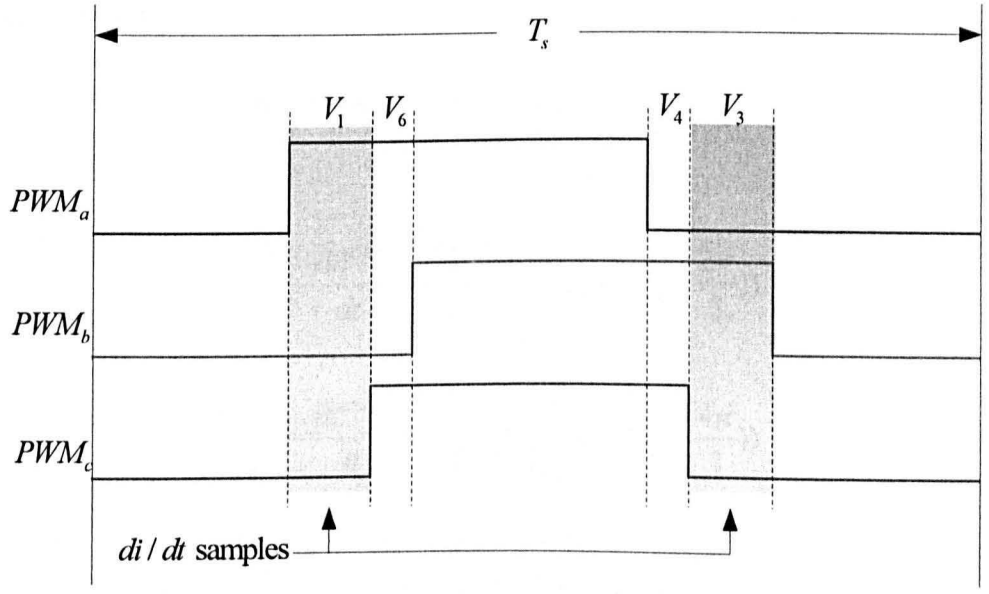

Figure 2.21: Modified PWM sequence of Extended Modulation method

It can be noted that the derivation of (2-66) to (2-71) is based on neglecting the back-EMF terms. Therefore, the EM method reported in [57] is not applicable at high frequencies as no compensation scheme for the large back-EMF terms is integrated and the analysis above is no longer consistent.

2.4.11 Saliency tracking by Fundamental PWM excitation method

Rather than modifying the PWM sequence as in the EM method, the fundamental PWM method proposed in [17, 20] utilizes, as indicated by its name, the fundamental PWM voltage vector excitation the machine. For example, supposing a vector $\underline{v}^*$ in sector I is demanded, it is decomposed with V1, V2 and null vectors (V0 and V7). When V1 and V0 are applied to the star-connected machine, as for the INFORM method, the following equations can be derived:

$$\frac{di_a^{(V1)}}{dt}-\frac{di_a^{(V0)}}{dt}=\frac{1}{c_1}(2-\frac{\Delta l}{l_0}\cos(2\theta_\delta)) \tag{2-81}$$

$$\frac{di_b^{(V1)}}{dt}-\frac{di_b^{(V0)}}{dt}=-\frac{1}{c_1}(1+\frac{\Delta l}{l_0}\cos(2\theta_\delta-\frac{2\pi}{3})) \tag{2-82}$$

$$\frac{di_c^{(V1)}}{dt}-\frac{di_c^{(V0)}}{dt}=-\frac{1}{c_1}(1+\frac{\Delta l}{l_0}\cos(2\theta_\delta-\frac{4\pi}{3})) \tag{2-83}$$

where $c_1=3l_0(1-\frac{\Delta l^2}{4l_0^2})\cdot\frac{1}{V_{dc}}$ can be considered as constant.

Three scalar position signals can be defined as:

$$p_{a1}=2-c_1(\frac{di_a^{(V1)}}{dt}-\frac{di_a^{(V0)}}{dt}) \tag{2-84}$$

$$p_{b1}=-1-c_1(\frac{di_c^{(V1)}}{dt}-\frac{di_c^{(V0)}}{dt}) \tag{2-85}$$

$$p_{c1}=-1-c_1(\frac{di_b^{(V1)}}{dt}-\frac{di_b^{(V0)}}{dt}) \tag{2-86}$$

By applying the same approach, another set of position signals using V2 and V0 can be defined as:

$$p_{a2} = -1 + c_1\left(\frac{di_b^{(V2)}}{dt} - \frac{di_b^{(V0)}}{dt}\right) \tag{2-87}$$

$$p_{b2} = -1 + c_1\left(\frac{di_a^{(V2)}}{dt} - \frac{di_a^{(V0)}}{dt}\right) \tag{2-88}$$

$$p_{c3} = 2 + c_1\left(\frac{di_c^{(V2)}}{dt} - \frac{di_c^{(V0)}}{dt}\right) \tag{2-89}$$

To avoid error caused by the uncertainty of the coefficient c_1, it is necessary to choose position signals with same offset to form a position vector $\underline{p}$. Therefore the $\alpha\beta$ components of this vector are given as (2-90) and (2-91), and the saliency position angle can be calculated without knowing c_1.

$$p_\alpha = p_{a2} - \frac{1}{2}p_{b1} - \frac{1}{2}p_{c1} \tag{2-90}$$

$$p_\beta = \frac{\sqrt{3}}{2}(p_{b1} - p_{c1}) \tag{2-91}$$

For demand voltage vectors located in the other five sectors, the position signals for each combination of an active vector and a null vector can also be obtained, and can be tabulated as Table 2.1. Similar results can be applied to a delta-connected machine.

Sampled Vectors	p_a	p_b	p_c
V1, V0	$2-c_1(\frac{di_a^{(V1)}}{dt}-\frac{di_a^{(V0)}}{dt})$	$-1-c_1(\frac{di_c^{(V1)}}{dt}-\frac{di_c^{(V0)}}{dt})$	$-1-c_1(\frac{di_b^{(V1)}}{dt}-\frac{di_b^{(V0)}}{dt})$
V2, V0	$-1+c_1(\frac{di_b^{(V2)}}{dt}-\frac{di_b^{(V0)}}{dt})$	$-1+c_1(\frac{di_a^{(V2)}}{dt}-\frac{di_a^{(V0)}}{dt})$	$2+c_1(\frac{di_c^{(V2)}}{dt}-\frac{di_c^{(V0)}}{dt})$
V3, V0	$-1-c_1(\frac{di_c^{(V3)}}{dt}-\frac{di_c^{(V0)}}{dt})$	$2-c_1(\frac{di_b^{(V3)}}{dt}-\frac{di_b^{(V0)}}{dt})$	$-1-c_1(\frac{di_a^{(V3)}}{dt}-\frac{di_a^{(V0)}}{dt})$
V4, V0	$2+c_1(\frac{di_a^{(V4)}}{dt}-\frac{di_a^{(V0)}}{dt})$	$-1+c_1(\frac{di_c^{(V4)}}{dt}-\frac{di_c^{(V0)}}{dt})$	$-1+c_1(\frac{di_b^{(V4)}}{dt}-\frac{di_b^{(V0)}}{dt})$
V5, V0	$-1-c_1(\frac{di_b^{(V5)}}{dt}-\frac{di_b^{(V0)}}{dt})$	$-1-c_1(\frac{di_a^{(V5)}}{dt}-\frac{di_a^{(V0)}}{dt})$	$2-c_1(\frac{di_c^{(V5)}}{dt}-\frac{di_c^{(V0)}}{dt})$
V6, V0	$-1+c_1(\frac{di_c^{(V6)}}{dt}-\frac{di_c^{(V0)}}{dt})$	$2+c_1(\frac{di_b^{(V6)}}{dt}-\frac{di_b^{(V0)}}{dt})$	$-1+c_1(\frac{di_a^{(V6)}}{dt}-\frac{di_a^{(V0)}}{dt})$

Table 2.1: Position signals obtained by di/dt measurements of each combination of active vector and null vector for a star-connected machine

It is noted that the null vector can be chosen from either V0 or V7 depending on the convenience of di/dt measurements. The rule for choosing appropriate position signals in constructing position vector is to cancel the offset as mentioned above.

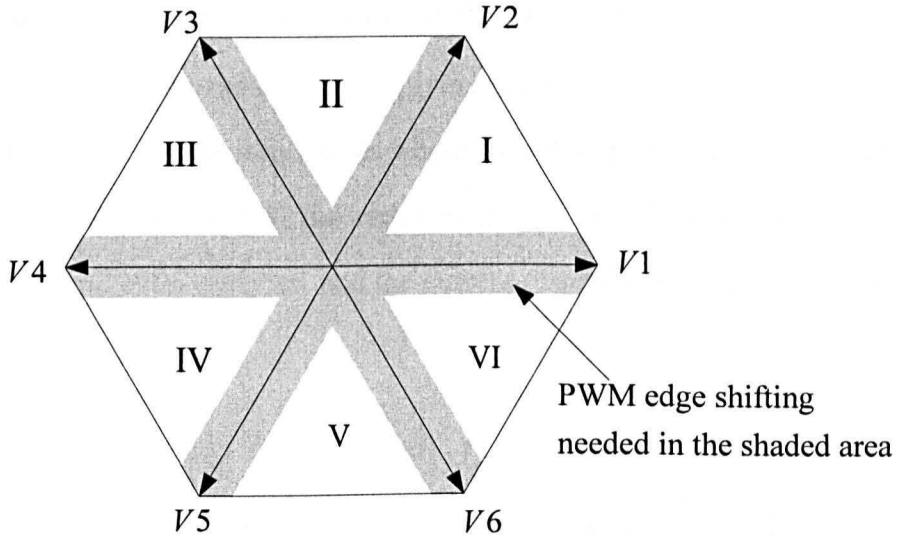

Figure 2.22: Locations of a demanded vector where a shifted PWM sequence is required

However, modification of the PWM sequence is also required for low modulation index region and for the cases when demanded voltage vector passes active vectors, the area where modification of PWM sequence is required is visualized in Figure 2.22. The difference compared with the EM method is that it does not change the active vectors applied in a normal PWM, and the only modification made is to shift corresponding PWM sequence to provide a duration of $t_{\min}$ for short vectors in the first half of the PWM period and their compensation is made in the second half of the period as shown in

Figure 2.23, assuming $\underline{v}^*$ residing in Sector I and extensions for both V1 and V2 required. Vector V1 is applied for the duration of $t_{\min}$ and its compensation V4 is applied for $(t_1 - t_{\min})$; V2 and its compensation V5 are applied for $t_{\min}$ and $(t_2 - t_{\min})$, respectively. Therefore, the mean voltage vector demanded from the inverter is conserved. Similar shifting can be utilized for vectors in the other five sectors and the results follow the above analysis. Theoretically this method can work in the whole operation range [17]. In the zero and low frequency situation

when modification of the fundamental PWM is required, current distortion is induced and can be reduced by applying active vectors in consecutive PWM periods [17]. At higher frequencies where the active vectors are longer due to the increase in the back-EMF, the requirement for modification of PWM pulses decreases and even vanishes, and the current distortion is consequently reduced significantly [17].

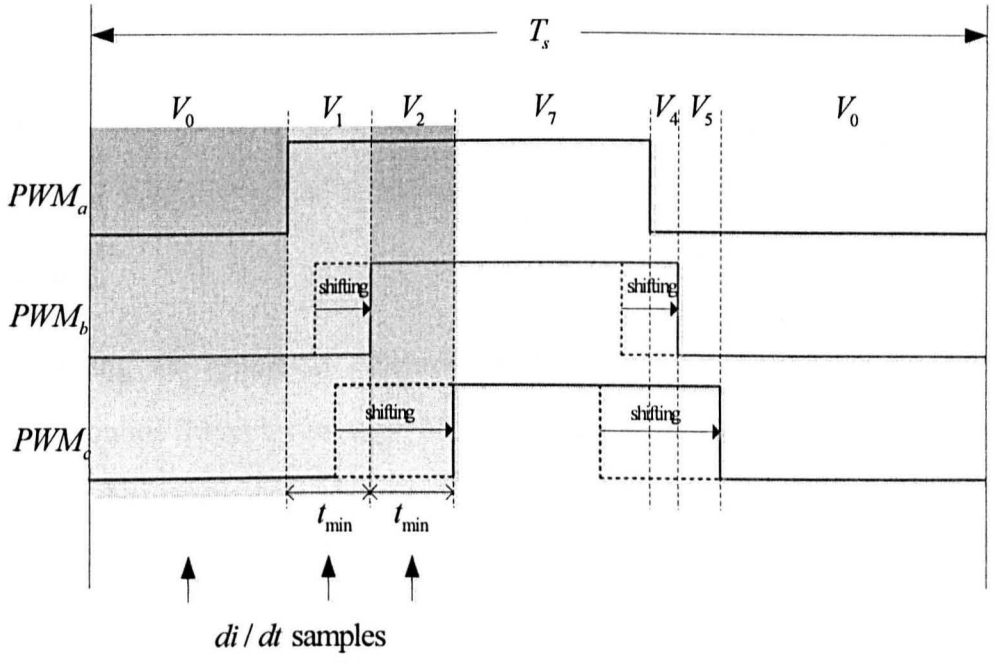

Figure 2.23: Edge shifting of a standard PWM sequence to provide sufficient time for di/dt measurements

2.4.12 Saliency tracking by Zero Vector method

Reference [58, 59] investigated the possibility of tracking the saliency position by measurements of zero sequence phase voltage/current caused by the unbalance nature of stator parameters. However, both of these two methods need to inject test vectors similar to the INFORM method, which suffers from the same limitations as the INFORM method as discussed previously.

Another approach which also makes use of the zero sequence information for position estimation was reported in [60]. It can be regarded as a combined method of saliency tracking and back-EMF based tracking technique.

Considering that a zero voltage vector is applied to the machine, the voltage equations in the real *dq* synchronous frame can be obtained as:

$$\begin{bmatrix} v_d^{(V0)} \\ v_q^{(V0)} \end{bmatrix} = \begin{bmatrix} R+pl_d & 0 \\ 0 & R+pl_q \end{bmatrix} \begin{bmatrix} i_d^{(V0)} \\ i_q^{(V0)} \end{bmatrix} + \begin{bmatrix} 0 \\ \psi_m \omega_r \end{bmatrix} = \begin{bmatrix} 0 \\ 0 \end{bmatrix} \tag{2-92}$$

Where superscript $(V0)$ represents the vector being applied, p denotes the derivate function, $\psi_m \omega_r$ is the back-EMF term, and cross coupling term is ignored.

Assuming the estimated synchronous frame is misaligned with the real *dq* synchronous frame by an angle of $\Delta\theta$, then applying transformation (2-93) to (2-92), the current derivative can be obtained as (2-94).

$$\begin{bmatrix} i_d^{(V0)} \\ i_q^{(V0)} \end{bmatrix} = \begin{bmatrix} \cos(\Delta\theta) & -\sin(\Delta\theta) \\ \sin(\Delta\theta) & \cos(\Delta\theta) \end{bmatrix} \begin{bmatrix} \hat{i}_d^{(V0)} \\ \hat{i}_q^{(V0)} \end{bmatrix} \tag{2-93}$$

$$\begin{bmatrix} \frac{d\hat{i}_d^{(V0)}}{dt} \\ \frac{d\hat{i}_q^{(V0)}}{dt} \end{bmatrix} = \frac{R}{l_d l_q} \begin{bmatrix} (l_d - l_q)\cos^2(\Delta\theta) - l_d & \frac{1}{2}(l_q - l_d)\sin(2\Delta\theta) \\ \frac{1}{2}(l_q - l_d)\sin(2\Delta\theta) & (l_q - l_d)\cos^2(\Delta\theta) - l_q \end{bmatrix} \begin{bmatrix} \hat{i}_d^{(V0)} \\ \hat{i}_q^{(V0)} \end{bmatrix} - \frac{\psi_m \omega_r}{l_q} \begin{bmatrix} \sin(\Delta\theta) \\ \cos(\Delta\theta) \end{bmatrix} \tag{2-94}$$

Using closed loop control, the $\hat{i}_d^{(V0)}$ term is controlled to zero. Therefore, (2-94) can be rearranged to:

$$\begin{bmatrix} \frac{d\hat{i}_d^{(V0)}}{dt} \\ \frac{d\hat{i}_q^{(V0)}}{dt} \end{bmatrix} = \frac{R}{l_d l_q} \hat{i}_q^{(V0)} \begin{bmatrix} \frac{1}{2}(l_q - l_d)\sin(2\Delta\theta) \\ (l_q - l_d)\cos^2(\Delta\theta) - l_q \end{bmatrix} - \frac{\psi_m \omega_r}{l_q} \begin{bmatrix} \sin(\Delta\theta) \\ \cos(\Delta\theta) \end{bmatrix} \quad (2\text{-}95)$$

Then by forcing $\frac{d\hat{i}_d^{(V0)}}{dt}$ to zero, the misalignment can be compensated and an estimation of the position can be achieved. In [18], a modified demodulation scheme was proposed to allow the estimation over the full operation region (i.e. all four quadrants). However, the performance of this method is still limited at the low speed no load condition, since under this condition, the saliency tracking taking over is the back-EMF tracking and the error magnitude is zero due to the lack of torque current.

2.5 Conclusion

In this chapter, a variety of methods for sensorless vector control of permanent magnet machines has been reviewed. Each of the methods has been described in terms of the principle, implementation and limitations. For a commercial application, it is essential to bear in mind the advantages and disadvantages in association with all possible methods and then choose the most suitable one. A comparison of the methods mentioned in this chapter has been made regarding the following aspects and conclusions have been drawn.

In terms of hardware usage and implementation complexity, model based methods have shown superiority over other methods. The measurements required for these methods can be limited to phase currents measurements, which is similar to that for high frequency injection methods. However, most of the model based methods rely on much less signal processing than that of high frequency injection methods. The current derivative methods on the other hand,

consume the most hardware resources compared with the other two categories. Additional current derivative sensors are sometimes required for acquisition of high resolution current derivative measurements, although multiple phase current measurements can replace direct current derivative measurements, adding more requirements to the signal processing and resulting in poorer performance. More complex modifications to sampling arrangements for the fundamental PWM sequence have to be incorporated for these methods to work.

Considerating the operating range, model based methods work well at medium and high speed but deteriorate with a decrease of speed. Zero and low speed control is still difficult to achieve. The *hf* injection methods are well suited for zero and low speed and limited for a higher speed. The INFORM and EM method can also work well under zero/low speed range while the fundamental PWM method can work ranging from zero to a high speed range. Zero vector current derivative method has poorer performance with the decrease of load level in the low speed region.

Several factors affect the estimation quality, such as inverter non-linearity and mechanical disturbances of the machine itself. An effective disturbance elimination procedure is therefore essential for the final implementation of the control. Model based methods can provide disturbance elimination such as the use of Kalman filter or other compensation schemes for inverter compensation. For the *hf* injection method, rotation signal injection is suited to disturbance elimination schemes due to its phase dependent tracking nature, and similar approaches can be applied to most current derivative methods. On the other hand, pulsating signal injection normally utilizes the amplitude of the stator current, and there are few measures for disturbance elimination and thus a poorer estimation quality is expected compared with other methods.

The advantages of the pulsating type *hf* signal injection method is that firstly a

low torque ripple is generated if injecting onto the flux producing axis, where in other signal injection methods and most current derivative methods the torque ripple is generally considered as an issue; secondly, with the pulsating signal injection, audible noise is kept minimum comparing with other methods except model based methods. Although audible noise can be reduced using pulsating signal injection, it is still significant for applications such as electrically powered steering system of this research. Modifications are required to further reduce the noise which will be discussed in following chapter.

Chapter 3 Random Frequency Sinusoidal Injection and Square wave Injection methods for audible noise reduction

3.1 Introduction

When using sensorless motor control wih a high frequency signal injection method, the frequency of the injection can be clearly heard and can be uncomfortable. The injection signal manifests itself as noise by creating mechanical vibration in many of the motor components, e.g. in the winding, in the motor casing. Other things cause acoustic noise as well, for example, air displacement due to the rotating of the rotor, but the dominant one is usually the high frequency signal injection which can range from several hundred Hz to several kHz. In automotive applications, this high audible noise makes it unsuitable. In [21], the additional audible noise caused by the *d-axis* injection method and fundamental PWM method [56], [17], [20], [43] was compared and the sound performance with the current derivative method was reported to be better than the injection method since the high frequency components are spread over a range of frequencies. To improve the hearing experience for the injection

based methods, a similar frequency spread can be achieved by using a random frequency injection instead of a fixed one. Thus, the sound introduced by the injection will be heard as a spread of components rather than a fixed tone, and due to the non-linearity of human hearing (see Chapter 4), some of the components will be highly attenuated, which will reduce the perception of the noise.

An alternative approach has been proposed to reduce the perception of noise, where the injection frequency is raised towards the PWM frequency- in this case using a square wave [52]. If the switching frequency is high enough (20 kHz in this work), the resultant noise component will be at a frequency that is rather attenuated by the human hearing. Therefore, a reduction of the audible noise can also be achieved.

These two methods are discussed in this chapter.

3.2 The Random *hf* Sinusoidal Injection method

3.2.1 Introduction

A novel approach to reducing the perception of noise for an injection based sensorless control is to randomly spread the injection frequency over a specified frequency range. The aim here is to combine the ease of implementation of the d-axis injection method, with the spread of frequencies associated with the fundamental PWM method. The approach is similar to that proposed for reducing the perception of PWM associated audible noise, by using random carrier frequencies, as proposed in [61, 62]. The aim of this part of the investigation is therefore to ensure that if a random *hf* injection frequency is

employed, it will not affect the behaviour of the sensorless algorithm.

The overall control structure of the implemented random *hf* sinusoidal injection method is shown in Figure 3.1.The random frequency injection method is quite similar to fixed frequency sinusoidal injection. In this section, its operation will be covered and the implementation of the method will be presented.

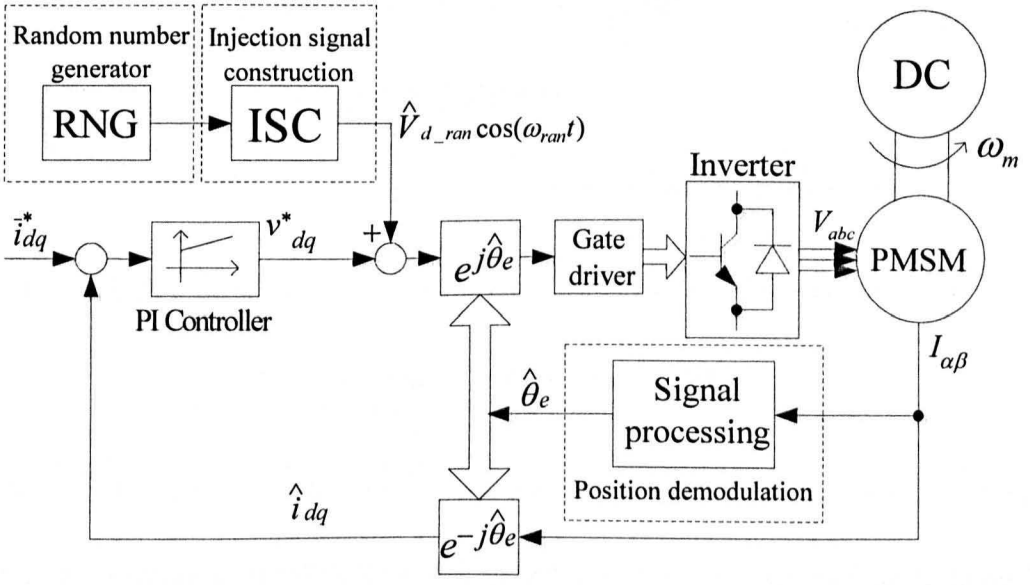

Figure 3.1: The overall control structure of the PMAC drive system with random *hf* sinusoidal injection method

3.2.2 Random number generation

In digital implementations, truly random sequences are difficult to realize since only predicted values can be generated by the processor. Consequently, a pseudo random sequence is generally chosen. There are several ways of creating pseudo random sequences. The feedback shift register [63] has been chosen as the pseudo random sequence generator due to its ease for implementing digitally. It is suitable for the DSP-based control platform of the experimental rig. A 16-bit feedback shift register is used in this work and the structure is shown as in Figure 3.2.

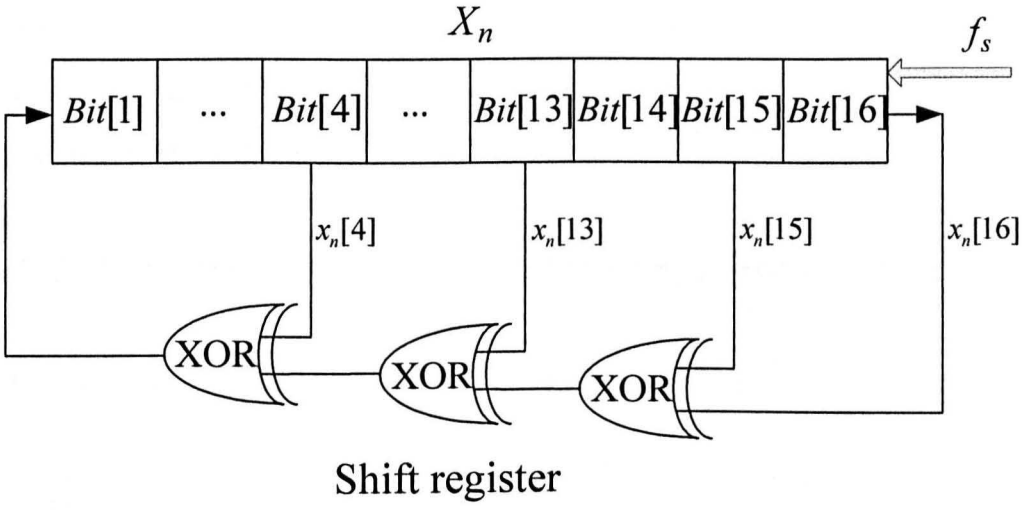

Figure 3.2: Structure of a 16-bit Feedback Shift Register

The random number generation process can be illustrated mathematically as:

$$X_n = (x_{n-1}[4] \oplus x_{n-1}[13] \oplus x_{n-1}[15] \oplus x_{n-1}[16]) \cdot 2^{15} + (X_{n-1} >> 1) \qquad (3\text{-}1)$$

Where X_n is the present value of the random number, X_{n-1} is the last updated value, $\oplus$refers to the Exclusive-Or operation, and $>>$is the logical right-shift operation.

The generator is processed at a fixed clock rate of 20 kHz which equals to the sampling rate of the system. An Exclusive-OR function is performed at each clock cycle combining the 4th, 13th, 15th and the last bit of the register, and the product is input to the first bit after a logical right-shift of the previous 16-bit sequence. In this way, the 16-bit sequence will go through 65535 distinct states $(2^{16}-1)$ before it repeats itself again. If the number of bit is chosen too small, the sequence will be soon repeated resulting in a poor randomness. If a higher number of bits are chosen, a larger number of distinct states will be generated and hence more randomness is expected with the cost of additional memory required in a practical fixed-point processor. In fact, with a 16-bit register updating at a rate of 20 kHz, the generated pattern will repeat itself in 3.3

seconds which is adequate for a motor drive application and is therefore chosen in this research. It should be noted that a non-zero initial value should be assigned to the shift register.

3.2.3 Construction of the injection signal

The constructed random frequency signal can be defined as:

$$\begin{bmatrix} \hat{v}_{\delta h} \\ \hat{v}_{\gamma h} \end{bmatrix} = k(f)\begin{bmatrix} \cos(2\pi(f_i+f_{ran})\cdot t) \\ 0 \end{bmatrix} = k(f)\begin{bmatrix} \cos(2\pi f\cdot t) \\ 0 \end{bmatrix}, \qquad f_{ran} \in [-f_{random}, +f_{random}] \tag{3-2}$$

where the superscript denotes that the injection voltage vector is considered in the estimated saliency $\hat{\delta}$-$\hat{\gamma}$ frame (for convenience, it is referred as the estimated *dq* frame in the following contents), $k(f)$ is a function depending on different injection frequencies, f_i is the centre frequency of the selected random range, f_{ran} is the instantaneous random frequency, f_{random} is the range of the random frequency, and $f = f_i + f_{ran}$ is the instantaneous injection frequency.

In order to derive the function $k(f)$, different injection frequencies have been applied to the PM motor with the fixed injection method. When these injection frequencies are applied, to ensure the amplitudes of the resultant different frequency *hf* currents do not change with the injection frequencies being applied (about 1.1A for each of the side bands), different injection voltages are used and the values are plotted in Figure 3.3. From Figure 3.3, a linearized approximation of the function $k(f)$ can be obtained as:

$$k(f) = 0.0006f + 0.4 \tag{3-3}$$

and equation (3-4) can be obtained:

$$\frac{V_i}{2\pi f_i} = \frac{k(f)}{2\pi f} = c \tag{3-4}$$

where V_i is the amplitude of the *hf* injection voltage in the fixed *hf* injection method with the resultant *hf* current amplitude around 1.1A, and c is a constant.

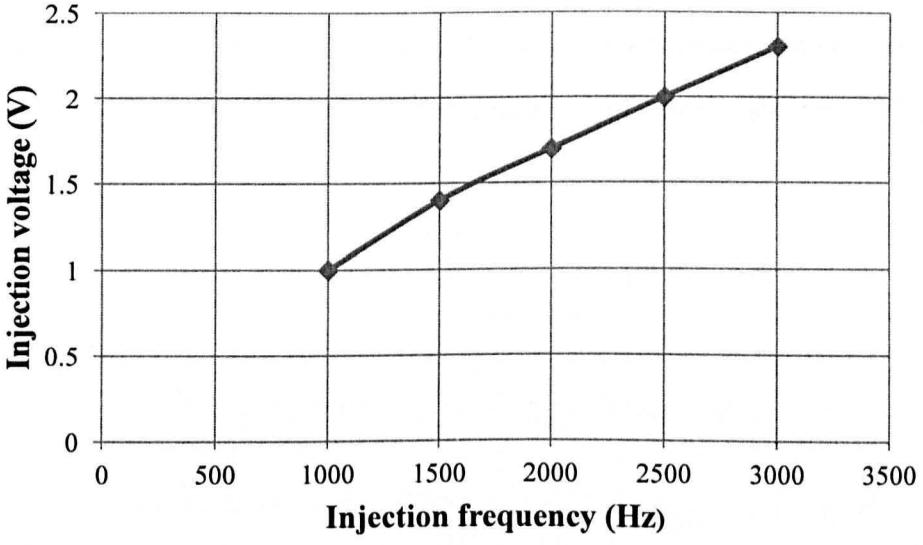

Figure 3.3: Plot of injection voltages against different injection frequencies with the same *hf* current amplitude

Applying (3-1), the random injection frequency range is derived as:

$$f_{random} = \frac{X_n}{m} \tag{3-5}$$

where m is a scaling factor to choose appropriate frequency range.

The choice of the injection frequency range should satisfy certain requirements in order to maintain a good control performance. Thus, the lower range of the frequency cannot be too low otherwise it will interfere with the current controller operation, and the upper range of the frequency cannot be too high to avoid the injection signal being highly stepped due to the limitation of the

switching frequency (20 kHz) as explained in [13]. On the other hand, it needs to be spread widely and randomly enough to allow the reduction of audible noise and improve the hearing experience. Some compromises need to be made to meet both requirements in a practical application. In this research, the centre injection frequencies have been chosen as 1.5 kHz and 2 kHz respectively to match the previous work in [13], and the random ranges of ±328 Hz and ±656 Hz have been chosen to allow the reduction of audible noise while maintaining good sensorless control performance. The generated injection voltage over 20ms for a frequency range of (1500±328) Hz random injection is shown in Figure 3.4.

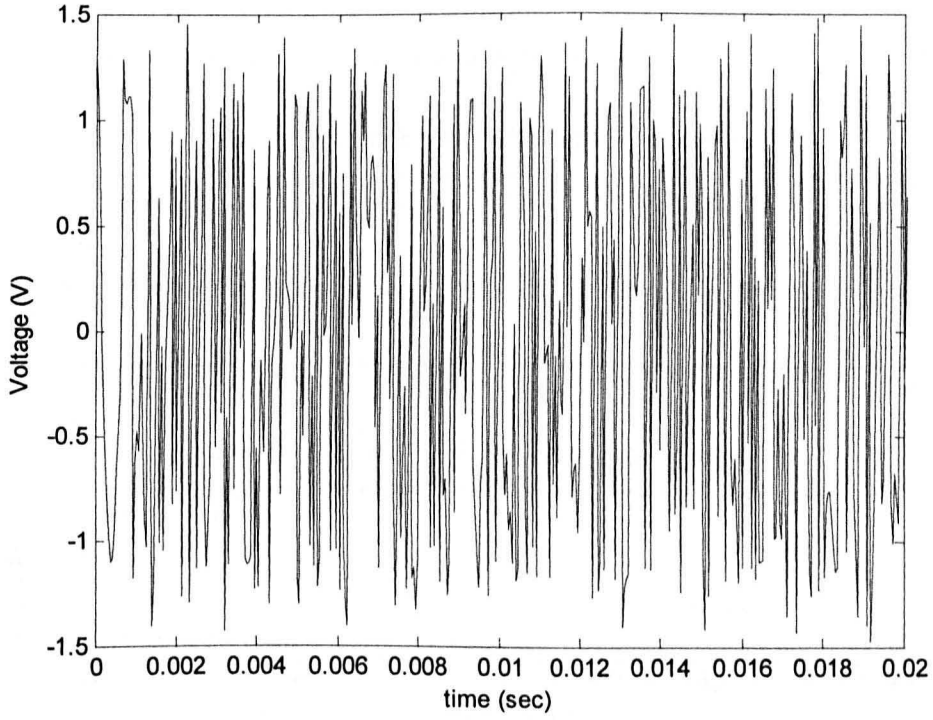

Figure 3.4: The generated random injection voltage with (1500±328) Hz random range

The results for the measured audible noise and the sensorless control with these frequencies will be compared and discussed in Chapter 6.

With appropriate selection of the injection voltage as described above, the

resultant *hf* current can be spread randomly. The wider the frequency range is, the more spread of the power of the *hf* current components. This can be illustrated by the spectrum of the line current obtained through rectangular windowed FFT operations with zoomed area regarding the *hf* current components for a fixed injection at 1.5 kHz and two random injections at (1500±328) Hz (1500±656) Hz, as shown in Figure 3.5.

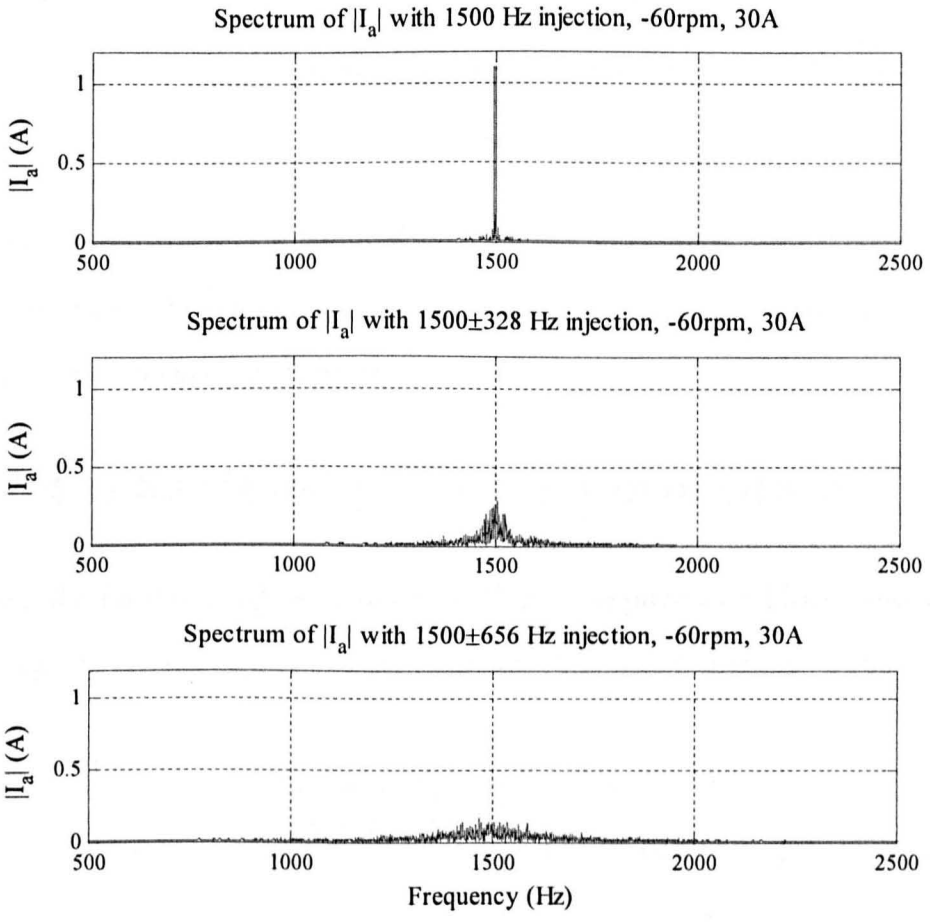

Figure 3.5: Spectra of the line currents for fixed 1500 Hz and random (1500±328) Hz, (1500±656) Hz injection at -60rpm under 30A load with sensored operation

Figure 3.5 also indicates that the reduction of the acoustic noise due to injection can be achieved by random injection as the *hf* current components spread as expected. Details of issues related to acoustic noise will be given in Chapter 6.

The power of the *hf* current components for the three injection types are calculated by summing up the related frequency components (for fixed injection, the power of the amplitude of the two side bands around the injection frequency is summed, and for random injection, the power of the amplitude of the components within the frequency range is summed) and is shown in Table 3.1.

	1500 Hz	(1500±328) Hz	(1500±656) Hz
Total Power (A^2)	2.5216	2.4682	2.4553

Table 3.1: The calculated *hf* current power for fixed and random hf injection method

As noted from Table 3.1, the total power of the resultant *hf* current components for the fixed and random injection methods are comparable, which demonstrates that the total power are preserved.

3.2.4 The signal processing procedure

When the pulsating signal as given in (3-2) is applied to a PMAC motor, the resultant *hf* current response in the estimated reference frame can be obtained as:

$$\begin{bmatrix} \hat{i}_{\delta h} \\ \hat{i}_{\gamma h} \end{bmatrix} = \eta(f) \cdot \frac{k(f)\sin(2\pi f \cdot t)}{2\pi f(L_s^2 - \Delta L_s^2)} \begin{bmatrix} L_s + \Delta L_s \cos(2\Delta\hat{\theta}_\delta) \\ -\Delta L_s \sin(2\Delta\hat{\theta}_\delta) \end{bmatrix} \tag{3-6}$$

where L_s the average inductance, ΔL_s the difference in inductance between the d and q axes, $\Delta\hat{\theta}_\delta$ the error between the real and the estimated rotor position [19], and $\eta(f)$ is a variable dependent on the integration of the random frequency variable f.

To see the effect of $\eta(f)$ on the resultant *hf* current components, both the fixed

and random *hf* injection were applied into the real *d-axis*. The resultant *hf* current vector in the real *dq* frame can be obtained by applying equation (3-4) and $\Delta\hat{\theta}_{\delta}=0$ to (3-6), yielding:

$$\begin{bmatrix} i_{dh} \\ i_{qh} \end{bmatrix} = \eta(f)\cdot\frac{c\cdot\sin(2\pi f\cdot t)}{L_d}\begin{bmatrix} 1 \\ 0 \end{bmatrix} \tag{3-7}$$

where i_{dh} and i_{qh} represent the *hf* current components in the real *dq* frame, L_d is the *d-axis* inductance, and for the fixed injection $\eta(f)$ equals 1. Then, the vector was observed on an arbitrary frame, namely $d_{obs}q_{obs}$ frame, shifted from the real *dq* frame by an angle θ_{obs} ranging from 0 degree to 360 degrees, equation (3-7) can be rearranged to the new frame as:

$$\begin{aligned}\begin{bmatrix} i_{dh}^{obs} \\ i_{qh}^{obs} \end{bmatrix} &= \begin{bmatrix} \cos\theta_{obs} & \sin\theta_{obs} \\ -\sin\theta_{obs} & \cos\theta_{obs} \end{bmatrix}\cdot\begin{bmatrix} i_{dh} \\ i_{qh} \end{bmatrix} \\ &= \eta(f)\cdot\frac{c\cdot\sin(2\pi f\cdot t)}{L_d}\begin{bmatrix} \cos\theta_{obs} \\ -\sin\theta_{obs} \end{bmatrix}\end{aligned} \tag{3-8}$$

where i_{dh}^{obs} and i_{qh}^{obs} are the current components observed from the arbitrary $d_{obs}q_{obs}$ frame. By multiplying (3-8) by the carrier $\sin(2\pi f\cdot t)$ and passing through a low pass filter, the DC value can be obtained as:

$$\begin{aligned} &LPF(\sin(2\pi f\cdot t)\cdot\begin{bmatrix} i_{dh}^{obs} \\ i_{qh}^{obs} \end{bmatrix}) = LPF(\eta(f)\cdot\frac{c\cdot(1-\cos(4\pi f\cdot t))}{2L_d}\begin{bmatrix} \cos\theta_{obs} \\ -\sin\theta_{obs} \end{bmatrix}) \\ &\Rightarrow\begin{bmatrix} i_{dh}^{'} \\ i_{qh}^{'} \end{bmatrix} = \eta(f)\cdot\frac{c}{2L_d}\begin{bmatrix} \cos\theta_{obs} \\ -\sin\theta_{obs} \end{bmatrix}\end{aligned} \tag{3-9}$$

where $LPF()$ represents the low pass filtering operation, and $i_{dh}^{'}$, $i_{qh}^{'}$ are the DC values. The scheme to obtain these values is shown in Figure 3.6.

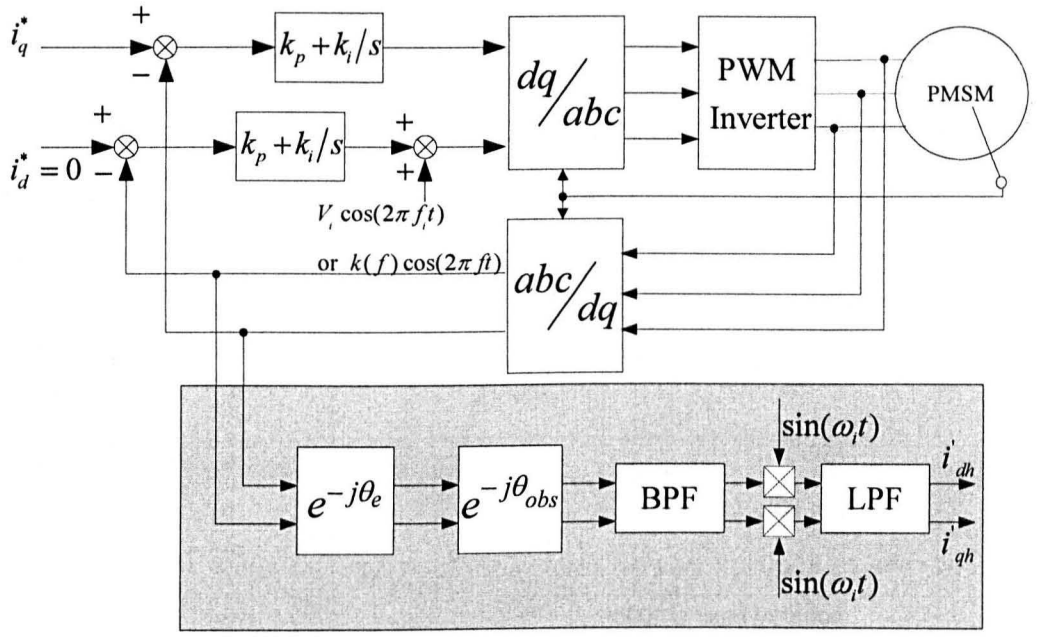

Figure 3.6: The scheme to obtain the amplitude of *hf* current vector with different observation coordinates

The values of i'_{qh} for both fixed and random *hf* injection are plotted in Figure 3.7, where the injection frequencies are 1.5 kHz and (1500±328) Hz, and the motor was operated under 30A sensored control at -60rpm.

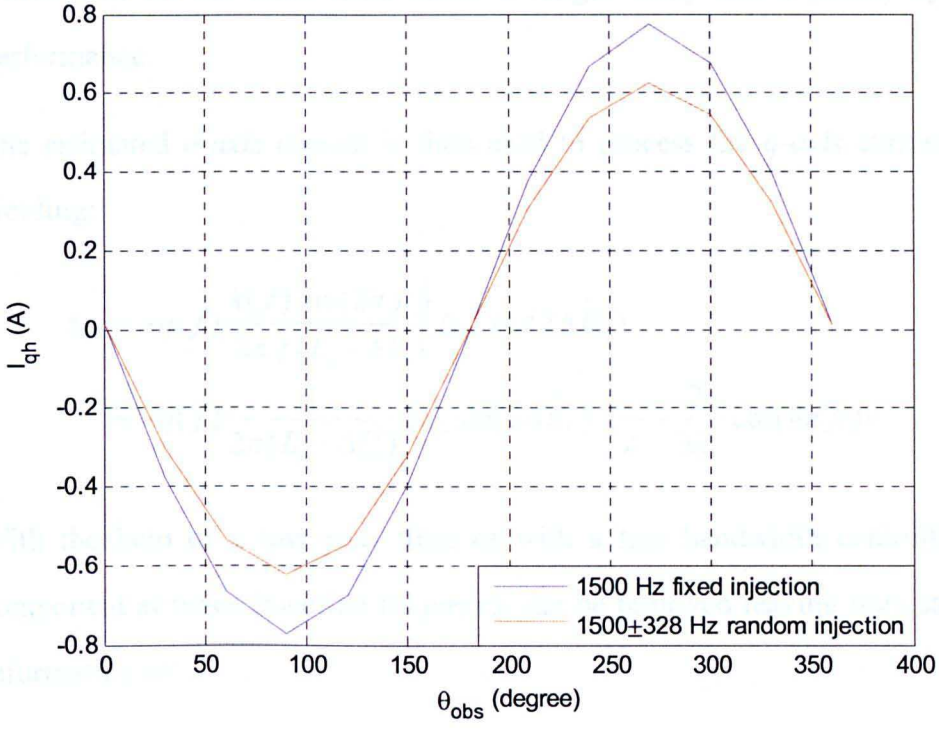

Figure 3.7: The values of $i_{qh}^{'}$ with 1.5 kHz and (1500±328) Hz injection under 30A, -60rpm sensored operation

It is noted from Figure 3.7 that the values of $i_{qh}^{'}$ for both 1.5 kHz fixed injection and (1500±328) Hz random injection are proportional to the sine of θ_{obs}. $\eta(f)$ for the random injection can be regarded as a constant scaling factor. Hence, the demodulation scheme for the random injection method can use the same structure as that used for the fixed frequency injection method shown in Figure 2.13. The current vector in the stationary frame is transformed into the estimated rotor rotating frame and a band pass filter is used to obtain the *hf* currents as in (3-6). Since a spread of frequency components are injected, a band pass filter with a wider bandwidth than that for a fixed frequency injection is needed to allow the *hf* signals in the whole injection range to be extracted from the measured currents. This however makes it difficult to filter out noise in this extended frequency range. To filter out the noise, higher order filters can be used,

which will on the other hand cause a longer delay and a poorer dynamic performance.

The estimated *d-axis* current is then used to process the *q-axis* current [64], yielding:

$$\begin{aligned}\Delta\gamma &= -\eta(f)\frac{k(f)\left|\sin(2\pi ft)\right|}{2\pi f(L_s^2-\Delta L_s^2)}\Delta L_s\sin(2\Delta\hat{\theta}_\delta)\\ &\approx -\eta(f)\frac{1}{2\pi(L_s^2-\Delta L_s^2)}\Delta L_s\sin(2\Delta\hat{\theta}_\delta)\cdot(\frac{2}{\pi}-\frac{2}{3\pi}\cdot\cos(4\pi ft))\end{aligned} \tag{3-10}$$

With the help of a low pass filter or with a low bandwidth controller, the component at twice injection frequency can be removed leaving only saliency information as:

$$\Delta\gamma \approx -\eta(f)\frac{4\cdot\Delta L_s}{2\pi^2(L_s^2-\Delta L_s^2)}\Delta\hat{\theta}_\delta \tag{3-11}$$

The signal above can then be driven to zero via a tracking scheme to achieve correct angle estimation. The tracking scheme used here is a mechanical observer [19] and will be further discussed in Chapter 4.

3.3 Square wave injection method

The square wave injection method [52], [54] uses either a pulsating or a rotating square wave voltage vector as the injection voltage to inject into either *d-axis* or *α-β axes*. In this work, a *d-axis* pulsating square wave injection was used in order to keep the torque ripple due to the injection at a minimum.

3.3.1 The principle of the method

The injected pulsating square wave type vector can be illustrated by Figure 3.8.

It is defined as:

$$\hat{v}_{\delta h} = \begin{cases} +V_i & , (n-1)T_i < t \le \dfrac{(2n-1)T_i}{2} \\ -V_i & , \dfrac{(2n-1)T_i}{2} < t \le nT_i \end{cases} \quad , \quad n = 1,2,3... \tag{3-12}$$

$$\hat{v}_{\gamma h} = 0$$

where $\hat{v}_{\delta h}$ and $\hat{v}_{\gamma h}$ are the injection voltage in the estimated dq frame, V_i is the amplitude of the square wave, and T_i is the period of the square wave signal. To achieve the goal of audible noise reduction, the frequency of the square wave signal needs to be as high as possible. In this research, 10 kHz is chosen as the injection frequency (i.e. $T_i = 100\mu s$), and a sampling frequency of 20 kHz equal to the switching frequency is used.

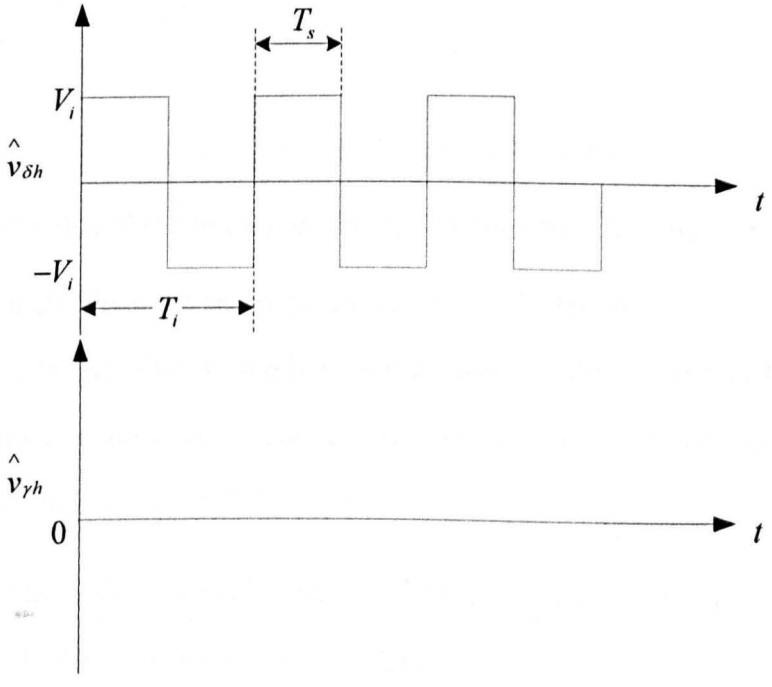

Figure 3.8: Square wave *hf* injection voltage vector

When a voltage vector as (3-12) is injected into the estimated *d-axis*, the resultant *hf* current derivative signals in the estimated reference frame can be

written as:

$$\frac{d}{dt}\begin{bmatrix}\hat{i}_{\delta h}\\ \hat{i}_{\gamma h}\end{bmatrix}=\frac{V_i}{2L_\delta L_\gamma}\begin{bmatrix}L_s+\Delta L_s\cos(2\Delta\hat{\theta}_\delta)\\ \Delta L_s\sin(2\Delta\hat{\theta}_\delta)\end{bmatrix},\quad \text{when } \hat{v}_{\delta h}>0$$
$$\frac{d}{dt}\begin{bmatrix}\hat{i}_{\delta h}\\ \hat{i}_{\gamma h}\end{bmatrix}=\frac{-V_i}{2L_\delta L_\gamma}\begin{bmatrix}L_s+\Delta L_s\cos(2\Delta\hat{\theta}_\delta)\\ \Delta L_s\sin(2\Delta\hat{\theta}_\delta)\end{bmatrix},\quad \text{when } \hat{v}_{\delta h}<0 \tag{3-13}$$

When the time interval between two current samples is short enough, the derivative of the currents can be approximated by subtracting the previous current sample from the present sample, then equation (3-13) becomes:

$$\begin{bmatrix}\Delta\hat{i}_{\delta h}\\ \Delta\hat{i}_{\gamma h}\end{bmatrix}=\frac{V_iT_i}{2L_\delta L_\gamma}\begin{bmatrix}L_s+\Delta L_s\cos(2\Delta\hat{\theta}_\delta)\\ \Delta L_s\sin(2\Delta\hat{\theta}_\delta)\end{bmatrix},\quad \text{when } \hat{v}_{\delta h}>0$$
$$\begin{bmatrix}\Delta\hat{i}_{\delta h}\\ \Delta\hat{i}_{\gamma h}\end{bmatrix}=\frac{-V_iT_i}{2L_\delta L_\gamma}\begin{bmatrix}L_s+\Delta L_s\cos(2\Delta\hat{\theta}_\delta)\\ \Delta L_s\sin(2\Delta\hat{\theta}_\delta)\end{bmatrix},\quad \text{when } \hat{v}_{\delta h}<0 \tag{3-14}$$

where $\Delta\hat{i}_{\delta h}$ and $\Delta\hat{i}_{\gamma h}$ represent the difference between the present value and the previous value of the *hf* current, and T_i is the period of the square wave signal. In this research, since the sampling frequency is 10 kHz, the above equation can be considered valid. The chosen injection voltage for this research is 3V to avoid control failure at high load. This is because the the output capability of the inverter is limited by the 12V DC link.

In a similar manner to the other demodulation methods, an error signal can be constructed to drive the estimation mechanism as:

$$\begin{aligned}\xi &= sign(\hat{v}_{\delta h})\cdot\Delta\hat{i}_{\gamma h}\\ &=\frac{V_iT_i}{2L_\delta L_\gamma}\cdot\Delta L_s\sin(2\Delta\hat{\theta}_\delta)\approx\frac{V_iT_i}{L_\delta L_\gamma}\cdot\Delta L_s\Delta\hat{\theta}_\delta\end{aligned} \tag{3-15}$$

3.3.2 The signal processing procedure

The demodulation scheme is shown in Figure 3.9.

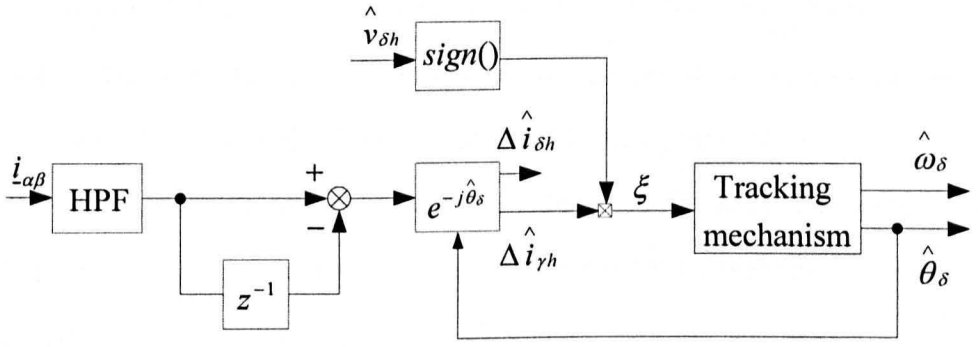

Figure 3.9: The demodulation scheme of the square wave *d-axis* injection method

In Figure 3.9, z^{-1} represents a unit delay which gives the previous sample's value of the sampled *hf* current signal. It can be seen that the sampled current vector in the stationary frame first passes through a high pass filter instead of a band pass filter as used in other *d-axis* demodulation schemes. This is because the injection frequency 10 kHz is half of the sampling frequency, while for a valid implementation of the digital band pass filter centred at 10 kHz, the sampling frequency is not high enough. Therefore, a high pass filter with a cut-off frequency at 1 kHz is used. The tracking mechanism is a mechanical observer which will be described in Chapter 4 from page 101.

3.4 Sensorless results for the two methods

The aforementioned two methods have been tested in the experimental rig which will be described in detail in Chapter 4. The motor was running at -60rpm under different load levels. The sensorless results are shown in the following sections.

3.4.1 Sensorless results for the random *hf* sinusoidal injection method

The centre frequency for the proposed random *hf* sinusoidal injection is chosen at 1.5 kHz. The random injection frequency ranges are set at ±328 Hz and ±656 Hz with 4^{nd} order and 6^{th} order butterworth band pass filters with 660 Hz and 1300 Hz bandwidth for each frequency range. A fixed injection method with 1.5 kHz injection frequency was used as a benchmark to evaluate the performance of the random injection method.

The results for sensorless operation under no load, 30A (33%) load and 60A (66%) load are shown from Figure 3.10 to Figure 3.12. All results are refered to electrical angles.

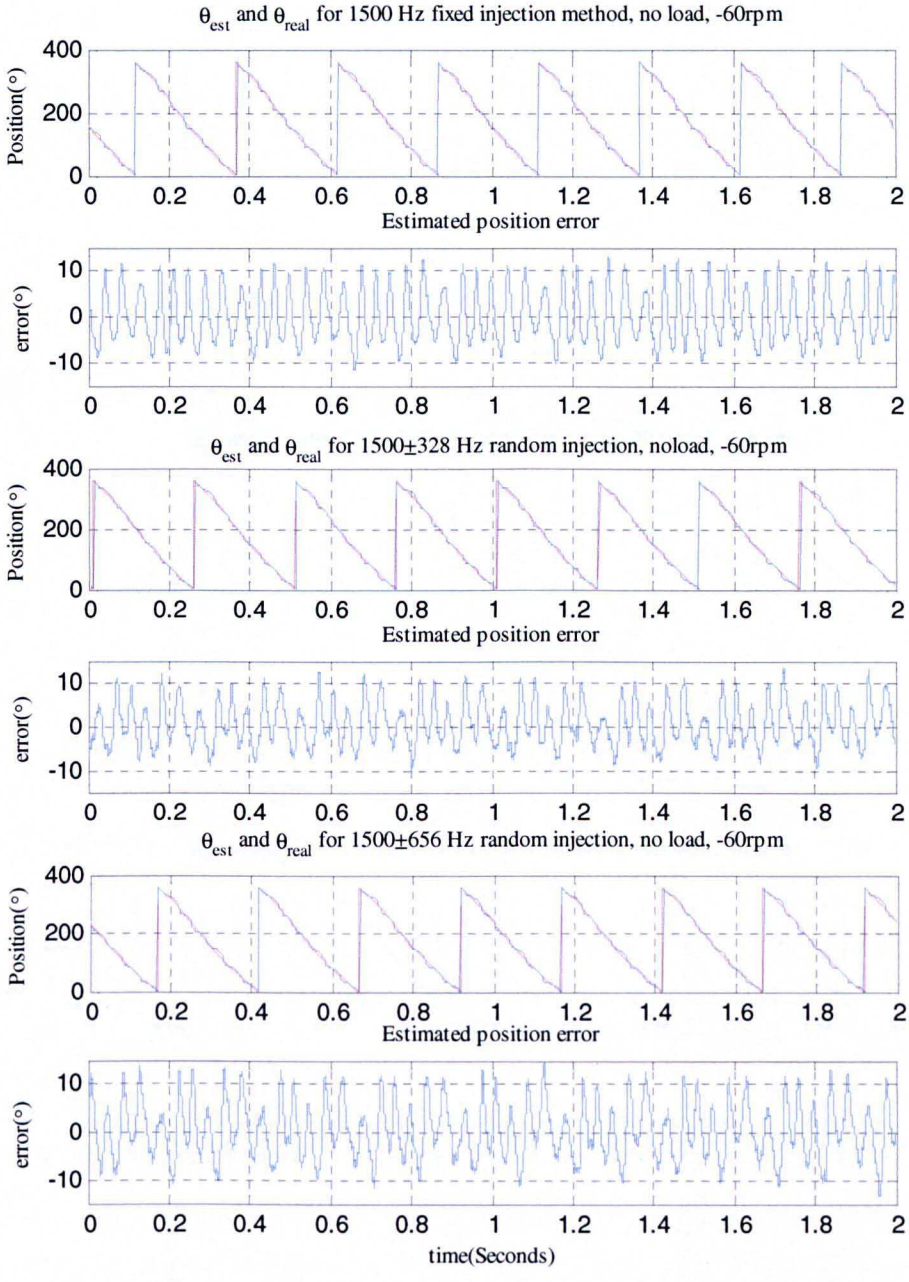

Figure 3.10: Sensorless results for control operations with 1.5 kHz fixed, (1500±328) Hz, and (1500±656) Hz random injections under no load, -60rpm

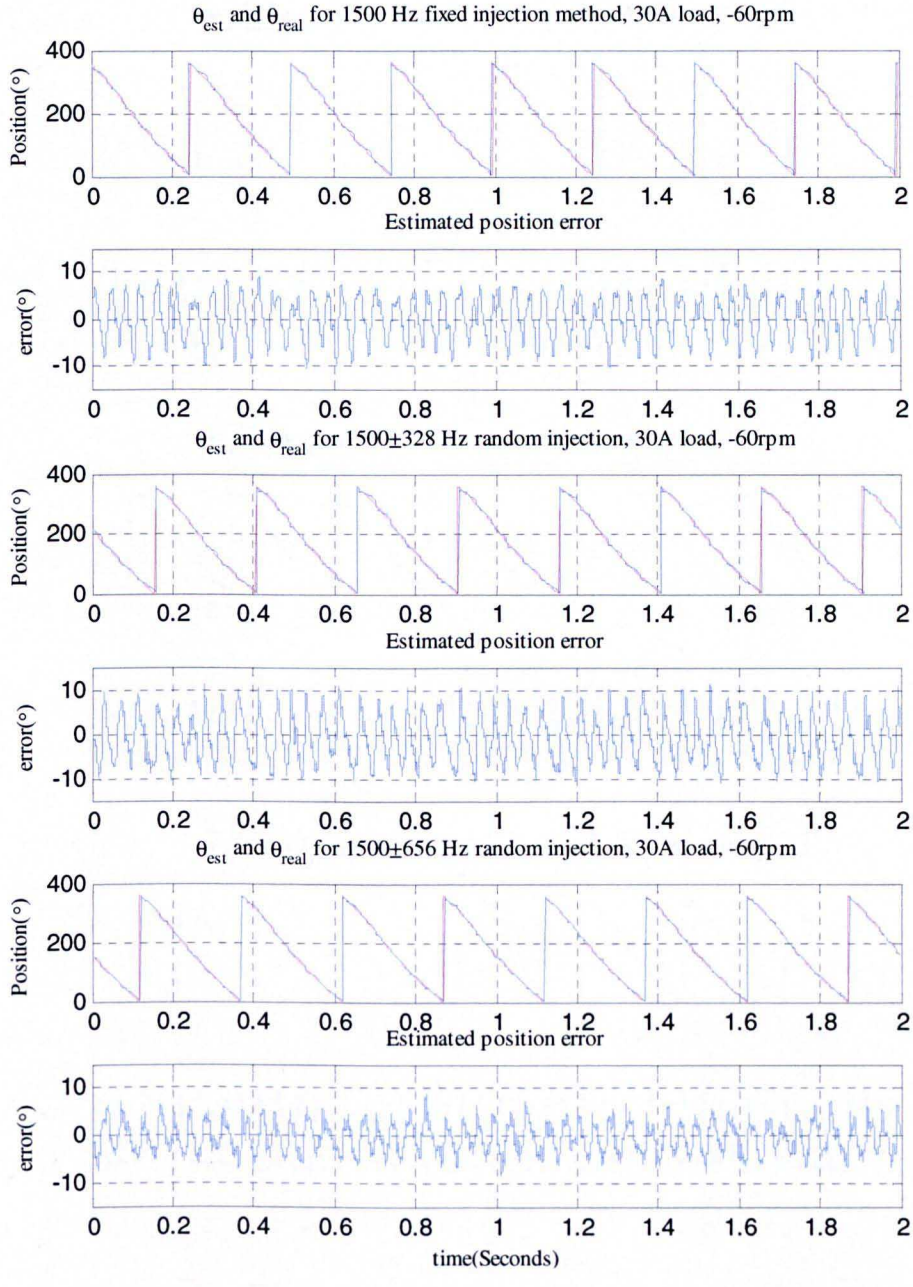

Figure 3.11: Sensorless results for control operations with 1.5 kHz fixed, (1500±328) Hz, and (1500±656) Hz random injections under 30A (33%) load, -60rpm

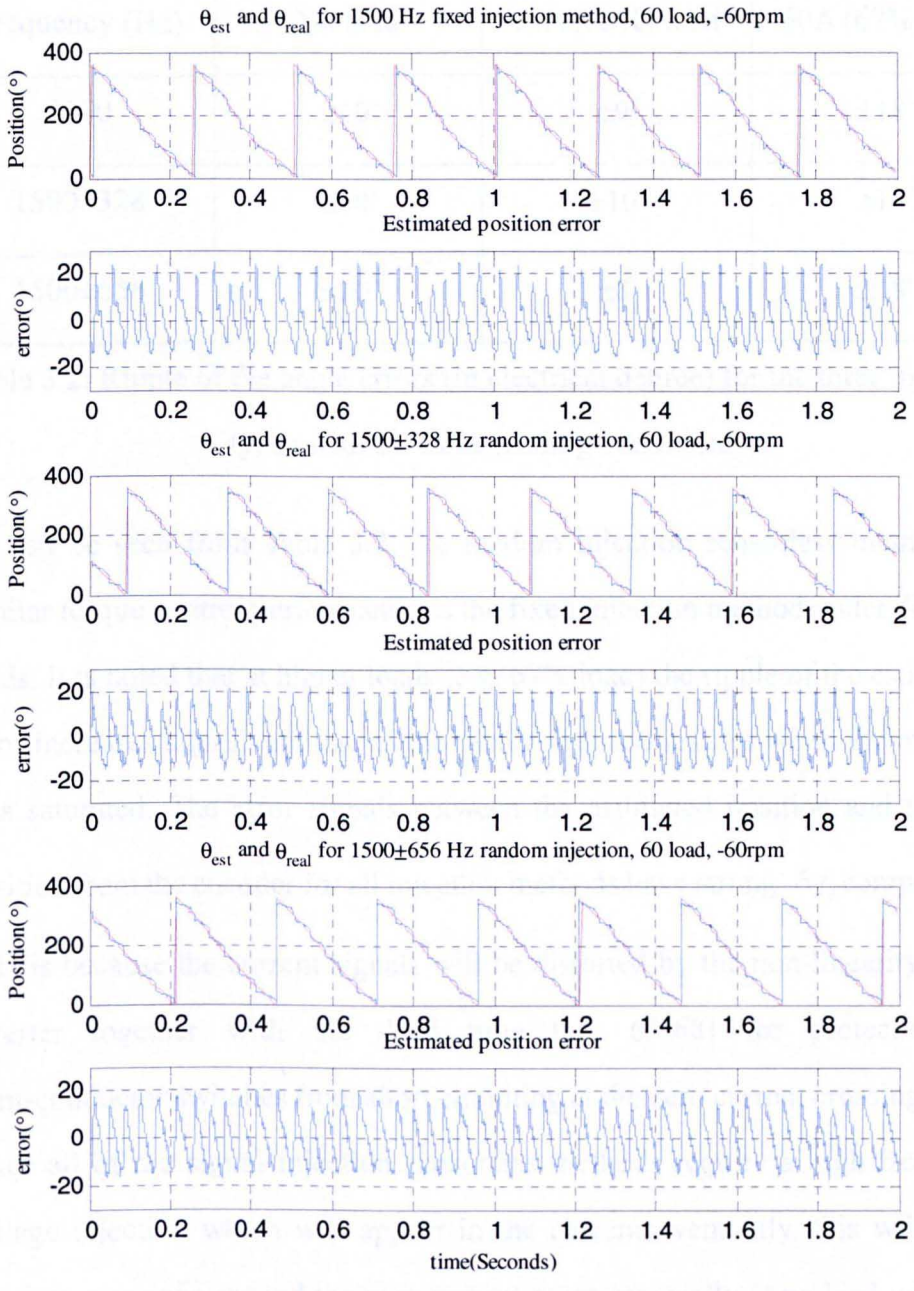

Figure 3.12: Sensorless results for control operations with 1.5 kHz fixed, (1500±328) Hz, and (1500±656) Hz random injections under 60A (67%) load, -60rpm

The angle errors for the the three injection types with the three loading conditions are summarised in Table 3.2.

Frequency (Hz)	No load	30A (33%) load	60A (67%) load
1500	±10°	±9°	±18°
1500±328	±10°	±10°	±18°
1500±656	±10°	±8°	±18°

Table 3.2: Ripple of the angle errors (in electrical degree) for the three injection types with the three loading conditions

As can be seen from Table 3.2, the random injection sensorless method has similar torque control performance as the fixed injection method under different loads. It is noted that at higher loads (e.g. 67% load) the ripple of the estimation error increases significant due to the higher order saliencies when the machine gets saturated. The error signals between the estimated position and the real position from the encoder for all injection methods have strong $6f_e$ components. This is because the current signals will be distorted by the non-linearity of the inverter together with the dead time [11, 65-68] for protecting the semi-conductor switches from short circuiting at the zero current crossing points. Since all of the signal injection sensorless methods require a high frequency voltage injection which will appear in the current eventually, this will cause multiple crossings around the zero current point especially at no load when the line current close around zero. Under loaded conditions, the *hf* currents which contain the position signal information also have considerable multiple zero current crossings [11], so the position estimation will be distorted. The order of the $6f_e$ component relates to the zero current points of the three-phase line current. That is, two zero current points per phase which gives six points in total (i.e. $6f_e$). This distortion in the position estimate will also distort the current signals in return, and in the line current spectrum, it manifests as 5^{th} and 7^{th}

harmonics [68] as it transforms back to the stationary frame. Methods to compensate this distortion have been proposed in [11, 65-68] and the research is ongoing.

3.4.2 Sensorless control results for the fixed *hf* square wave injection method

The square wave injection sensorless method was also tested for the position estimate quality as for the random sinusoidal injection method. The injection signal is a 10 kHz square wave pulsating voltage vector into the estimated *d-axis* with 3V amplitude. The motor was running at -60rpm under sensorless torque control, and the results of the position estimate are shown in Figure 3.13 to Figure 3.15 for no load, 30A (33%) load, and 60A (67%) load, respectively.

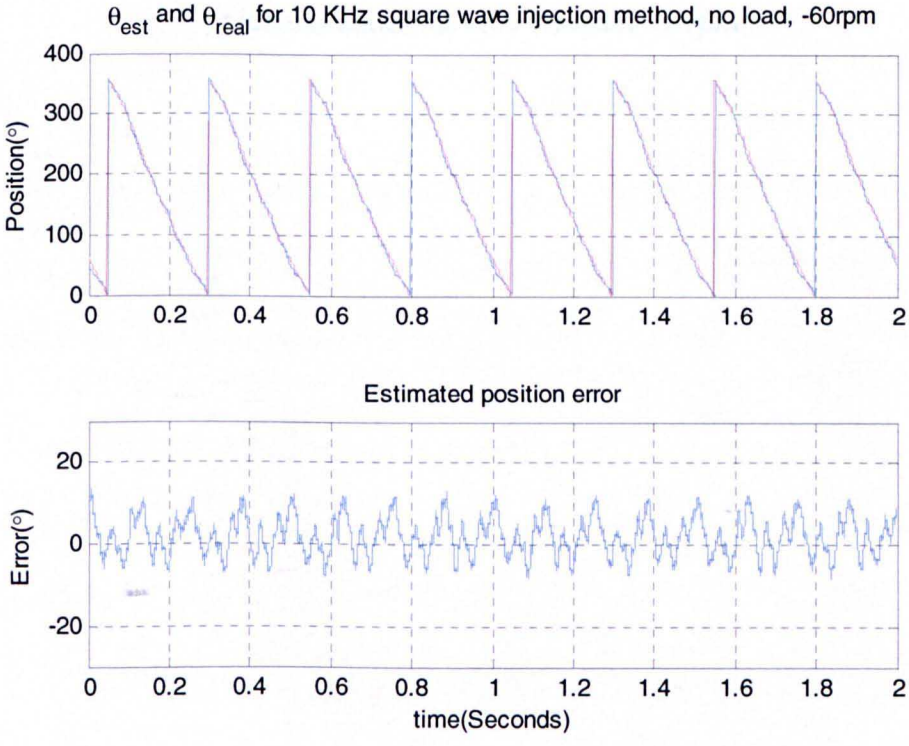

Figure 3.13: Sensorless results for control operations with 10 kHz square wave injection under no load, -60rpm

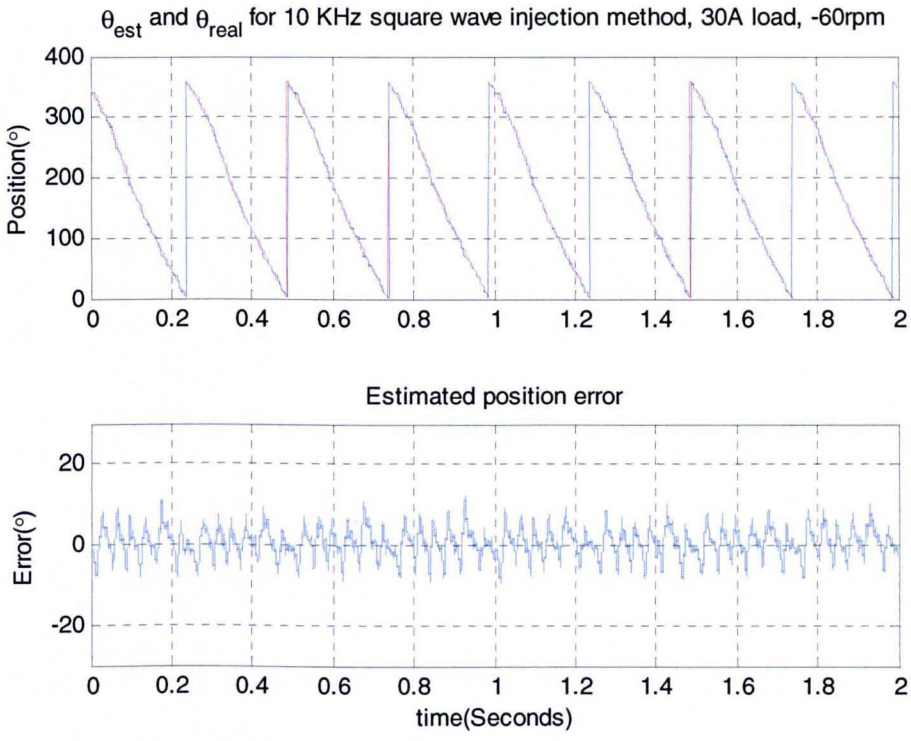

Figure 3.14: Sensorless results for control operations with 10 kHz square wave injection under 30A (33%) load, -60rpm

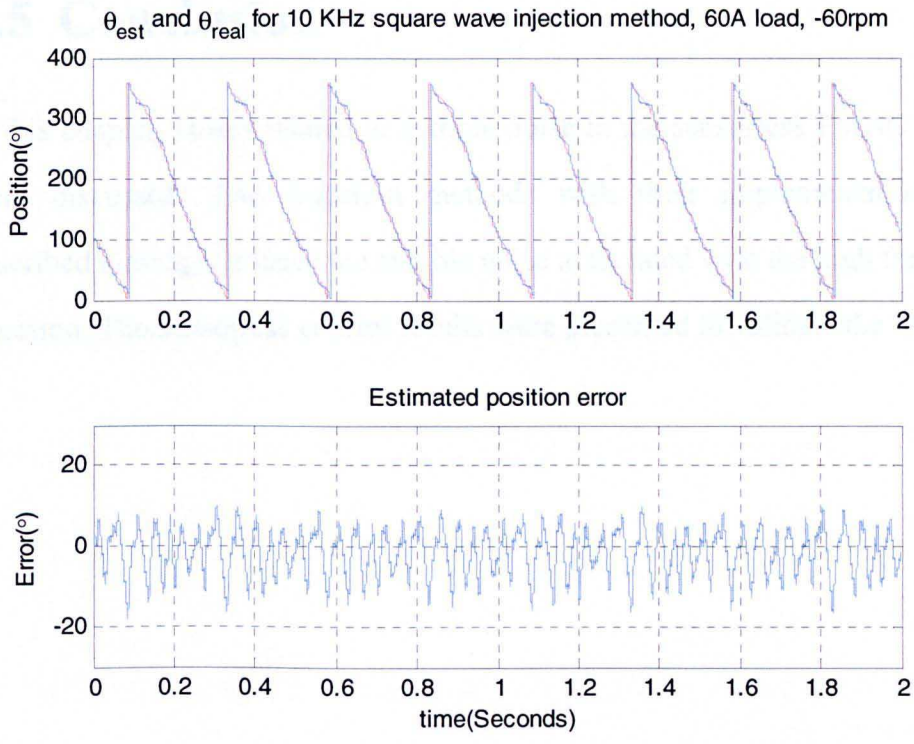

Figure 3.15: Sensorless results for control operations with 10 kHz square wave injection under 60A (67%) load, -60rpm

As can be seen from Figure 3.13 to Figure 3.15, the sensorless control performance for the square wave *hf* injection method has a slightly smaller position error compared to that for the sinusoidal *hf* injection method. This could be possibly because no low pass filters are needed for the demodulation procedure for the square wave injection method, and while for the sinusoidal injection method, the *hf* sinusoidal carrier signal is present in the error signal and needs to be filtered out. However, this is not clear enough and future investigation is needed. The main distortion was again found at $6f_e$.

It was also found for all three methods mentioned in this chapter the ripple of the angle error in the steady state are below 15 electrical degrees with no load and 30A (33%) load, but a bit more than 15 degrees under 60A (67%) load. This needs to be improved in future investigation.

3.5 Conclusion

In this chapter, issues related to audible noise in the sensorless PMAC control were discussed. Two injection methods with their implementation were described aiming to reduce the audible noise associated with the high frequency injection. The sensorless control results were presented to validate the methods.

Chapter 4 Experimental Rig

4.1 Introduction

A bespoke high current inverter and loading system has been designed and constructed to evaluate the control scheames proposed. This test rig is described in detail in this chapter. The overall structure is first outlined to give a brief idea of the construction of the test system. Then the components of this system are discussed individually.

4.2 Overall structure of the test system

The whole test system consists of the AC and DC machines, their driver circuitry, and the measurement, control, capture and display units, as illustrated in Figure 4.1.

The AC machine is a low power low voltage Interior PM synchronous machine with the parameters listed in Table 4.1, and the load machine is a permanent magnet DC machine, the parameters of which can be found in Table 4.2.

The two machines are connected through a $20\,N\cdot m$ coupling. The AC machine is driven by a bespoke three-phase inverter and the DC machine by a single H-Bridge. The two converters share the same DC link, which allows power to

flow bi-directionally between the two machines (i.e. they are able to operate in four quadrants). The external power supply is a regulated DC power supply set at 12V providing the losses of the system.

The measurements include current measurements using three current transducers and position measurement by an encoder mounted at one end of the machine's shaft. The control platform consists of an FPGA, DSP and a host computer developed at the University of Nottingham which performs the data acquisition, control calculation, gating signals output and results display.

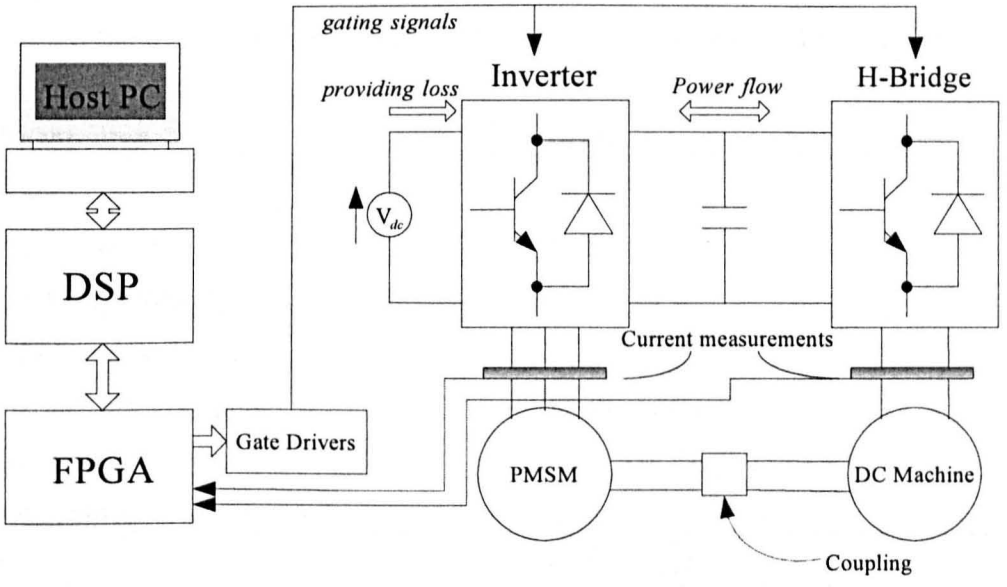

Figure 4.1: The overall system of the test rig

Parameter	Value
Rated Power	1 kW
Rated Speed	2000 rpm
Rated Voltage (ln-ln)	12 V
Rated Current	90 A
Number of poles	8
Back-EMF constant	0.0083 $V/(rad \cdot s)$
Inertia	165× $10^{-6} kg \cdot m^2$
Line-line resistance	43.8 $m\Omega$
Ld	85 μH
Lq	115 μH

Table 4.1: Parameters of the Star-connected PMSM used in the test rig

Parameter	Value
Rated power	250 W
Rated speed	4000 rpm
Peak stall torque	12 $N \cdot m$
Continuous stall torque	1.77 $N \cdot m$
Back-EMF constant	0.049 $V/(rad \cdot s)$
Inertia	282× $10^{-6} kg \cdot m^2$
Resistance	7.3 $m\Omega$
Inductance	0.0456 mH

Table 4.2: Parameters of the DC load machine used in the test rig

4.3 Converters

The test rig utilizes a bespoke three-phase inverter to drive the AC machine and a single-phase H-bridge to drive the DC machine to achieve four-quadrant operation. The structure of this arrangement is shown in Figure 4.2 and a picture of the drives is shown in Figure 4.3.

The semiconductor switches used in this rig are ten IXFN230N10 power MOSFETs with a rated maximum voltage of 100V and a maximum current of 230A to suit the low voltage, high current nature of the machines.

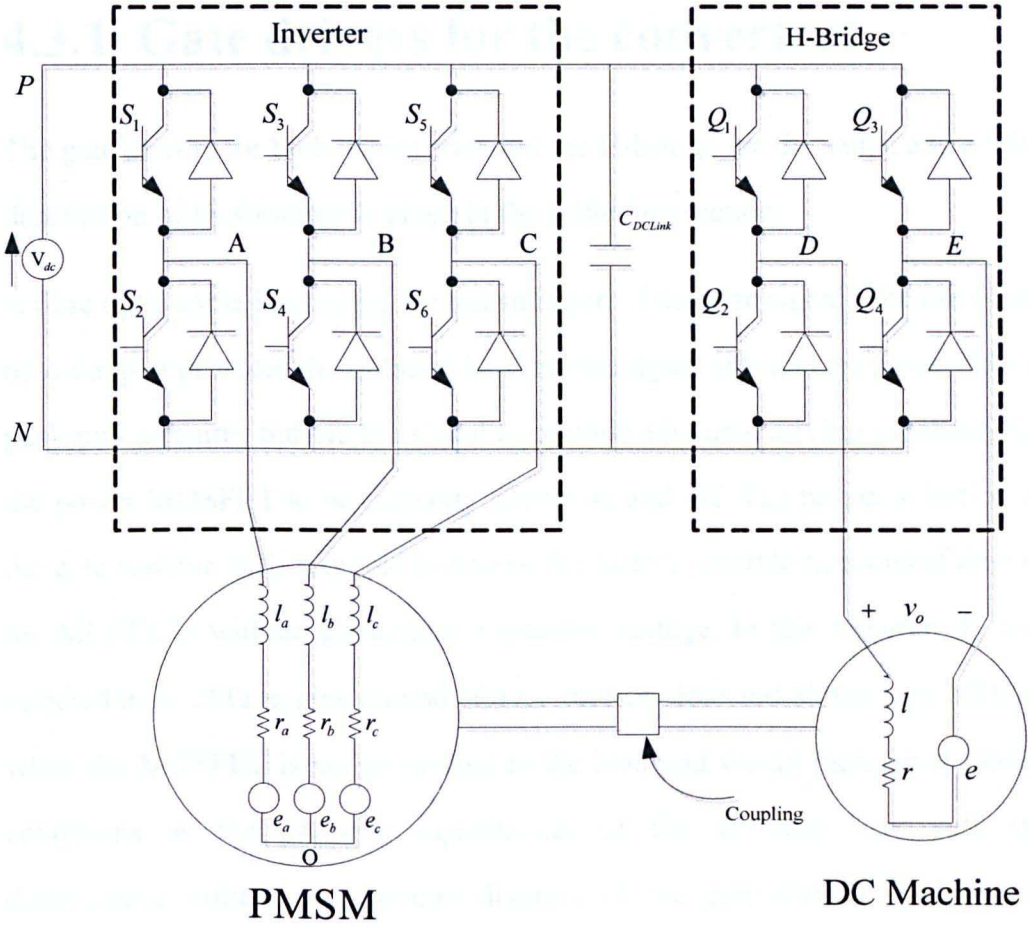

Figure 4.2: Structure of the converters for the test system

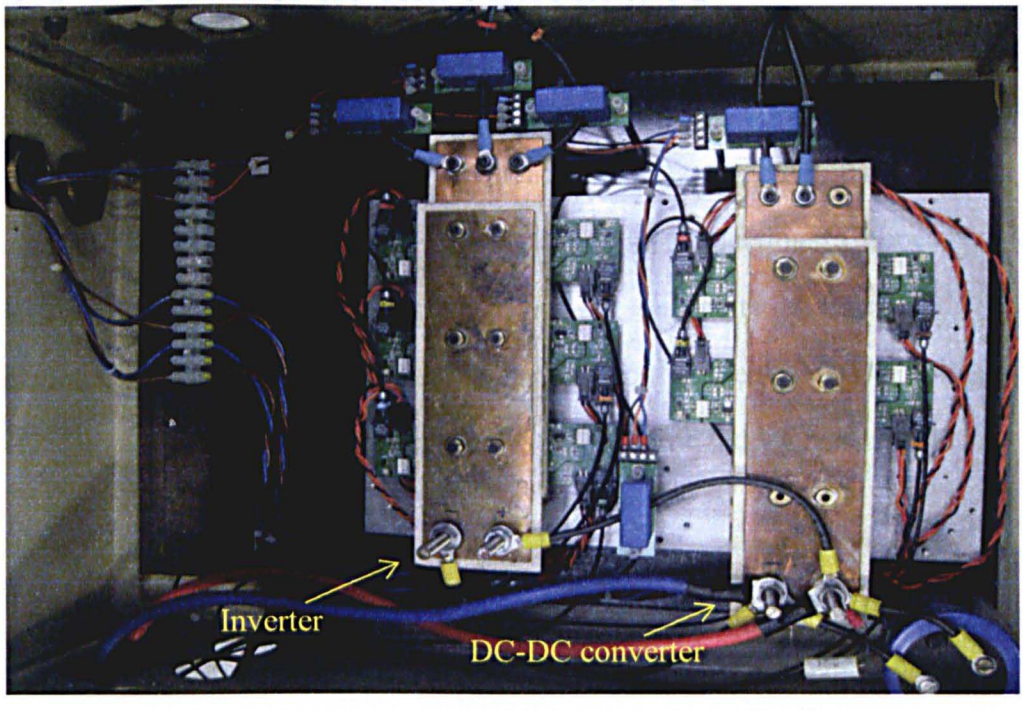

Figure 4.3: Picture of the converters of the test system

4.3.1 Gate drivers for the converters

The gate drivers for both the inverter and the H-bridge are the same, and a brief description of its structure is given in the following section.

A fibre optic cable is used for the transmission of the gate signal. The use of the opto-coupler provides the isolation between the signal side and the power side. A push-pull circuitry buffers the signal to provide adequate driving capability for the power MOSFET to be correctly turned on and off. The proper selection of the gate resistor r_g is required to ensure the fastest possible turn-on/off time of the MOSFETs without generating a massive voltage. In this research, r_g was selected to be 20Ω to give around 800 ns turn-on time and 850 ns turn-off time when the MOSFET is not connected to the load and would increase at loaded conditions as the parasitic capacitances of the switches vary with the drain-source voltage. The circuit diagram of the gate drivers is shown in Appendix B.

4.3.2 Layout of the converters

The layout of the converters is illustrated in Figure 4.3. Due to the high current (up to 90 A) and high switching frequency (20 kHz) natual of the test rig, it is essential to minimise the parasitic inductance in connections. Copper busbars are therefore used as the power plane. The 3-phase inverter and the H-bridge are placed close to each other on a same heatsink so that the shared DC link can be connected with short cables to minimise the parasitic inductance as well.

4.4 Measurement

Measurements are made using three current transducers for motor phase current measurement, and an incremental encoder for sensing the speed and position of

the rotor. The details of these instruments together with their principles will be described in the following sections.

4.4.1 Current measurements

The experimental rig has four current transducers (LEM LA 100-P/SP13) each with a range of ±160 Amps. These are for the three phase currents of the AC machine and the armature current of the DC load machine. The current transducers are current source type devices which output current signals proportional to the current flowing in the primary cables. The benefit of using a current signal transmission is that less noise is picked up than that for a voltage signal transmission, as a voltage signal would be distorted by the environmental noise which normally exists as voltage source. At the receiving side, burden resistors are used to transform the currents to suitable voltage levels for the ADCs (analogue to digital converters). The transducers used in this work were supplied by ±12 V voltage sources with 24 Ω burden resistors, giving a voltage level of ±3.84 V corresponding to ±160A.

4.4.2 Encoder

To evaluate the sensorless operation, a sensored operation benchmark needs to be considered. An incremental encoder (760N/2/HV from the British Encoder Products Co.) with 2500 pulses per revolution (PPR) was used in this rig. The encoder has three signals operating in differential mode, as shown in Figure 4.4.

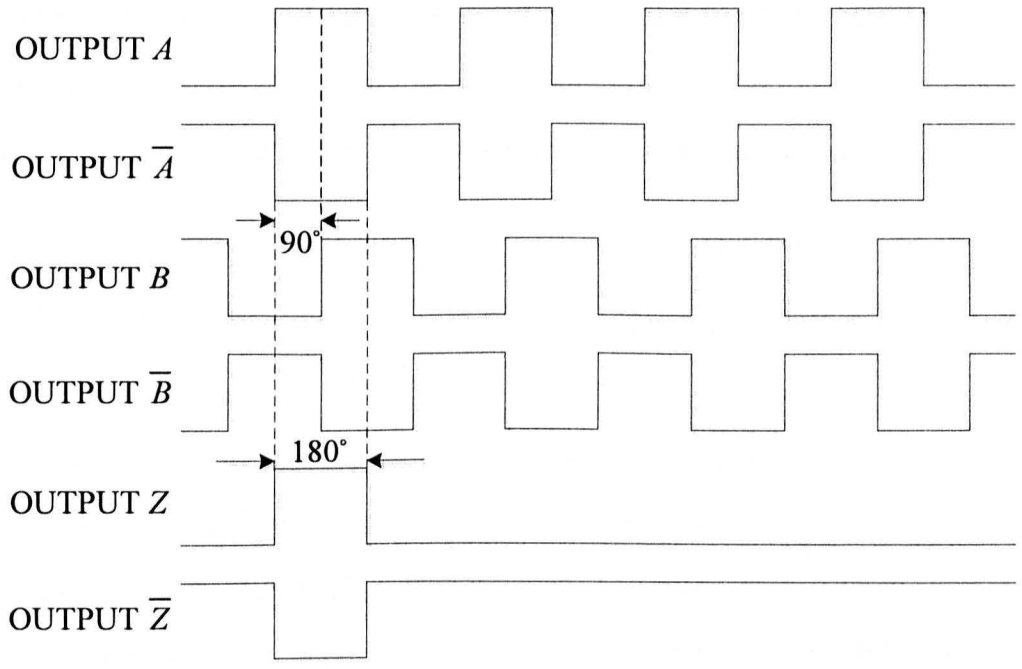

Figure 4.4: Encoder outputs signals, clockwise rotation direction (A leading B)

Two of the signals are shifted 90 degrees electrically apart from each other (the order of the two signals demonstrates the direction of the rotation) and the third is used for resetting a reference point and pulse counting. The signals are received by a differential receiver (Texas SN75175) and the pulses are added or subtracted (depending on whether A is leading B) by a decoding circuit within the FPGA. By knowing the number of the counted pulses and the passed time, the rotated angle can be obtained and thus the absolute position can be calculated with respect to the reference point. The speed of the rotation can be obtained by calculating the change in position every 2.5ms (every 50 interrupts to calculate it since the mechanical time constant is much greater than that of the interrupt period) shown as:

$$\omega_r = {}^{\Delta\theta}\!/_{2.5ms} = \Delta\theta \cdot 400 \ (rad/s) \tag{4-1}$$

where $\Delta\theta$ is the change in position (rad/s) within $2.5ms$.

As the pulse value is an incremental one with respect to the reference point, once

the encoder is powered off the zero reference point would be lost. Hence, the motor needs to rotate at least one revolution to reset the zero reference point to achieve the correct absolute angle at the start of controlled operation.

For a vector controlled PMSM motor, the offset angle between the encoder reference point and the permanent magnet direction needs to be known and compensated for correct alignment.

The easiest way to obtain this offset is to inject a constant voltage vector to the stator winding to force the rotor magnet to align with the stator magnetic field. The recorded absolute angle is then the required offset. This can be illustrated in Figure 4.5, where the applied vector has only an α component. It is noted that all angles referred are in electrical degrees.

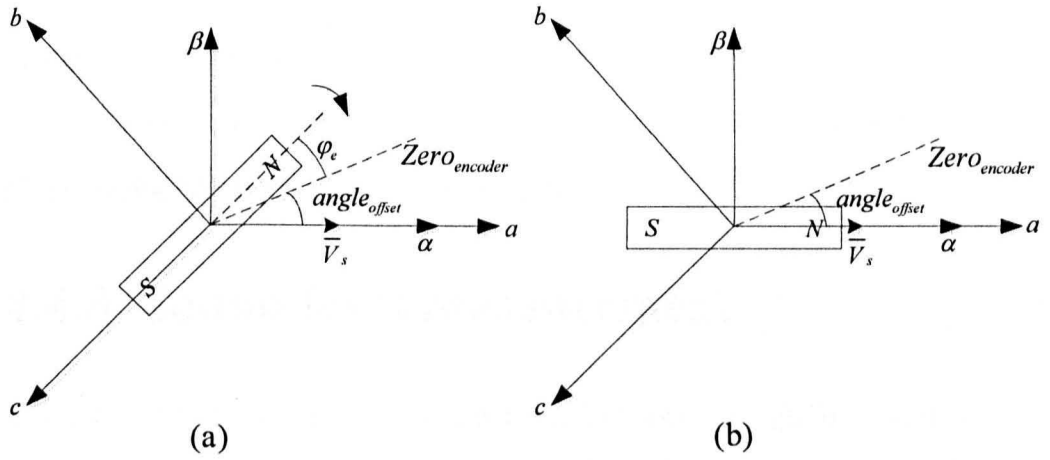

Figure 4.5: Encoder offset obtained by applying a fixed voltage vector to force the alignment between rotor magnet and stator flux. From left to right: rotor initially stalled at a random electrical angle, quoted as φ_e; (b), rotor aligned with the stator flux.

Another method utilizes the back-EMF of the machine. This method will give a more accurate reading of the encoder offset angle, and the principle is shown in Figure 4.6.

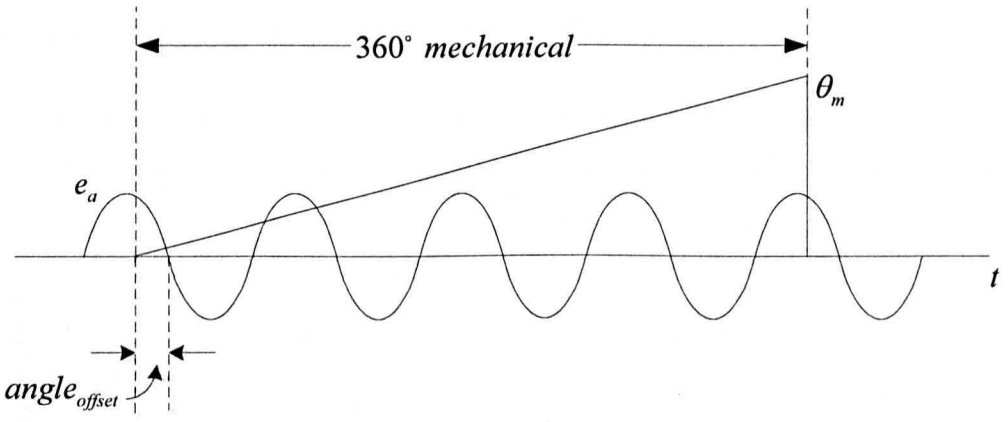

Figure 4.6: Encoder offset obtained by looking at the phase back-EMF

The AC motor was driven by the DC load machine rotating at a constant speed in the positive direction. The terminals of the stator windings were open and the phase voltages were measured, which equals the back-EMF of each phase. Since the motor used in the experiment has 8 poles, one mechanical revolution contains 4 electrical revolutions as seen from Figure 4.6. The angle between the zero crossing point of the encoder position and the zero crossing point of the A phase back-EMF is the encoder offset angle.

4.4.3 Sound level measurement

4.4.3.1 Introduction to human hearing and weighting scales

The audible range of the human hearing is from 20 Hz up to around 16 kHz and the upper limit decreases with age [69]. Within this range, however, the human ear responds in a non-linear way to different frequencies of noise, and is most sensitive to the frequencies between 2 and 5 kHz, mainly due to the structure of the human ear [69]. To match the perceived 'loudness' of noise for human hearing, different weighting scales are used for sound pressure level measurements, including A, B, C, D, and Z weightings [70, 71], etc. By using these weighting scales, the measured sound levels in different frequency pitches are either deemphasized or emphasized. The most commonly used weighting

scale is the A-weighting scale, as shown in Figure 4.7.

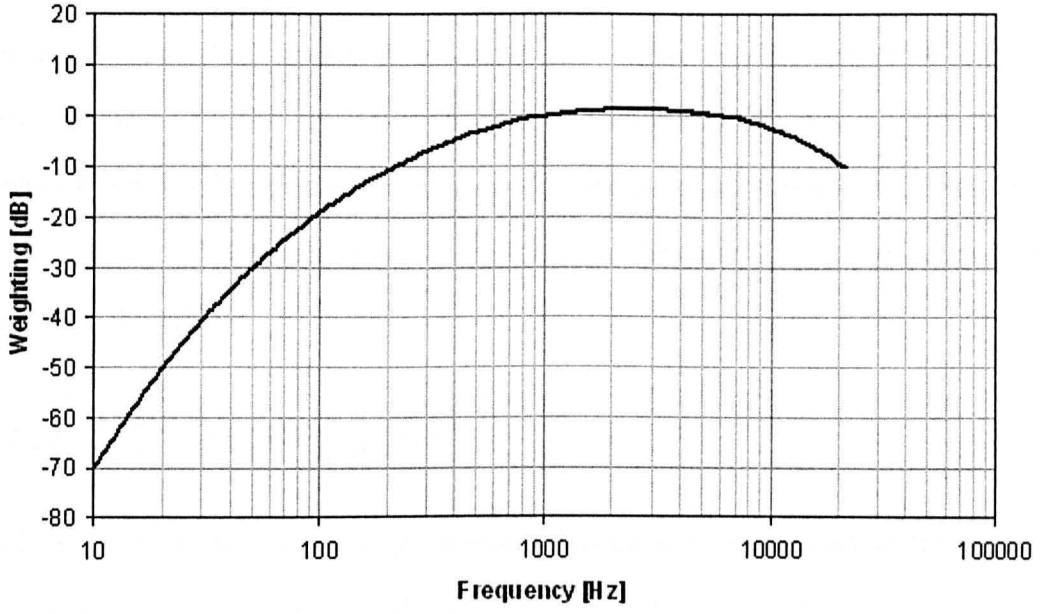

Figure 4.7: A-weighting scales [72]

It is designed based on the 'equal loudness contours' defined in [71]. The sound level measurement after scaling by A-weighting is referred to as dBA. It is regarded to fit well in environmental noise measurement [69] for all frequency ranges, whereas B, C, and D-weightings are more specified to measure the noise in certain range of frequencies.

However, there are some drawbacks for these weighting scales. Firstly, since they are designated to describe a broad band sound with a single index, multiple tones of different frequencies may give the same values. Therefore, the spectrum analysis would be an more accurate way to describe the broad band noise [69] with multiple tones such as the random noise introduced by the random *hf* injection sensorless method. In addition, since these weightings are based on mathematic formulas weighting only the loudness, other factors such as the duration of the sound, the psychology effects on humans etc. are not taken into account. Other methods combining all the effects on human hearing are desirable.

4.4.3.2 The sound level measurement

The audible noise generated for the different injection methods was measured using a Testo-816 sound level meter [73] with A-weighting [69-71, 74] processing as mentioned ealier. The PMAC motor and DC load machine were placed in a wooden box lined with sound proof material. A rubber mat was also placed under the motor base to absorb the vibrations and noise conducted through the table.

4.5 FPGA and DSP

The control platform used in this research is a general purpose advanced digital system, developed in the PEMC group of the University of Nottingham [75]. The core components of this platform are a field programmable gate array (FPGA) chip and a 32-bit floating point digital signal processor (DSP). They are used to process all the measurement data, generate gating signals and perform motor control.

The FPGA is used to manage the I/O interface. Measured values of the motor's currents and position are stored into the registers of the FPGA and read by the DSP through the interface. The DSP performs the control calculations and eventually generates the timing signals for PWM generation, which are then passed to the FPGA to generate the gating patterns for the converters to perform the speed and torque control of the motor. For a sensorless control application, the DSP also performs the calculation of the position estimation.

4.5.1 FPGA board

A ProASIC3-A3P400 type of FPGA chip, a third generation of Actel Flash FPGA, is chosen in this research due to its good performance/price ratio. It has 400K system gates, 9216 D-flip-flops, 54Kbits RAM and up to 194 user I/Os.

Besides the FPGA chip, the FPGA board also integrates the A/D channels, D/A converter, LED trip display, and user inputs and outputs, etc., which is illustrated in Figure 4.8.

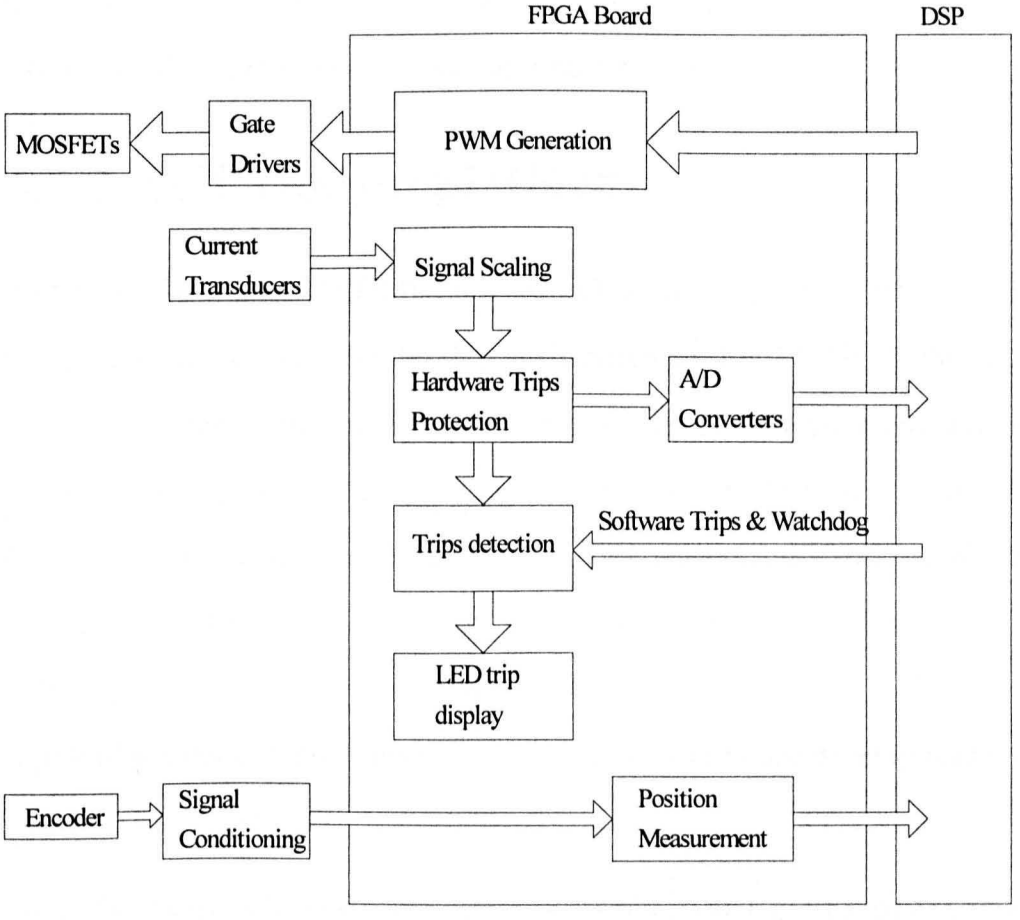

Figure 4.8: The function block of the FPGA board

Ten A/D channels are available on the board. In this experiment, only four channels are used for sampling the three phase currents of the AC motor and the armature current of the DC load machine. The A/D circuit measures the voltage ranging from +5 to −5 V. Then this is converted to 0-2.5V for the A/D input pins. Hardware trips are available by comparing the input voltage with a pre-defined reference voltage, providing fast protection against over current, over voltage, etc.

Eight channels of outputs compatible with the fibre optic connectors are available on the boards for outputting the PWM gating signals. However, ten

outputs are needed (6 for the 3-phase inverter and 4 for H-bridge). Therefore, an extension board for more outputs is placed upon the FPGA board, which also integrates the signal conditioning circuits for the encoder signal. The extension board is connected to the main board via a 26-pin header connected to a 74LVC16245A buffer and a 74LVC245A buffer chip.

4.5.2 DSP control platform

A C6713 DSP Starter Kit (DSK) is a standalone development platform which allows users to evaluate and develop applications for the TI C6xx DSP family [76], and is used in this rig. It is supplied by a single +5V power supply and consists of a TMS320C6713 DSP chip which operates at 225 MHz, a 32-bit wide External Memory Interface (EMIF) which connects on-board peripherals including the SDRAM, Flash and Complex Programmable Logic Device (CPLD), an on-board analogue audio codec, and an embedded JTAG emulator which allows debug from Code Composer Studio (a TI's code development tool) through a PC's USB port.

The DSK also provides three expansion connectors which can be used to accept plug-in daughter cards. They are for memory, peripherals, and the Host Port Interface (HPI).

The memory and peripherals connectors are connected with the FPGA board, providing interfacing the memories on the FPGA board with the DSP's asynchronous EMIF signals, and bringing out the DSP's peripheral signals such as the external interrupt trigger signal from the FPGA's clock.

4.5.3 HPI and PC host

A TMS320C6713 DSK HPI Daughter card by Educational DSP [77] is connected to the DSK. In the host service mode, the daughter card allows serial,

parallel and USB access to the DSK's HPI port. In this research, a USB type of access is used to interface the PC host and the DSK. A Matlab based user interface developed by the PEMC group of the University of Nottingham is used to download a programme built in Code Composer to the DSP, control the operation of the application and monitor variables on a PC screen.

4.6 The design of the controller

The PMSM is operated under current control and the DC load machine is under speed control. Both of the controllers are first designed in a continuous time domain (s-plane) and then digitized into C-code in a DSP.

4.6.1 Current controller design

The vector control theory models AC machine as a DC machine, so the PMSM can be modelled by the voltage equations including the impedances and the cross-coupling terms in the rotating *d-q* frame, as shown in (4-2).

$$\begin{bmatrix} v_d \\ v_q \end{bmatrix} = \begin{bmatrix} r_s + pL_d & -\omega_r L_q \\ \omega_r L_d & r_s + pL_q \end{bmatrix} \begin{bmatrix} i_d \\ i_q \end{bmatrix} + \begin{bmatrix} 0 \\ \omega_r \psi_m \end{bmatrix} \tag{4-2}$$

where v_d and v_q are the d and q parts of the stator voltage, L_d and L_q are the d and q parts of the stator inductance, i_d and i_q are the d and q parts of the stator current, r_s is the stator resistance, p is the differentiator, ω_r is the electrical speed of the rotor, and ψ_m is the rotor permanent magnet flux.

The equivalent circuit of the PMSM is shown as in Figure 4.9.

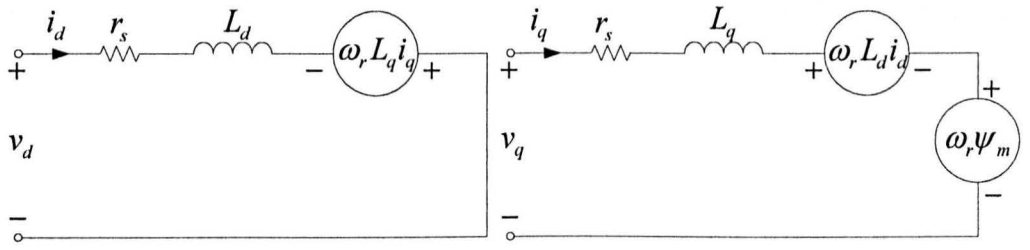

(*a*) *d - axis* model (*a*) *q - axis* model

Figure 4.9: Equivalent circuit of a PMSM in the *d-q* rotating frame

Since the time constant of the mechanical system is far slower than that of the electrical system, the speed can be regarded as constant in the current transition time. Therefore, the cross-coupling terms and the back-EMF term can be neglected for the feedback control design of the current controller. The plant used for current loop design is assumed as:

$$G_{plant}(s) = \frac{1}{sL_s + r_s} \tag{4-3}$$

where r_s is the stator phase resistance and L_s represents the average value of the *dq* inductances which was used in this design.

In this work, a PI regulator was chosen and the control schematic is given in Figure 4.10.

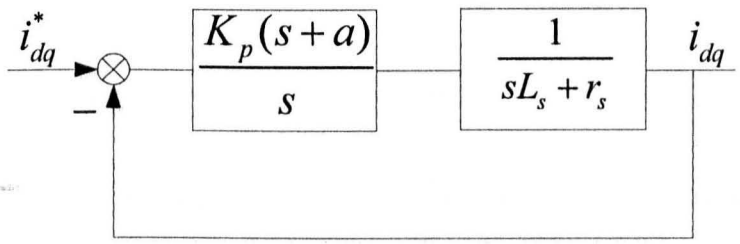

Figure 4.10: Design schematic of the current loop

No delay terms are considered as the sampling delay (50 μs) is much smaller than the plant time constant.

The current controller bandwidth was set to 150 Hz to match the previous work in [13] and using the classic root locus method the controller was designed as:

$$G_c(s) = \frac{0.10876(s+539.9)}{s} \tag{4-4}$$

The Bi-linear transform, as given in (4-5) was used to digitize the controller for a DSP.

$$s = \frac{2}{T_s} \cdot \frac{1-z^{-1}}{1+z^{-1}} \tag{4-5}$$

where T_s is the sampling frequency which in this case is 50 μs.

An anti-windup procedure was automatically incorporated in the code since the output of the controller was limited to prevent excessive error being accumulated when the calculated results exceeded the inverter output capability.

To enhance the dynamic performance of the current controller, feed forward terms were added after the controller output. Thus the ultimate control block of the current controller is shown as in Figure 4.11.

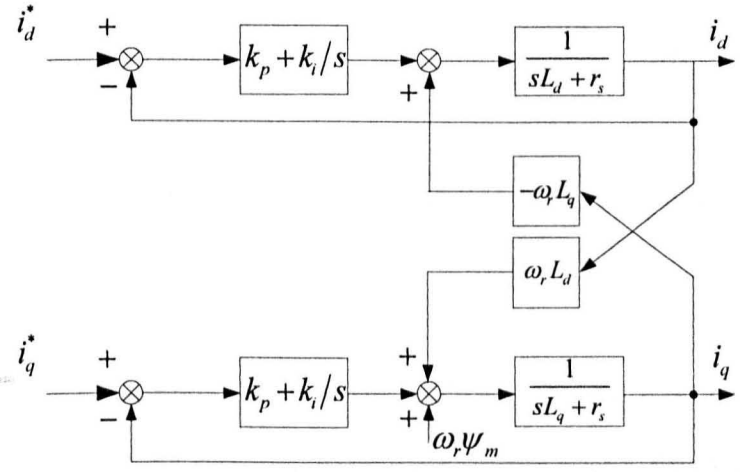

Figure 4.11: Feedback current control with feed forward decoupling

The performance of the current controller is tested for *d* and *q* current by giving a pair of opposite step demands to one of the currents and keeping the other zero,

as shown in Figure 4.12 and Figure 4.13, respectively.

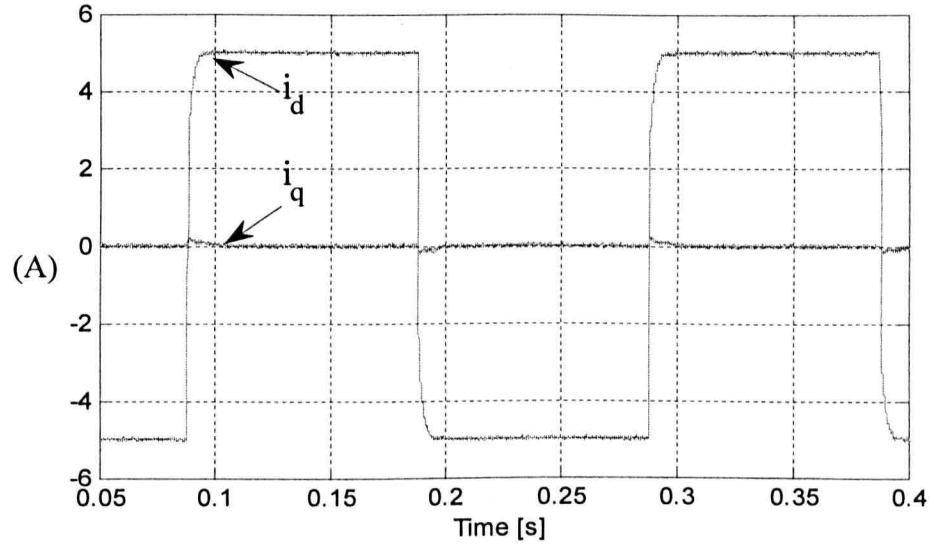

(a)

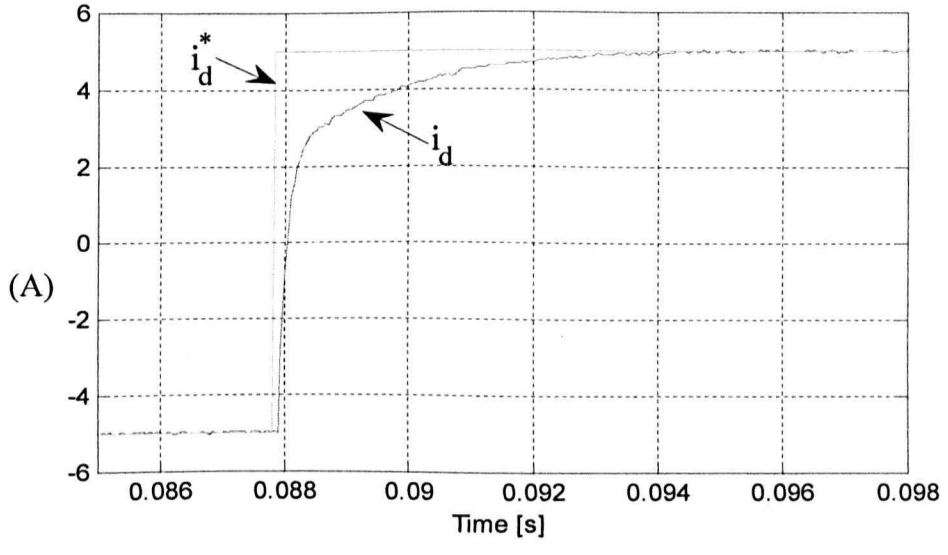

(b)

Figure 4.12: The performance of the current controller for a square wave type demand of *d-axis* current while keeping *q-axis* demand zero. From top to bottom: (a), measured i_d and i_q currents in 0.4 second; (b), demanded and measured i_d.

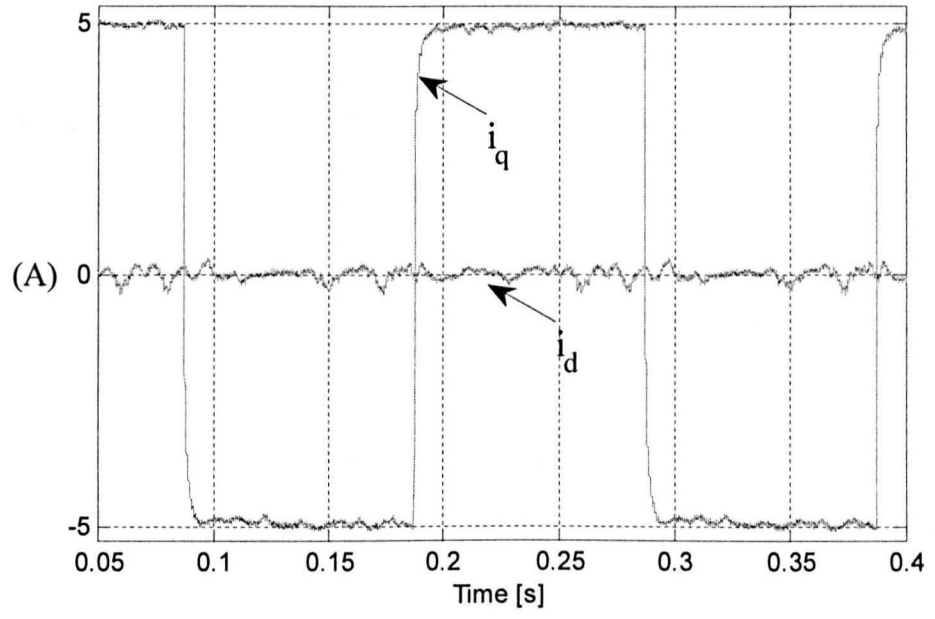

(a)

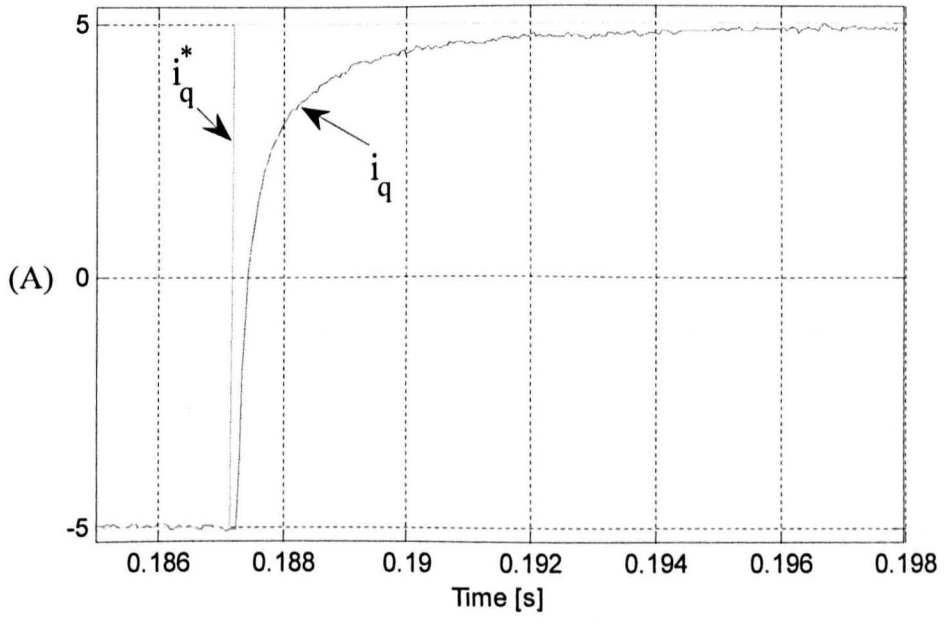

(b)

Figure 4.13: The performance of the current controller for a square wave type demand of *q-axis* current while keeping *d-axis* demand zero. From top to bottom: (a), measured i_d and i_q currents in 0.4 second; (b), demanded and measured i_q.

As observed from Figure 4.12 and Figure 4.13, the rise time of the current

controller was about 3 *ms*, as expected for the designed controller bandwidth. However, the *d-axis* current response in Figure 4.12 shows a much faster initial rising edge at the beginning of the transient followed by a slower transient in the following period. This is because the closed loop zero of the controller probably falls on the right hand side of the plant pole for the *d-axis* current loop (since average inductance is used instead of actual *d-axis* inductance for this design). This can be seen by comparing the two resultant root locus plots in Figure 4.14 for the *d* and *q* axis controllers. For the *d-axis* controller, the pole A corresponds to the faster rising part of the curve at the beginning and pole B corresponds to the slower part of the curve.

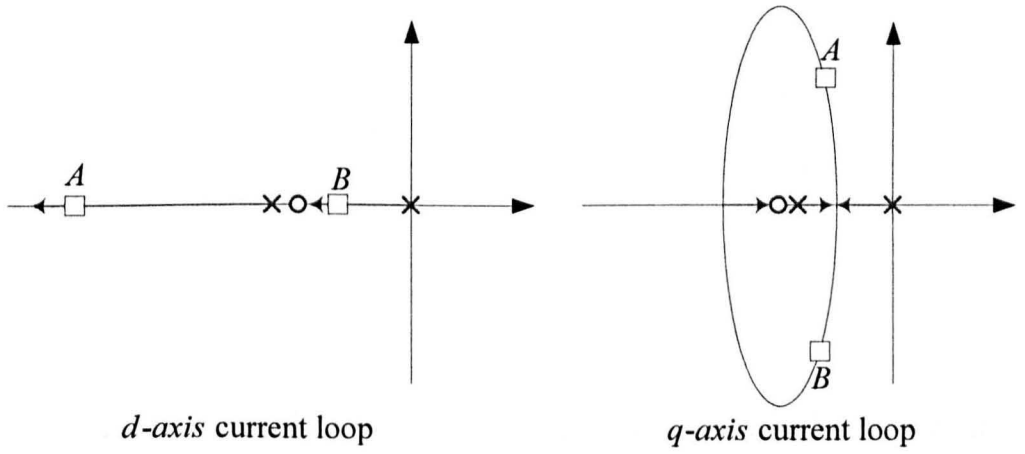

Figure 4.14: Root locus to illustrate the *d* and *q* axis current loop controller

The current loop of the DC load machine was designed as a 150 Hz PI controller in a similar mannor to the PMAC machine. The DC machine has only one current loop and the armature current was dirrectly measured and used as the feedback to the controller.

4.6.2 Speed controller design

The DC load machine was controlled under speed control. The plant of the mechanical model is given as:

$$G_{splant}(s) = \frac{k_t}{Js + B} \tag{4-6}$$

where k_t is the torque constant, J is the inertia of the motor and B is the friction of the system which can be ignored since it's very small.

A PI controller was also adopted and the schematic is given as in Figure 4.15, assuming the current loop as a unity constant with respective to the speed loop.

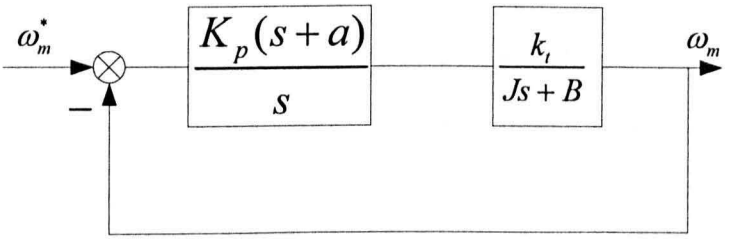

Figure 4.15: Controller schematic of the DC machine speed loop

In this work, a controller with a bandwidth of 8.488 Hz was used for the speed loop, as shown in (4-7).

$$G_{sc}(s) = \frac{0.2611(s + 757.95)}{s} \tag{4-7}$$

Similar approach was used to transform it into discrete domain as that for current loop with a sample time of 2.5ms. The performance of the controller was tested when speed reversal demands were applied, as shown in Figure 4.16.

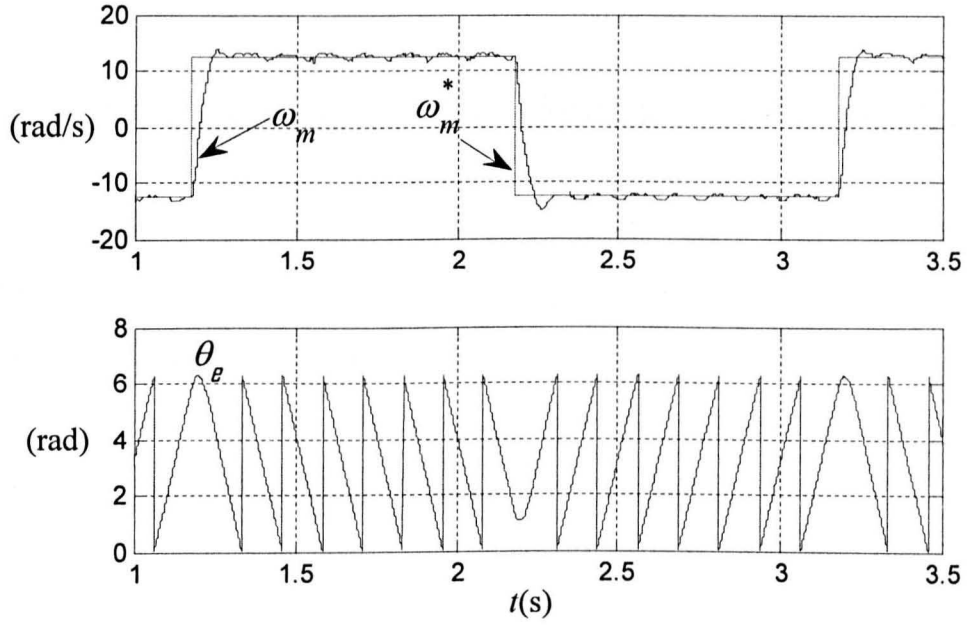

(a)

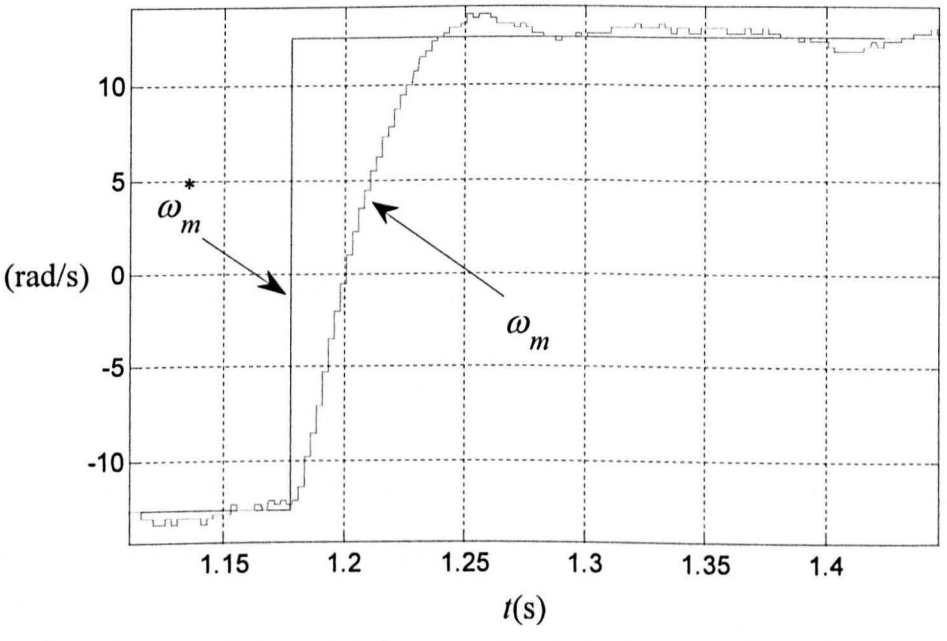

(b)

Figure 4.16: The performance of the speed controller for speed reversal. From top to bottom: (a), demanded and measured speed of the rotor, with its electrical position from the encoder; (b), demanded and measured speed (zoomed in).

It was found that the rise time of the speed response was around $50\,ms$, as

expected.

4.7 The design of the Mechanical observer

A mechanical observer [19] was adopted to process the position estimation for the sensorless operation. The structure of a typical mechanical position and speed observer is shown as in Figure 4.17. It is noted that the position estimate was used as the feedback for the frame transformation for deriving the error signal and the friction was neglected.

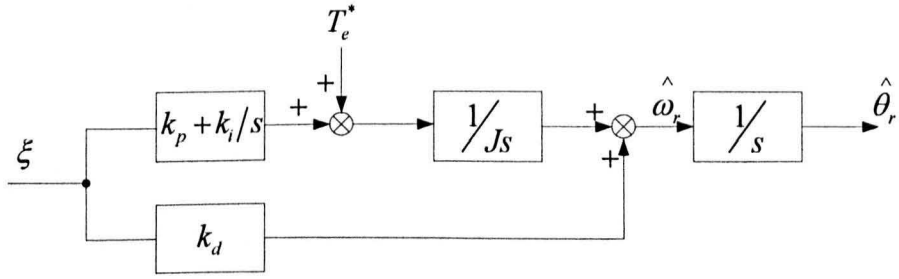

Figure 4.17: Structure of the Mechanical Observer used to obtain the position estimate [19]

The transfer function of the plant is given in (4-8).

$$G_{MO\_plant}(s) = \frac{1}{Js^2} \tag{4-8}$$

where J is the overall inertia of the system, and is defined by summing the two inertia values in Table 4.1 and Table 4.2.

A PID controller was adopted. Again the root locus method was used to design the controller. The resulting controller is given as:

$$G_{MO\_contorller}(s) = \frac{k_d(s^2 + \frac{k_p}{k_d}s + \frac{k_i}{k_d})}{s} = \frac{0.11738(s^2 + 195.3s + 2704.5)}{s} \tag{4-9}$$

The continuous domain controller was decomposed into a PI controller and a gain equal to k_d as shown in Figure 4.17. They were digitized respectively

using the bilinear transformation.

It is noted that although a higher bandwidth is expected to obtain better dynamic performance, a trade-off has to be made to maintain good estimation quality. A bandwidth of 90 Hz was therefore incorporated.

4.8 Space vector modulation

Space vector modulation (SVM) scheme is a widely adopted real-time modulation technique which is preferred in a digital implementation of a voltage source inverter (VSI) for generating the PWM timing signals[78], and is used in this research.

For a 3-phase VSI in Figure 4.2, the operating status of the power devices can be represented by switching states. State '1' represents the upper switch of the inverter leg is on and the (v_{AN}, v_{BN} and v_{CN}) is positive ($+V_{dc}$), while state '0' represents the lower switch of the inverter is on and the terminal voltage of the inverter is zero. Eight possible switching states combinations can be found, including six active states and two zero states, which are defined as active space vectors and zero space vectors, respectively. The six active vectors divide the space into six sectors, each covering 60° of the space region. The space vectors and their corresponding conducting switches as well as the vector values are listed in Table 4.3 [78], and the division of the sectors is illustrated in Figure 4.18.

Space Vector	Switching State	On-state Switches	Vector Value
$V0$	000	S_2, S_4, S_6	0
$V1$	100	S_1, S_4, S_6	$\frac{2}{3}V_{dc}e^{j0}$
$V2$	110	S_1, S_3, S_6	$\frac{2}{3}V_{dc}e^{j\frac{\pi}{3}}$
$V3$	010	S_2, S_3, S_6	$\frac{2}{3}V_{dc}e^{j\frac{2\pi}{3}}$
$V4$	011	S_2, S_3, S_5	$\frac{2}{3}V_{dc}e^{j\pi}$
$V5$	001	S_2, S_4, S_5	$\frac{2}{3}V_{dc}e^{j\frac{4\pi}{3}}$
$V6$	101	S_1, S_4, S_5	$\frac{2}{3}V_{dc}e^{j\frac{5\pi}{3}}$
$V7$	111	S_1, S_3, S_5	0

Table 4.3: Space vectors and their on-state switches

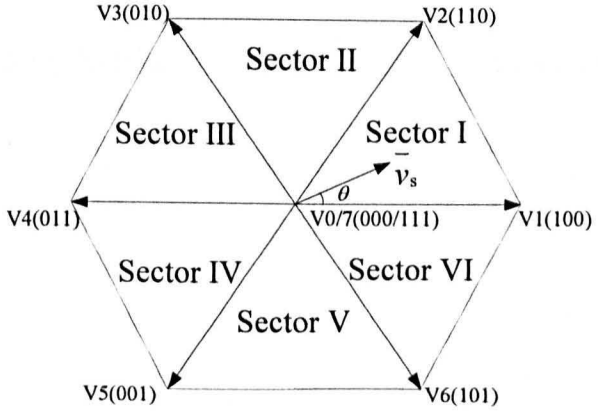

Figure 4.18: Division of the sectors by active space vectors

The values of the active vectors are obtained based on the 3-phase/2-phase transformation (Park transformation [22]). For the two-level inverter in Figure 4.2, after applying the Park Transformation, phase voltages can be represented by two orthogonal values in the stationary α-β plane as:

$$\begin{bmatrix} v_\alpha \\ v_\beta \end{bmatrix} = \frac{2}{3}\begin{bmatrix} 1 & -\frac{1}{2} & -\frac{1}{2} \\ 0 & \frac{\sqrt{3}}{2} & -\frac{\sqrt{3}}{2} \end{bmatrix}\begin{bmatrix} v_{AO} \\ v_{BO} \\ v_{CO} \end{bmatrix} \tag{4-10}$$

where v_α, v_β are the orthogonal components of the vector, and v_{AO}, v_{BO} and v_{CO} are the instantaneous load phase voltages. The coefficient $2/3$ is an arbitrarily defined constant, and the benefit of using this is that the magnitude of the three-phase voltages is reserved after the transformation. A space vector $\underline{v}_s$ can be constructed as:

$$\underline{v}_s = v_\alpha + jv_\beta \tag{4-11}$$

Applying (4-10) into (4-11), the space vector can be rewritten in the form of phase voltages as:

$$\underline{v}_s = \frac{2}{3}(v_{AO}\cdot e^{j0} + v_{BO}\cdot e^{j\frac{2\pi}{3}} + v_{CO}\cdot e^{j\frac{4\pi}{3}}) \tag{4-12}$$

where $e^{j\theta} = \cos\theta + j\sin\theta$ and $\theta = 0,\ \frac{2\pi}{3}$ and $\frac{4\pi}{3}$, respectively.

If the operation of the inverter is balanced (i.e. no zero sequence component), equation (4-13) can be obtained:

$$v_{AO} + v_{BO} + v_{CO} = 0 \tag{4-13}$$

When the active vector $V1$ is applied to the two-level inverter, the values of the phase voltages are obtained:

$$v_{AO} = V_{dc},\quad v_{BO} = v_{CO} = -V_{dc}/2 \tag{4-14}$$

Applying (4-14) into (4-12), the value of space vector is obtained:

$$\underline{V}_1 = \frac{2}{3} V_{dc} e^{j0} \tag{4-15}$$

In a similar way, the other five active vectors can be derived and the common expression of all the active vectors can be written as:

$$\underline{V}_k = \frac{2}{3} V_{dc} e^{j(k-1)\frac{\pi}{3}}, \qquad k = 1,2,...,6 \tag{4-16}$$

A space vector $\underline{v}_s$ can be therefore represented by the sum of the nearby two active vectors and a zero vector, as shown in Figure 4.18. This vector rotates in the space with a frequency of the fundamental frequency of the inverter output, defined as f. The angle θ ($\theta = 2\pi f$) indicates which sector the rotating space vector falls in. Table 4.4 shows the relationship between the angle value and the sector, and the stationary vectors (active vectors and zero vectors) used for representing the rotational vector.

Sector	θ	Stationary vectors
I	$0 \leq \theta < \frac{\pi}{3}$	$\underline{V}_1 \underline{V}_2$ and $\underline{V}_{0(7)}$
II	$\frac{\pi}{3} \leq \theta < \frac{2\pi}{3}$	$\underline{V}_2 \underline{V}_3$ and $\underline{V}_{0(7)}$
III	$\frac{2\pi}{3} \leq \theta < \pi$	$\underline{V}_3 \underline{V}_4$ and $\underline{V}_{0(7)}$
IV	$\pi \leq \theta < \frac{4\pi}{3}$	$\underline{V}_4 \underline{V}_5$ and $\underline{V}_{0(7)}$
V	$\frac{4\pi}{3} \leq \theta < \frac{5\pi}{3}$	$\underline{V}_5 \underline{V}_6$ and $\underline{V}_{0(7)}$
VI	$\frac{5\pi}{3} \leq \theta < 2\pi$	$\underline{V}_6 \underline{V}_1$ and $\underline{V}_{0(7)}$

Table 4.4: Rotating space vectors location and their decomposed stationary vectors

The dwell time of the applied stationary vectors determines the duty-cycle of the corresponding switches in a sample period T_s and is calculated based on the 'Volt-second balancing' theory [78]. For a sufficiently short sample period T_s, the rotating space vector $\underline{v}_s$ can be regarded as constant value during the time interval of T_s. The product of the rotating space vector $\underline{v}_s$ and the sampling period T_s should be equal to the sum of the stationary vectors multiplied by their dwell time. For example, when a space vector is located in Sector I as shown in Figure 4.19, it can be decomposed into $\underline{V}_1$, $\underline{V}_2$ and $\underline{V}_{0(7)}$, with their times T_1, T_2 and T_0.

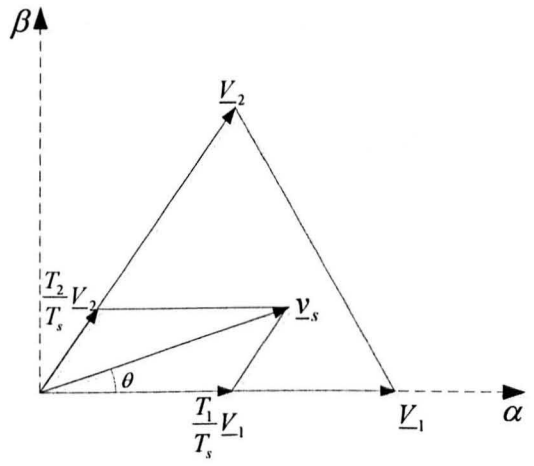

Figure 4.19: Diagram of a rotating vector falls in Sector I

From Table 4.3 and the volt-second balancing theory, (4-17) can be written:

$$\begin{aligned} &\underline{v}_s \cdot T_s = \underline{V}_1 \cdot T_1 + \underline{V}_2 \cdot T_2 + \underline{V}_0 \cdot T_0 \\ &\Rightarrow \\ &v_s e^{j\theta} \cdot T_s = \frac{2}{3} V_{dc} \cdot T_1 + \frac{2}{3} V_{dc} e^{j\frac{\pi}{3}} \cdot T_2 + 0, \qquad (0 \le \theta < \frac{\pi}{3}) \end{aligned} \tag{4-17}$$

Rewritten (4-17) in a stationary α-β plane, yielding:

$$\begin{cases} v_s \cos(\theta) \cdot T_s = \frac{2}{3} V_{dc} \cdot T_1 + \frac{1}{3} V_{dc} \cdot T_2 \\ v_s \sin(\theta) \cdot T_s = \frac{\sqrt{3}}{3} V_{dc} \cdot T_2 \end{cases} \tag{4-18}$$

Since $T_s = T_0 + T_1 + T_2$, solving (4-18) yields:

$$\begin{cases} T_1 = \frac{\sqrt{3} v_s T_s}{V_{dc}} \sin(\frac{\pi}{3} - \theta) \\ T_2 = \frac{\sqrt{3} v_s T_s}{V_{dc}} \sin(\theta) \\ T_0 = T_s - T_1 - T_2 \end{cases} \tag{4-19}$$

For vectors which fall in other sectors, a similar procedure can be applied. The general expression for the three stationary vector dwell times can be obtained by replacing the angular displacement θ with:

$$\theta' = \theta - (k-1)\pi/3 \tag{4-20}$$

where $k = 1, 2, ..., 6$ indicates that the vector falls in Sector I, II,…,VI, respectively.

The arrangement of the switching sequence of SVM is not unique, and a typical seven segment arrangement is adopted in this work due to its minimal switching frequency, as shown in Figure 4.20 for the case when a space vector resides in sector I.

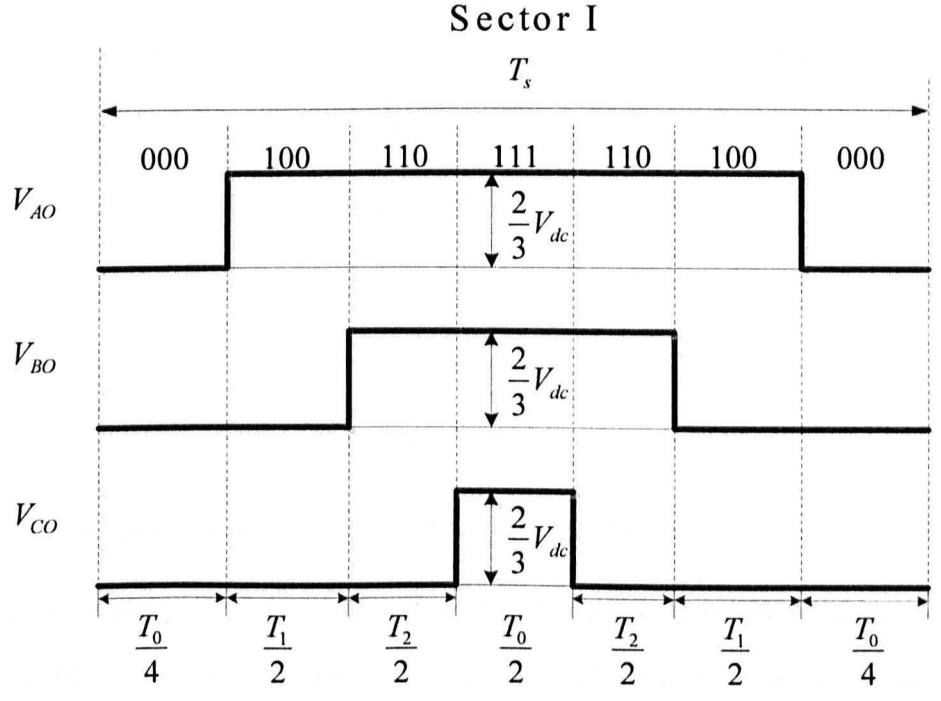

Figure 4.20: A typical seven segment switching sequence when $\bar{v}_s$ is in sector I

It can be noted that in one sampling period each switch only turns on and off once. Thus the switching frequency of the inverter as a whole is equal to the sampling frequency. Although the switching frequency can be decreased by using other switching sequences such as a five-segment sequence [78], where the redundent inactive vector V7(111) is eliminated and the duration of it is added to V0(000) at the start and end of the switching invertal resulting in a sequence of V0→V1→V2→V1→V0, it is not desirable to do so in this work

due to its increased THD.

4.9 Duty Cycle Modulation for the H-bridge

The timing signals for the single phase H-bridge to drive the DC load machine is also calculated in the DSP and the modulation scheme is described in this section. The DC load machine is under speed control as mentioned in section 4.6.2. The controller output is the demanded armature voltage, referred as the reference voltage V_{ref}.

The typical duty cycle modulation strategies for controlling a single phase full bridge (H-bridge) converter as shown in Figure 4.2 are Bipolar and Unipolar voltage switching methods. In bipolar type of switching, switches (Q_1, Q_4) and (Q_2, Q_3) are set to be two switching pairs. Each pair of switches turns on and off simultaneously, one of which is always on. Whilst for a unipolar type of switching, switches (Q_1, Q_4) and (Q_2, Q_3) are controlled independently, allowing Q_1 and Q_3 to be on or off at the same time. A unipolar voltage switching type duty cycle modulation is used in this research to generate the timing signal for the H-bridge due to its low output ripple characteristic [79]. The details of the two modulation strategies are described in the following sections.

4.9.1 Bipolar type duty cycle modulation

The switching sequence and the output of the bipolar type modulation strategy is illustrated in Figure 4.21. For a demanded armature voltage V_{ref}, a triangular carrier wave at the sample frequency T_s is used to compare with the demanded value. The amplitude of the carrier wave is chosen to equal to the DC link

voltage V_{dc} for simplicity. If V_{ref} is greater than the carrier, the first pair of switches (Q_1, Q_4) shown in Fig. 4.2 turns on while the other pair is off, vice versus. The output voltage v_o ranges between $-V_{dc}$ and V_{dc}, as the name bipolar indicated.

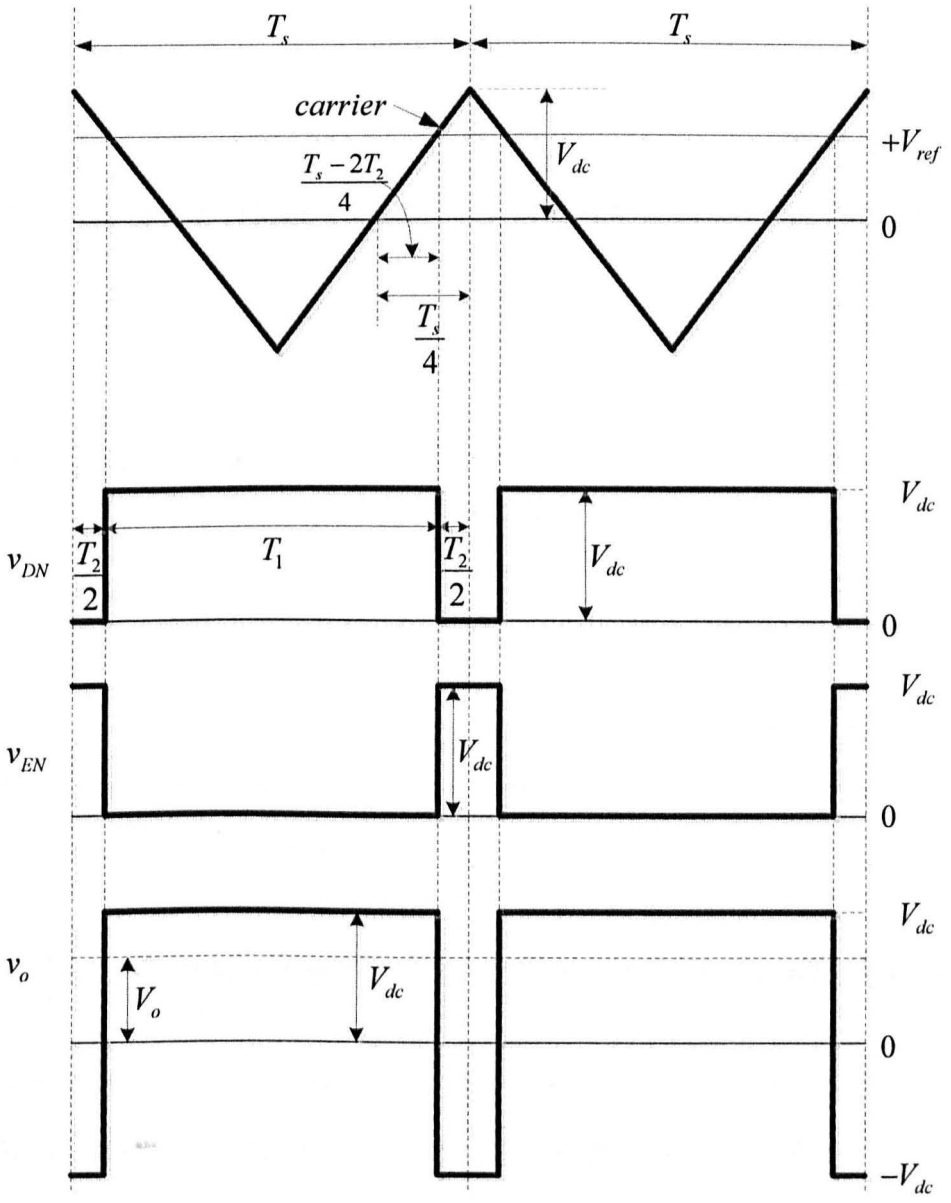

Figure 4.21: Switching sequence and the output of a bipolar modulation

The average output voltage of the converter can be obtained by subtracting the average value of the two terminal voltage V_{DN} and V_{EN}, with respect to the

negative DC bus in Figure 4.2. In the example of Figure 4.21, the conducting time of (Q_1, Q_4) in a sampling period is T_1, and the conducting time of (Q_2, Q_3) in the same time interval is T_2. Then V_{DN} and V_{EN} can be obtained as:

$$\begin{cases} V_{DN} = \dfrac{T_1}{T_s} V_{dc} \\ V_{EN} = \dfrac{T_2}{T_s} V_{dc} \\ T_s = T_1 + T_2 \end{cases} \tag{4-21}$$

Thus the output voltage averaged in a switching period can be derived as:

$$V_o = \frac{T_1 - T_2}{T_s} V_{dc} = \frac{T_s - 2T_2}{T_s} V_{dc} \tag{4-22}$$

Also, from the mathematical point of view, (4-23) can be written:

$$\begin{aligned} &\frac{V_{ref}}{V_{dc}} = \left(\frac{T_s - 2T_2}{4}\right) \Big/ \left(\frac{T_s}{4}\right) = \frac{T_s - 2T_2}{T_s} \\ &\Rightarrow V_{ref} = \frac{T_s - 2T_2}{T_s} V_{dc} \end{aligned} \tag{4-23}$$

Comparing (4-22) with (4-23), one can observe that the average voltage output is equal to the demanded value, as expected.

4.9.2 Unipolar type duty cycle modulation

The switching sequence and the output of the unipolar type modulation strategy is illustrated in Figure 4.22. The same demanded armature voltage V_{ref} as that for the bipolar type modulation is applied, and the triangular carrier wave with the same sampling frequency T_s and the same amplitude V_{dc} is used to compare with the demanded value. If V_{ref} is greater than the carrier, the upper switch of

the first leg in Figure 4.2 is on (Q_1 turns on and Q_2 turns off), vice versus. To obtain the switching sequence for second leg of the H-bridge $-V_{ref}$ is used to compare with the same carrier as that of the first leg. A similar approach is applied to generate the correct switching sequence for the second leg.

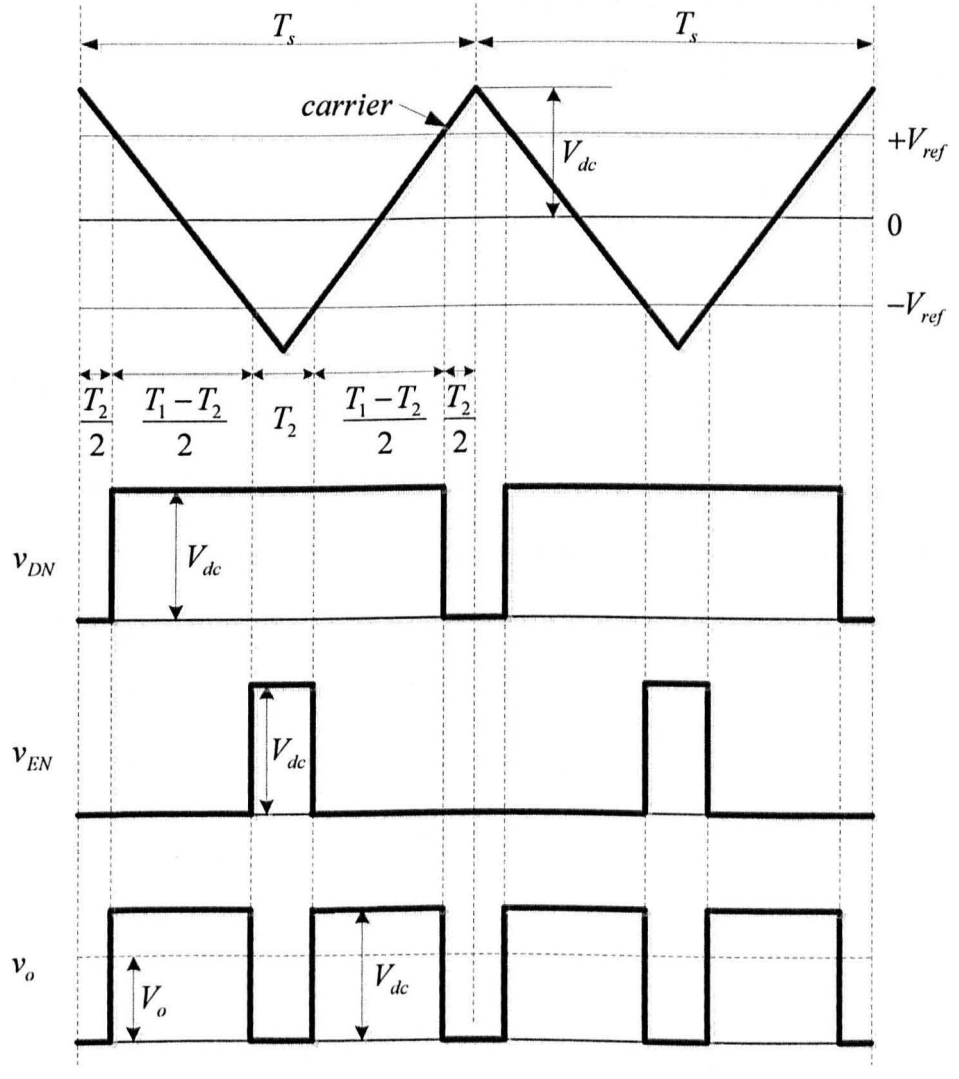

Figure 4.22: Switching sequence and the output of a unipolar modulation

Similar to the previous analysis for the bipolar type, the average output voltage is:

$$\begin{aligned} V_o &= V_{DN} - V_{EN} \\ &= \frac{T_1 - T_2}{T_s} V_{dc} \\ &= V_{ref} \end{aligned} \tag{4-24}$$

Comparing equation (4-24) with (4-22) and (4-23), it can be found that there is no difference between the average output voltages of the two types of modulation strategies for a given reference voltage. However, as the 'effective' switching frequency is doubled for a unipolar type, the voltage ripple presence in the unipolar PWM type of output is decreased with respect of the output from a same switching frequency bipolar type strategy [79].

4.10 Conclusions

The experimental rig consists of the AC-DC motor system, their driver system and the control platform, which were described in this chapter in detail. The controller design procedure and the modulation scheme used for generating the gating signals were also mentioned.

Chapter 5 Enhanced position estimation

5.1 Introduction

In this chapter, other issues associated with the high frequency signal injection based sensorless control have been addressed, including the initial discrimination between north and south poles, and the loading influences on estimation (i.e. the armature reaction). Possible measures to solve the aforementioned problems are discussed and evaluated through experiments.

5.2 Initial position detection

For a saliency tracking based sensorless PMSM control method, since the desired saliency being tracked is twice the electrical frequency, the polarity of the estimated position cannot be distinguished (i.e. north or south pole), and therefore the initial rotor position and its polarity must be detected.

The method used in this research for initial position detection is introduced in [64] and described as follows. Assuming a 2-pole PM motor with the rotor magnet at 0 and 180 degrees electrically (0 degree aligned with the stator phase *a*) as in Figure 5.1, the total flux in the d-axis direction is composed of the magnet

flux and the stator flux introduced by the d-axis current, yielding:

$$\begin{aligned} \psi_d &= \psi_m + \psi_{ad}, \qquad \theta_e = 0^\circ \\ \psi_d &= \psi_m - \psi_{ad}, \qquad \theta_e = 180^\circ \end{aligned} \tag{5-1}$$

where ψ_d, ψ_m and ψ_{ad} are the total d-axis flux, the magnet flux and the d-axis armature reaction flux ($\psi_{ad} = L_d i_d$), respectively.

If the d-axis stator current is rather high (i.e. the induced flux is rather large), the total flux in the d-axis direction is either saturated ($\theta_e = 0^\circ$) or de-saturated ($\theta_e = 180^\circ$). Consequently, the inductance in the d-axis direction is either decreased or increased. If a fixed amplitude voltage *v* is applied along the d axis, the d axis current flowing will be different for the two conditions. By comparing the values of the two currents, the positive d-axis (+d-axis) and the negative d-axis (-d-axis) can be distinguished.

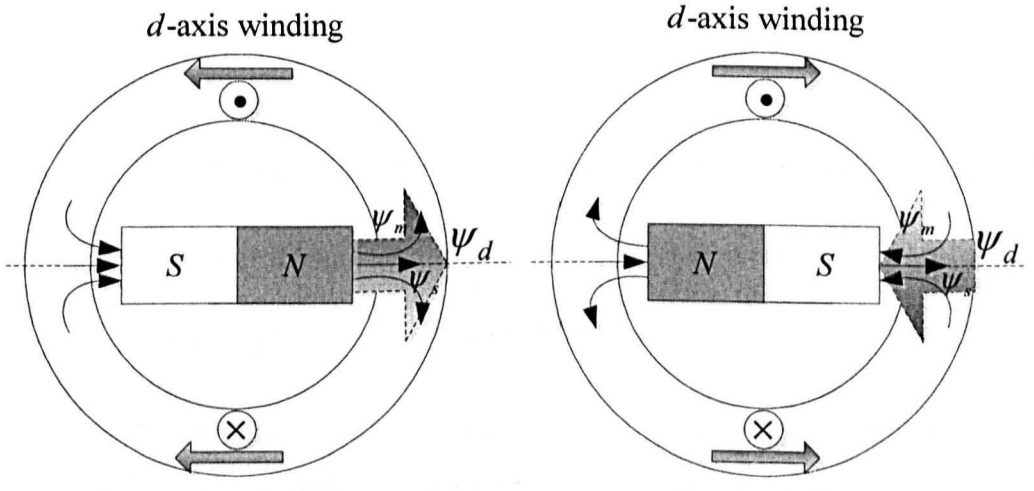

Figure 5.1: D-axis flux distribution of rotor position at 0 and 180 degrees (aligned with stator phase *a*)

To identify the polarity of an estimated rotor angle $\hat{\theta}_e$ obtained through the

saliency tracking sensorless method, two test voltage pulses with the same amplitude and duration (i.e. the same volt-second) are injected onto the estimated ±d-axes ($\pm\hat{\theta}_e$). With an injection voltage of high enough amplitude, the resultant current transients will produce a noticeable difference between the two peak values due to the impedance variation caused by the change in flux. The larger peak current value will be obtained when a positive V voltage is injected along the +d-axis. Thus the correct initial polarity of the rotor magnet can be identified.

The initial position detection scheme is shown as in Figure 5.2. In this figure, $\hat{\theta}_{e\_raw}$ represents the estimated rotor position without polarity identification, $\hat{\theta}_{e\_corr}$ represents the identified correct rotor initial position, which can be written as:

$$\hat{\theta}_{e\_corr} = \begin{cases} \hat{\theta}_{e\_raw}, & \text{if } i_d^{+d} > i_d^{-d} \\ \hat{\theta}_{e\_raw} + \pi, & \text{if } i_d^{+d} < i_d^{-d} \end{cases} \tag{5-2}$$

where i_d^{+d} is the resultant d-axis current when the voltage pulse is applied to the estimated positive d axis, and i_d^{-d} is the resultant d-axis current when the voltage pulse is applied in the opposite direction.

It is noted that the motor is kept at standstill throughout whole process of the initial estimation and polarity identification.

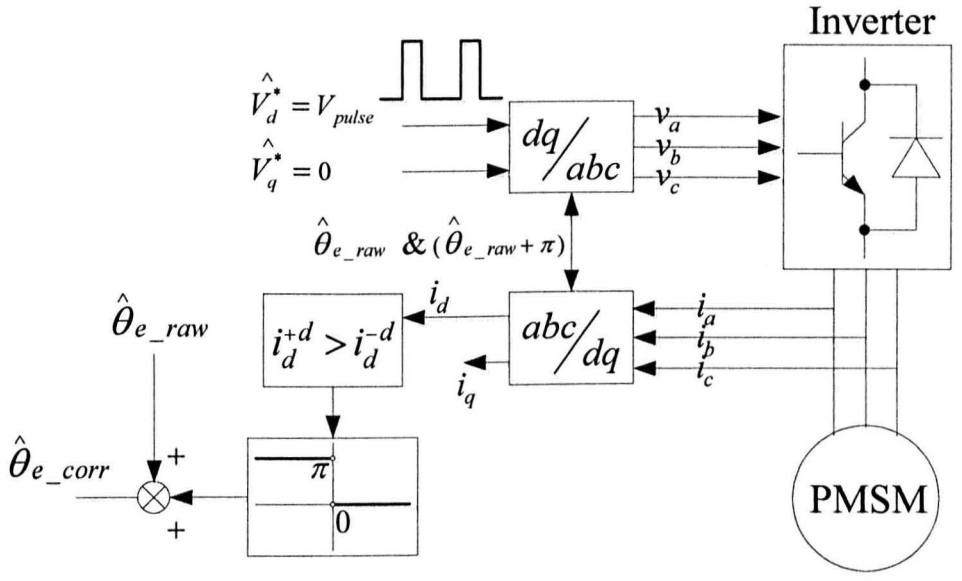

Figure 5.2: Initial polarity detection scheme

The scheme has been tested by experiment. The injected voltage has been set at 2V with 2ms pulse width, and the results for a correct initial polarity and an incorrect initial polarity from the estimation are shown as in Figure 5.3 and Figure 5.4.

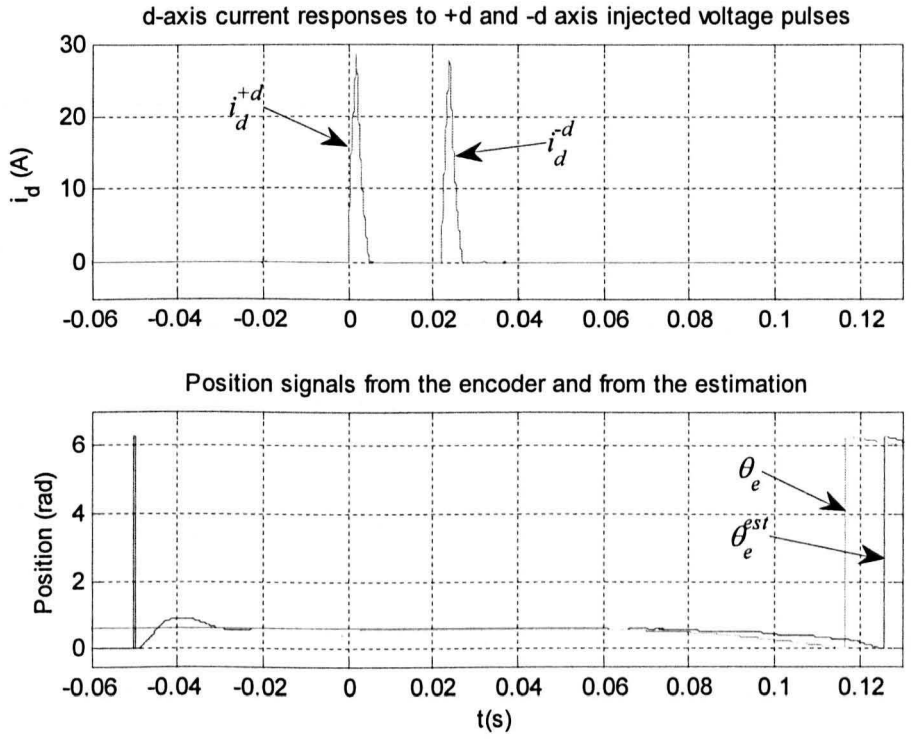

Figure 5.3: Initial polarity detection with correct initial polarity estimation

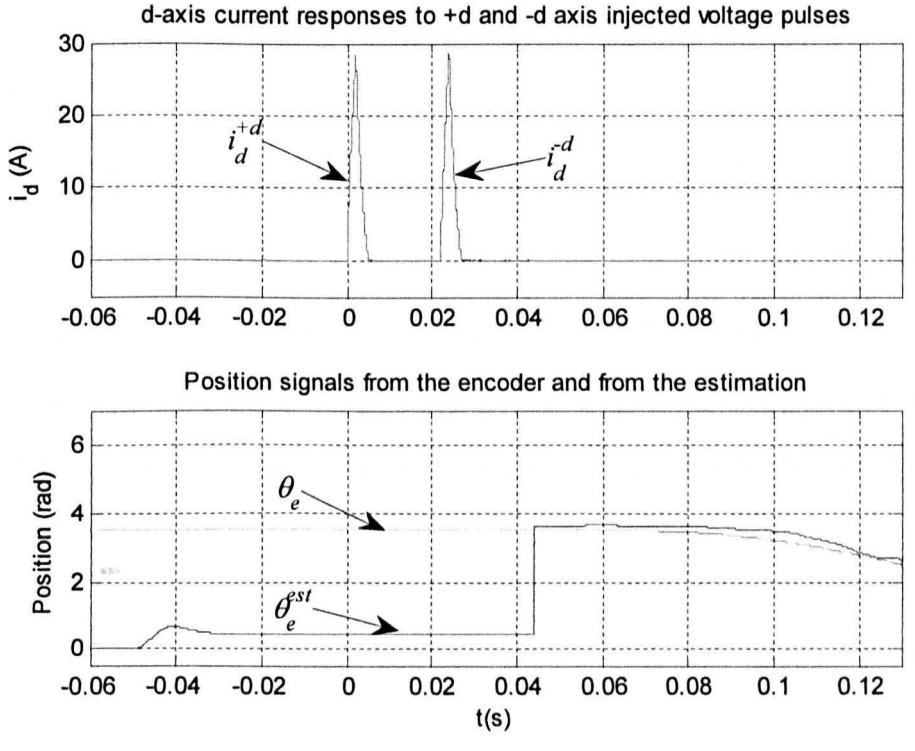

Figure 5.4: Initial polarity detection with incorrect initial polarity estimation

In Figure 5.3, the resultant current for the estimated +d-axis injection (i_d^{+d}) has a higher peak value than that of the estimated –d-axis injection (i_d^{-d}), which indicates that the estimated initial rotor position has a correct polarity so no compensation needed. In Figure 5.4, the initial rotor polarity is incorrect, which causes i_d^{+d} to be less than i_d^{-d}. Therefore, a compensation angle of 180° is needed to achieve the correct polarity.

5.3 Armature reaction

For a PMSM machine, the net flux linkage is the combination of the magnet flux and the stator induced flux. In a vector controlled system with a voltage source inverter, the flux distribution in a *dq* rotating frame can be written as:

$$\begin{aligned} \psi_d &= \psi_m + \psi_{ad} \approx \psi_m + L_d i_d \\ \psi_q &= \psi_{aq} \approx L_q i_q \end{aligned} \tag{5-3}$$

where ψ_{ad} and ψ_{aq} are the armature current induced flux in the rotating *d* and *q* axis respectively.

Since the d-axis current is normally controlled to zero to achieve maximum torque density, only the q-axis current component will affect the net flux. Thus a phase shift of the total flux is produced under loaded conditions, resulting in a misalignment between the total flux direction and the rotor d-axis, which can be illustrated as in Figure 5.5.

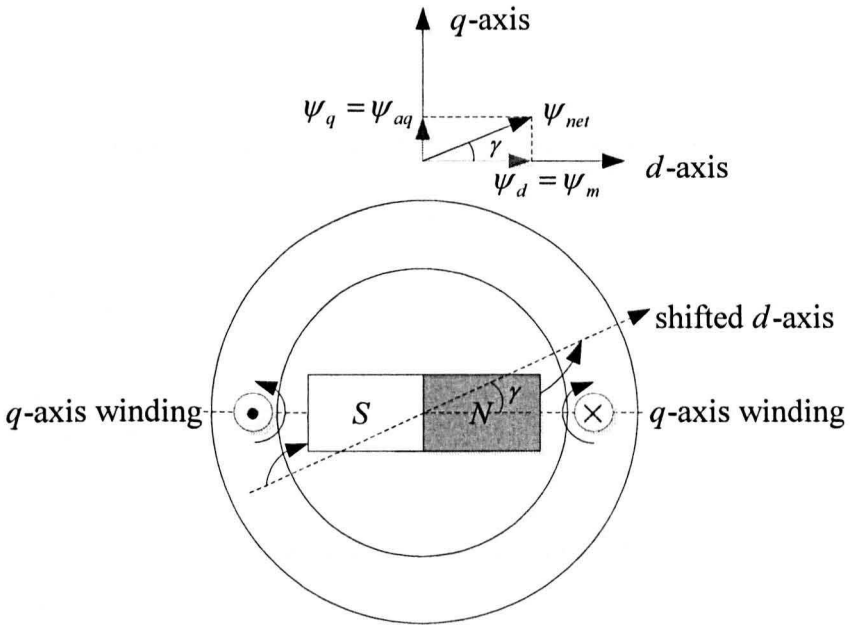

Figure 5.5: Total flux shift due to the armature reaction under loaded conditions

As can be seen from Figure 5.5 that with the increase of q-axis current (i.e. increased loading) the shift angle increases accordingly. The saliency tracking sensorless techniques track the maximum and minimum spatial impedances which are sinusoidally distributed according to the net flux spatial rather than the magnet flux. As a result, the shifted rotor electrical angle will be obtained.

5.3.1 Armature reaction compensation by adding predefined angle offset values

To achieve correct orientation for vector control, the simplest way to compensate this angle shift is to find the difference between the estimated angle and the one obtained from an encoder under sensored operation mode at different loading conditions. A look-up table or a linear function can be constructed to allow the correction of the estimated angle with different loading conditions for correct frame transformation. In this research the angle difference is approximated through a linear function as:

$$\hat{\theta}_{comp} = \hat{\theta}_e + f(i_q^*) \tag{5-4}$$

where $\hat{\theta}_{comp}$ and $\hat{\theta}_e$ are the corrected and un-corrected angle estimates, $f()$ stands for the linear function, and i_q^*-- the demanded torque current is used to access the function for angle compensation. The measured phase shifts, for the machine investigated, due to the armature reaction are shown in Figure 5.6 in radians from -60A to 60A.

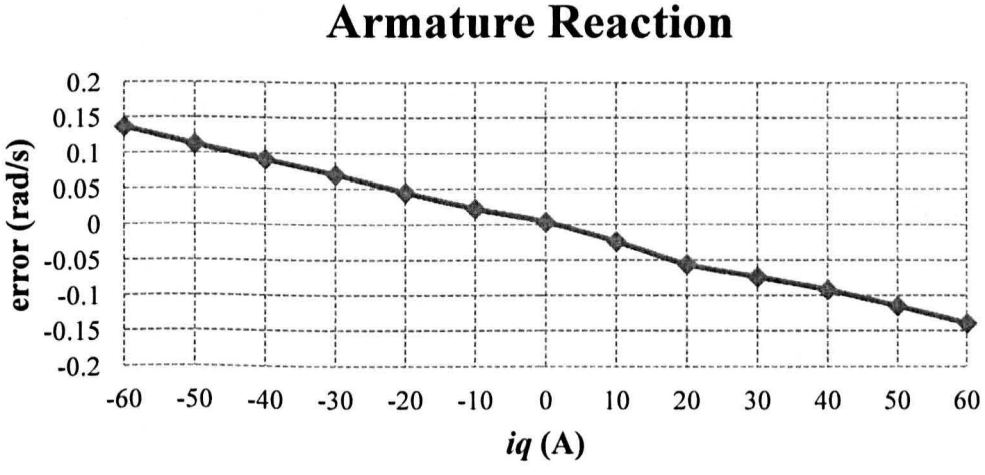

Figure 5.6: Phase shift of the angle estimate due to the armature reaction

Then the linear function $f(i_q^*)$ is obtained as:

$$f(i_q^*) = -0.0023 i_q^* - 0.0015 \tag{5-5}$$

However, the corrected angle $\hat{\theta}_{comp}$ for the motor fundamental model transformation cannot be used for the high frequency signal injection. This is because the saliency angle being tracked with this method is aligned with the direction of the net flux linkage not with the real *d-axis*. If the compensated angle is used, instability will be caused for the estimation process.

It should be noted that if the load current is sufficiently high, the *q-axis* flux will be saturated making the *q-axis* inductance reduced significantly. A failure of the

position estimation with the injection based sensorless method may occur when the *q-axis* inductance eventually approaches the *d-axis* inductance (in some cases, the sign of the difference may even reverse [80]), since the error signal used to drive the tracking mechanism will become almost zero independent of the alignment between the estimated and the real rotor position. It was found that in order to obtain a correct position estimate in this work, the load torque current has to be limited between -60A and 60A.

5.3.2 Armature reaction compensation by decoupling the cross coupling term

The other way of compensating the armature reaction is to take into account the cross coupling terms [81, 82] for the saliency tracking operation.

With the consideration of the cross coupling terms, the high frequency model can be written as:

$$\begin{bmatrix} v_{dh} \\ v_{qh} \end{bmatrix} = \frac{d}{dt} \begin{bmatrix} L_d & L_{dq} \\ L_{dq} & L_q \end{bmatrix} \cdot \begin{bmatrix} i_{dh} \\ i_{qh} \end{bmatrix} \tag{5-6}$$

The transformation matrix can be applied to transform the real *d-q* frame to the estimated *d-q* frame (the $\hat{d}$-$\hat{q}$ frame) with the inverse transformation defined as:

$$\begin{aligned} T(\Delta\theta_r) &= \begin{bmatrix} \cos(\Delta\theta_r) & \sin(\Delta\theta_r) \\ -\sin(\Delta\theta_r) & \cos(\Delta\theta_r) \end{bmatrix} \\ T^{-1}(\Delta\theta_r) &= \begin{bmatrix} \cos(\Delta\theta_r) & -\sin(\Delta\theta_r) \\ \sin(\Delta\theta_r) & \cos(\Delta\theta_r) \end{bmatrix} \end{aligned} \tag{5-7}$$

where $\Delta\theta_r = \hat{\theta}_r - \theta_r$ is the estimation error angle.

Equation (5-6) can be rewritten as:

$$\begin{aligned}\begin{bmatrix}\hat{v}_{dh}\\ \hat{v}_{qh}\end{bmatrix} &= T(\Delta\theta_\delta)\begin{bmatrix}v_{dh}\\ v_{qh}\end{bmatrix}\\ &= T(\Delta\theta_\delta)\cdot\frac{d}{dt}\begin{bmatrix}L_d & L_{dq}\\ L_{dq} & L_q\end{bmatrix}\cdot\begin{bmatrix}i_{dh}\\ i_{qh}\end{bmatrix}\\ &= T(\Delta\theta_\delta)\cdot\frac{d}{dt}\begin{bmatrix}L_d & L_{dq}\\ L_{dq} & L_q\end{bmatrix}\cdot T^{-1}(\Delta\theta_r)\cdot\begin{bmatrix}\hat{i}_{dh}\\ \hat{i}_{qh}\end{bmatrix}\end{aligned} \tag{5-8}$$

where L_d and L_q are the high frequency d and q axis inductances respectively.

After some calculation, equation (5-8) becomes [81]:

$$\begin{aligned}\begin{bmatrix}\hat{v}_{dh}\\ \hat{v}_{qh}\end{bmatrix} &= \frac{d}{dt}\begin{bmatrix} L_s-\Delta L_s'(\cos 2\Delta\theta_\delta\cdot\frac{\Delta L_s}{\Delta L_s'}-\sin 2\Delta\theta_\delta\cdot\frac{L_{dq}}{\Delta L_s'}) & \Delta L_s'\cdot(\sin 2\Delta\theta_\delta\cdot\frac{\Delta L_s}{\Delta L_s'}+\cos 2\Delta\theta_\delta\cdot\frac{L_{dq}}{\Delta L_s'})\\ \Delta L_s'\cdot(\sin 2\Delta\theta_\delta\cdot\frac{\Delta L_s}{\Delta L_s'}+\cos 2\Delta\theta_\delta\cdot\frac{L_{dq}}{\Delta L_s'}) & L_s+\Delta L_s'(\cos 2\Delta\theta_\delta\cdot\frac{\Delta L_s}{\Delta L_s'}-\sin 2\Delta\theta_\delta\cdot\frac{L_{dq}}{\Delta L_s'})\end{bmatrix}\cdot\begin{bmatrix}\hat{i}_{dh}\\ \hat{i}_{qh}\end{bmatrix}\\ &= \frac{d}{dt}\begin{bmatrix}L_s-\Delta L_s'\cdot\cos(2\Delta\theta_\delta+\theta_{ar}) & \Delta L_s'\cdot\sin(2\Delta\theta_\delta+\theta_{ar})\\ \Delta L_s'\cdot\sin(2\Delta\theta_\delta+\theta_{ar}) & L_s+\Delta L_s'\cdot\cos(2\Delta\theta_\delta+\theta_{ar})\end{bmatrix}\cdot\begin{bmatrix}\hat{i}_{dh}\\ \hat{i}_{qh}\end{bmatrix}\end{aligned} \tag{5-9}$$

where L_s and ΔL_s are the average and incremental self-inductances, defined by:

$$L_s=\frac{L_q+L_d}{2},\quad \Delta L_s=\frac{L_q-L_d}{2} \tag{5-10}$$

$\Delta L_s'$ is the incremental inductance accounting for the mutual inductance, and is given as:

$$\Delta L_s'=\sqrt{\Delta L_s^2+L_{dq}^2} \tag{5-11}$$

where L_{dq} is the mutual inductance between the d and q axes.

θ_{ar} is the angle offset due to the armature reaction, and is defined as:

$$\begin{aligned}\theta_{ar} &= \arctan\left(\frac{L_{dq}}{\Delta L_s^{'}} \Big/ \frac{\Delta L_s}{\Delta L_s^{'}}\right) = \arctan\left(\frac{L_{dq}}{\Delta L_s}\right) \\ &= \arctan\left(\frac{2L_{dq}}{L_q - L_d}\right)\end{aligned} \tag{5-12}$$

When under *d-axis* injection:

$$\begin{bmatrix} \hat{v}_{dh} \\ \hat{v}_{qh} \end{bmatrix} = V_i \begin{bmatrix} \cos(\omega_i t) \\ 0 \end{bmatrix} \tag{5-13}$$

The high frequency current in the estimated *dq* axis under *d-axis* injection can be written as:

$$\begin{bmatrix} \hat{i}_{dh} \\ \hat{i}_{qh} \end{bmatrix} = \frac{V_i \sin(\omega_i t)}{\omega_i (L^2_s - \Delta L_s^{'2})} \begin{bmatrix} L_s + \Delta L_s^{'} \cos(2\Delta\theta_r + \theta_{ar}) \\ -\Delta L_s^{'} \sin(2\Delta\theta_r + \theta_{ar}) \end{bmatrix} \tag{5-14}$$

If the angle estimation error $\Delta\theta_r$ is sufficiently small, by using (5-12), equation (5-14) can be rewritten as:

$$\begin{bmatrix} \hat{i}_{dh} \\ \hat{i}_{qh} \end{bmatrix} = \frac{V_i \sin(\omega_i t)}{\omega_i (L^2_s - \Delta L_s^{'2})} \begin{bmatrix} L_q - 2\Delta\theta_r L_{dq} \\ -L_{dq} - 2\Delta\theta_r \Delta L_s \end{bmatrix} \tag{5-15}$$

By demodulating the high frequency current vector from the carrier signal and low pass filtering, it becomes:

$$\begin{bmatrix} \hat{i}_{dh\_lp} \\ \hat{i}_{qh\_lp} \end{bmatrix} = \frac{V_i}{2\omega_i (L^2_s - \Delta L_s^{'2})} \begin{bmatrix} L_q - 2\Delta\theta_r L_{dq} \\ -L_{dq} - 2\Delta\theta_r \Delta L_s \end{bmatrix} \tag{5-16}$$

By solving equation (5-16), the error $\Delta\theta_\delta$ can be written as:

$$\Delta\theta_r = -\frac{V_i}{4\omega_i(L^2{}_s - \Delta L_s^{'2})}(\hat{i}_{qh\_lp} + \frac{L_{dq}}{L_q}\hat{i}_{dh\_lp}) \tag{5-17}$$

It can be seen that the estimation error is proportional to the term $(\hat{i}_{qh\_lp} + \frac{L_{dq}}{L_q}\hat{i}_{dh\_lp})$. By forcing this term to zero, the estimate will be aligned to the real rotor position. This term, rearranged as equation (5-18), is recognized as the error signal to drive the tracking mechanism.

$$\xi = (\hat{i}_{qh} + \lambda\hat{i}_{dh}) = -\frac{4\omega_i(L^2{}_s - \Delta L_s^{'2})}{V_i}\cdot\Delta\theta_r \tag{5-18}$$

where the value $\lambda = \frac{L_{dq}}{L_q}$ is defined as the cross coupling coefficient and can be calculated either by FE (finite element) analysis or by experiments [81].

The experimental method to derive λ is to inject the *hf* voltage vector into the real d-axis, and the *hf* voltage equation is given as:

$$\begin{bmatrix} V_i\cos(\omega_i t) \\ 0 \end{bmatrix} = \frac{d}{dt}\begin{bmatrix} L_d & L_{dq} \\ L_{dq} & L_q \end{bmatrix}\begin{bmatrix} i_{dh} \\ i_{qh} \end{bmatrix} \tag{5-19}$$

Then the corresponding *hf* current can be obtained as:

$$\begin{bmatrix} i_{dh} \\ i_{qh} \end{bmatrix} = \frac{1}{L_d L_q - L^2{}_{dq}}\begin{bmatrix} \frac{C(1-L_d L_q)}{L_{dq}} + \frac{V_i\sin(\omega_i t)}{\omega_i}L_q \\ C\cdot L_d - \frac{V_i\sin(\omega_i t)}{\omega_i}L_{dq} \end{bmatrix} \tag{5-20}$$

where C is a constant resulting from the integration operation. Similar to equation (5-15), after multiplying (5-20) by the carrier signal and low pass filtering, the resultant current vector is obtained as:

$$\begin{bmatrix} i'_{dh} \\ i'_{qh} \end{bmatrix} = \frac{V_i}{2\omega_i (L_d L_q - L^2_{dq})} \begin{bmatrix} L_q \\ -L_{dq} \end{bmatrix} \tag{5-21}$$

The cross coupling coefficient λ can be calculated through:

$$\lambda = \frac{L_{dq}}{L_q} = -\frac{i'_{qh}}{i'_{dh}} \tag{5-22}$$

The overall schematic of measuring the cross coupling coefficient is shown in Figure 5.7.

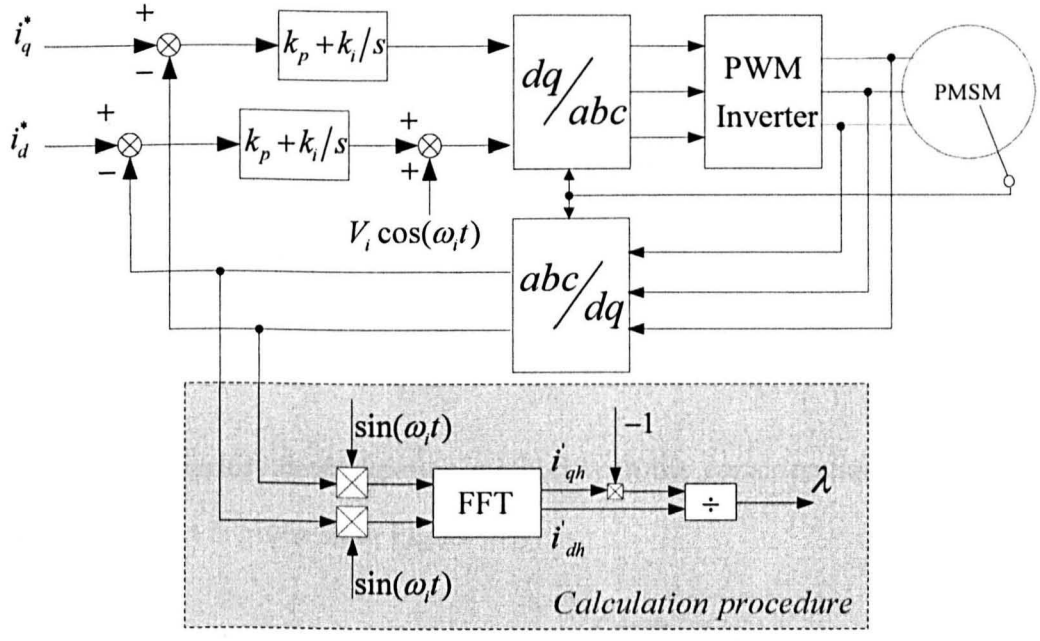

Figure 5.7: Scheme of measuring the cross coupling coefficient

As noted from Figure 5.7, an FFT operation rather than low pass filters is performed to obtain the current vector in equation (5-21). This is to avoid additional delay from the filters to give an accurate measurement of λ, and is acceptable as this is a one-off commissioning procedure. The measured coefficient is plotted as in Figure 5.8.

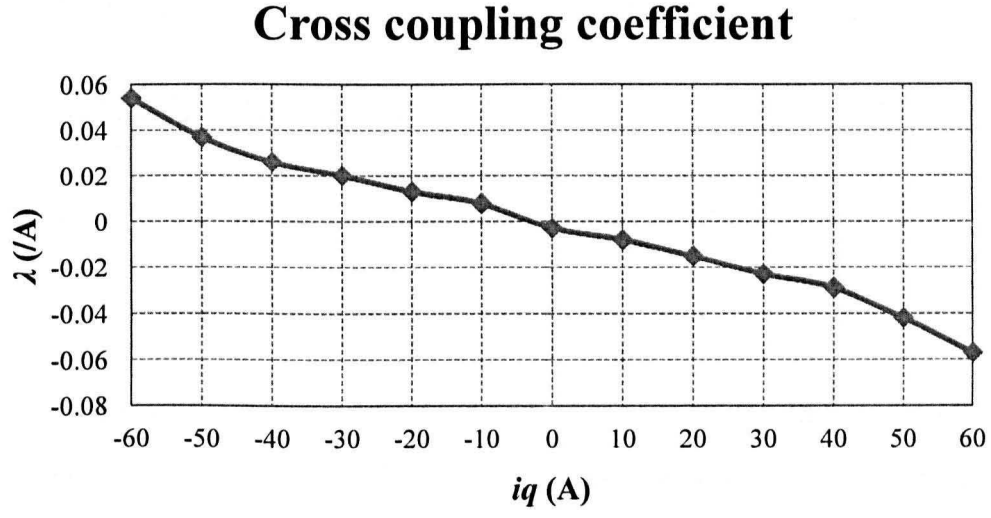

Figure 5.8: Measured cross coupling coefficient values

The coefficient λ can be linearized and derived as:

$$\lambda = -0.0008 \cdot i_q^* - 0.0015 \tag{5-23}$$

where i_q^* is the demanded torque current. i_d^* is kept zero at all time.

Then the sensorless demodulation method with the consideration of the cross coupling effect is given as in Figure 5.9.

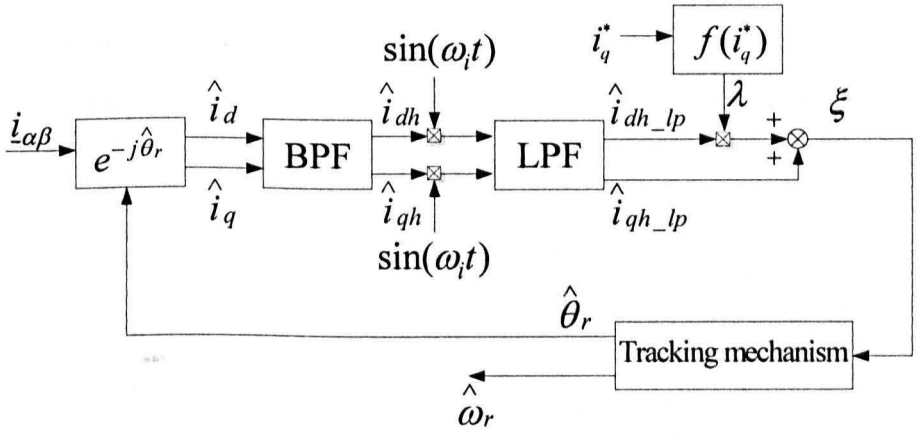

Figure 5.9: Demodulation scheme with cross coupling effect decoupled

5.3.3 Compensation results for the two mentioned methods

The results for the armature reaction compensation using the encoder measured angle offsets and decoupling the cross coupling terms are compared in this section. The AC motor is operated under torque control and the DC load machine holds the speed at -60 rpm. Results for motor under light loads (10A, 11%) and heavy loads (50A, 56%) are taken and shown from Figure 5.11 to Figure 5.17, and the corresponding load currents waveforms are shown in Figure 5.10 and Figure 5.14.

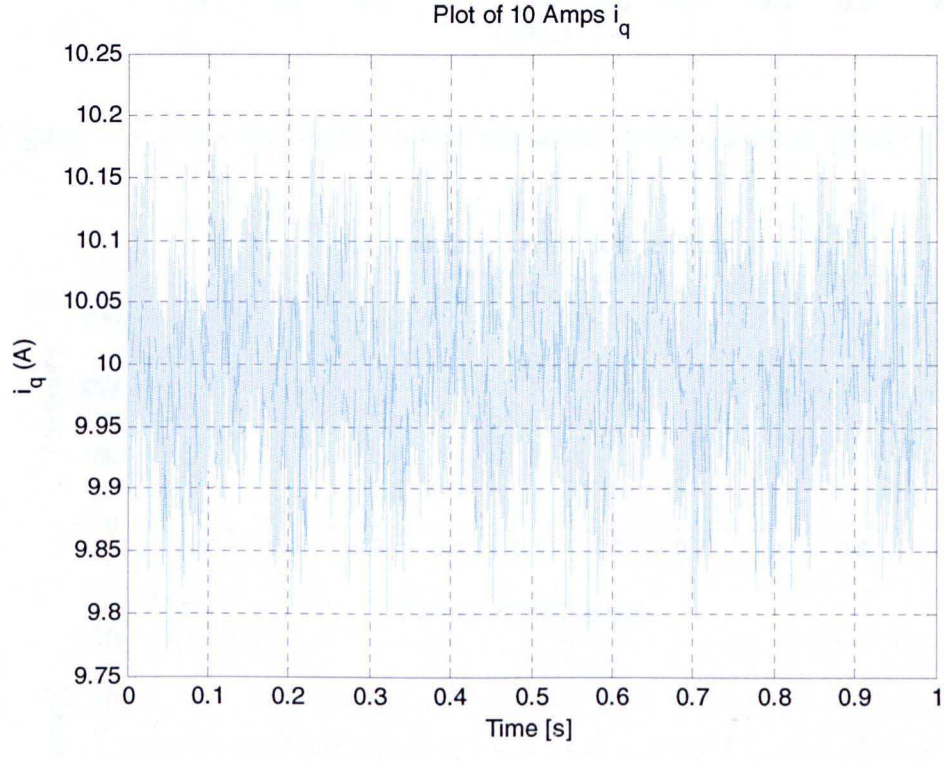

Figure 5.10: Plot of 10A (11%) i_q with sensorless operation

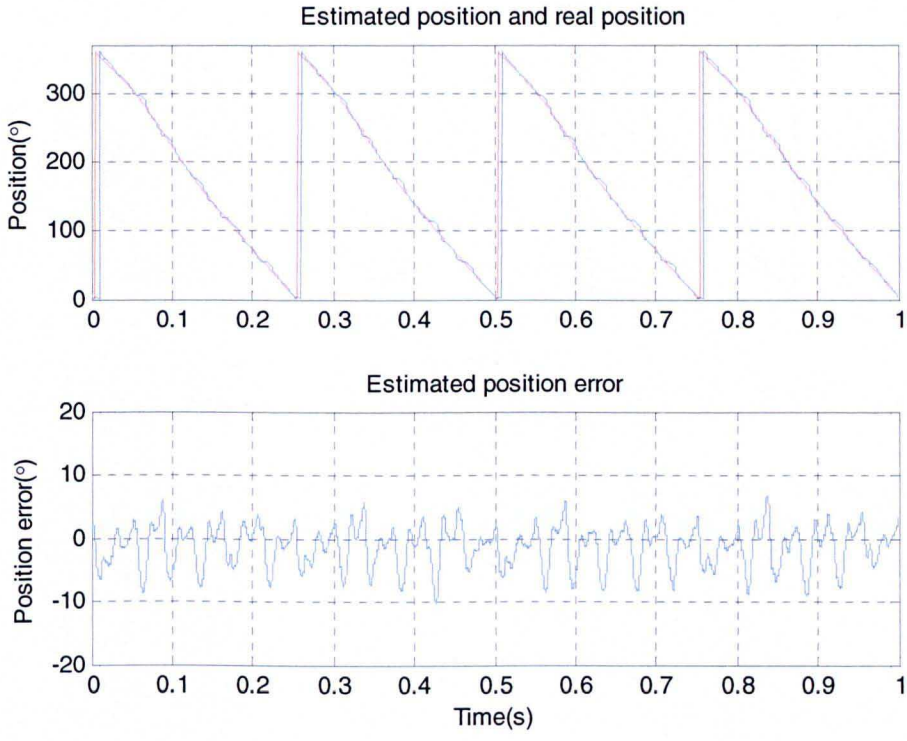

Figure 5.11: Obtained angle without armature compensation at 10A (11%) load

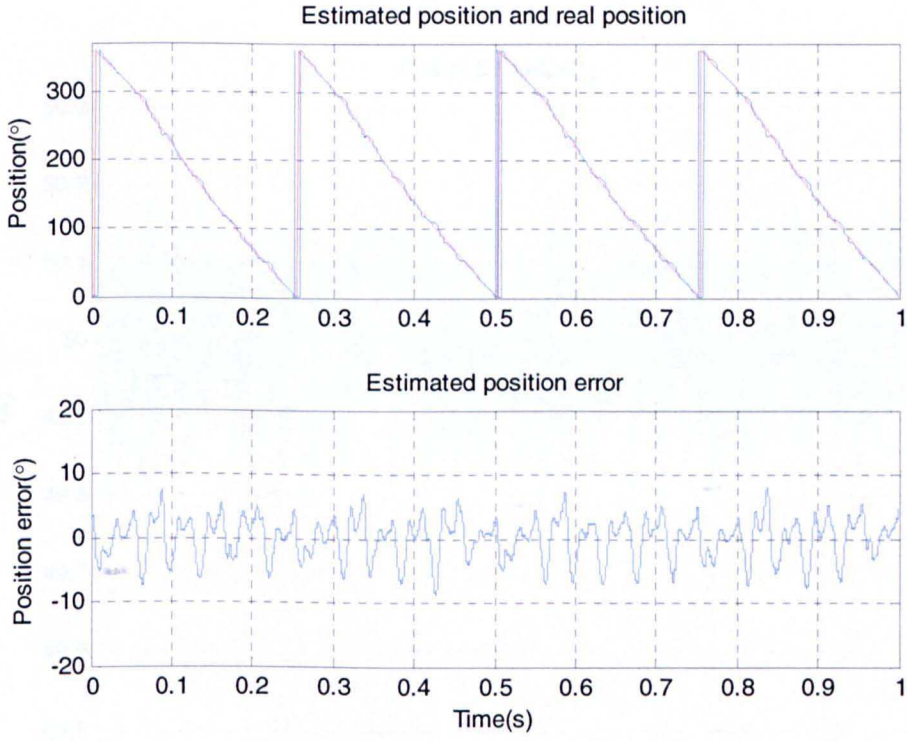

Figure 5.12: Results of armature compensation by predefined offset at 10A (11%) load

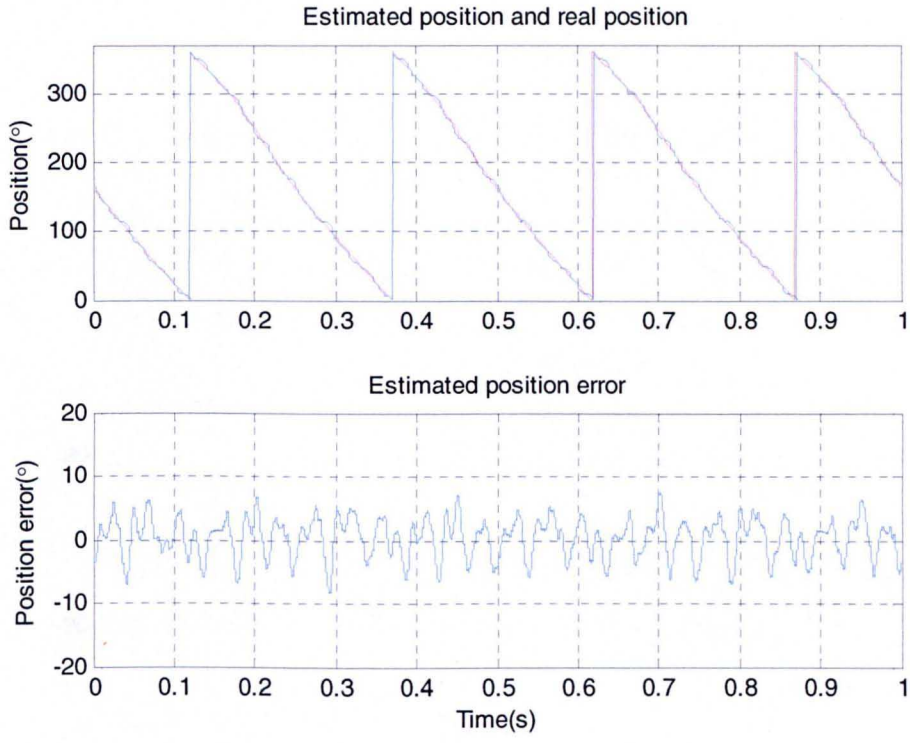

Figure 5.13: Results of armature compensation by decoupling the cross coupling term at 10A (11%) load

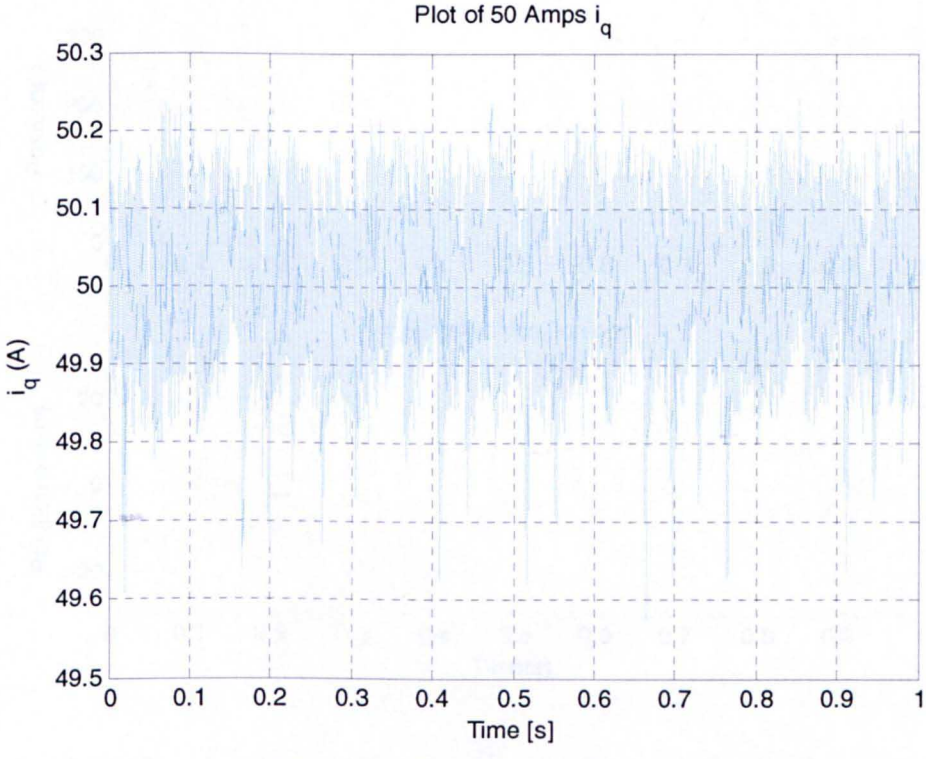

Figure 5.14: Plot of 50A (56%) i_q with sensorless operation

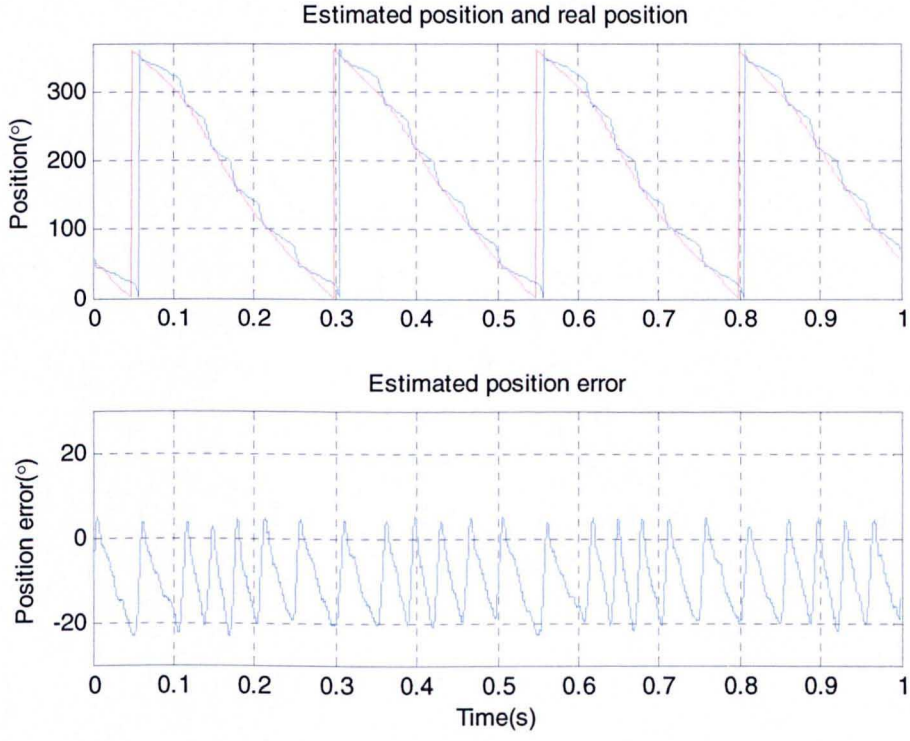

Figure 5.15: Obtained angle without armature compensation at 50A (56%) load

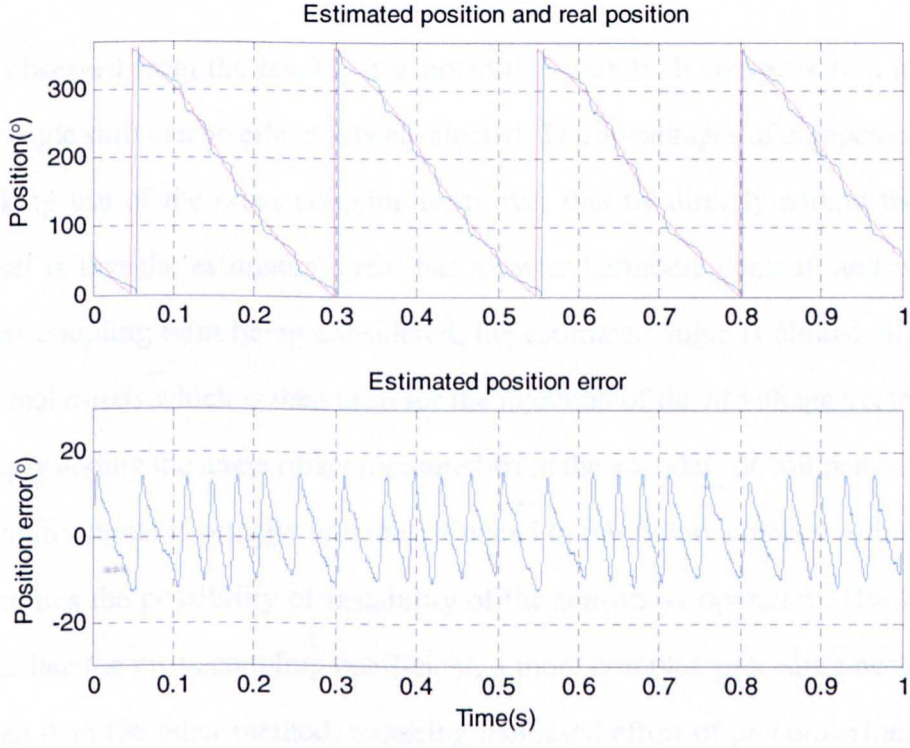

Figure 5.16: Results of armature compensation by predefined offset at 50A (56%) load

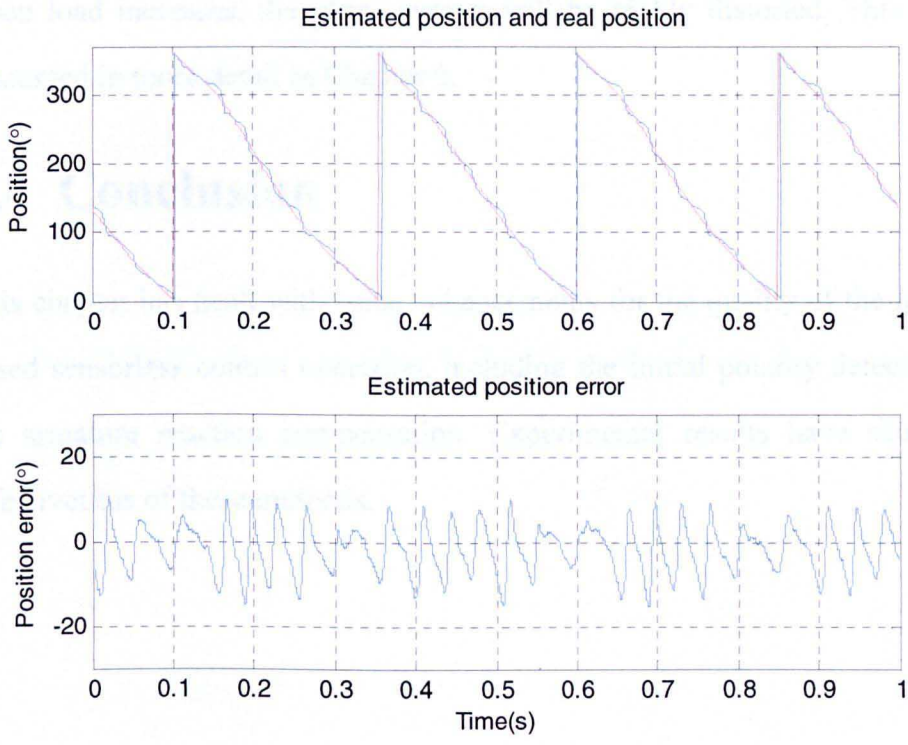

Figure 5.17: Results of armature compensation by decoupling the cross coupling term at 50A (56%) load

As observed from the results, it is noted that with both compensation methods the angle shift can be effectively eliminated. The advantages of compensation by making use of the cross coupling term over that by directly adding the angle offset is that the estimation error has a lower harmonic content, and with the cross coupling term being considered, the estimated angle is almost aligned to the real *d-axis* which is then used for the injection of the *hf* voltage vector. With simply adding the angle offset measured from the encoder for compensation, the injection signal is actually into the estimated d-axis before compensation, which increases the possibility of instability of the sensorless operation. However, to calculate the cross coupling coefficient, a more complex procedure needs to be taken than the other method, requiring increased effort of precomissioning and complexity of the system setup, and for this reason the linear function compensation method has been used for the rest of this work. It is also noted that

when load increases, the phase current will be highly distorted. This will be discussed in more detail in Chapter 6.

5.4 Conclusion

This chapter has dealt with some enhancements for the quality of the injection based sensorless control operation, including the initial polarity detection and the armature reaction compensation. Experimental results have shown the effectiveness of these methods.

Chapter 6 Sensorless vector torque control results

6.1 Introduction

In this Chapter, the results taken from the test rig will be shown to illustrate the performance of the motor drive system using the three injection-based sensorless methods discussed. The results are compared in terms of the current distortion they produce, audible noise, and dynamic performance. Results from the sensored vector controlled system are used as a benchmark with which to assess the sensorless methods.

6.2 Current distortion for the different sensorless methods

In this section, the current distortion of the line currents for the different *hf* injection sensorless methods is evaluated. The test rig setup was described in Chapter 4. The DC load machine was operated with speed control and the PMAC machine utilized the position signals obtained either from the encoder for the sensored operation or from the estimation for the sensorless operation to perform torque control. The motor was rotating at -60rpm and -120rpm between

-60A and 60A loading conditions. The current data were measured using a LeCroy CP150 current probe [83] and captured for 2 seconds by a Lecroy WaveSufer-424 oscilloscope [84] with 100 kHz sampling rate. They were uploaded to a host PC and then processed offline using Matlab software. Current distortion can be regarded as an indication of the torque ripple. The distorted current components will bring additional torque variations at different frequencies. Since some of them cannot be filtered out by the mechanical coupling of the system due to the frequencies being higher than the bandwidth of the mechanical model (composed with inertia and friction terms), they are the main source of the torque ripple to degrade the control performance and affect the EPS applications. The Total Harmonic Distortion (THD) [79] of the line currents has been calculated to quantify the quality of the line currents and thus to evaluate the torque ripple.

6.2.1 The current distortion for the sensored system — the benchmark

The current distortion for a sensored control system – the benchmark, is first investigated. The results of the THDs of the line current are shown in Figure 6.1.

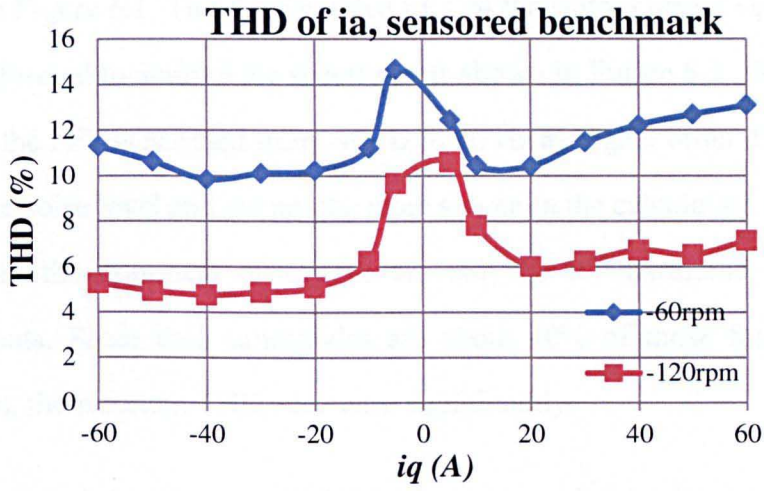

Figure 6.1: THD of i_a for the sensored benchmark at -60rpm and -120rpm

From Figure 6.1, it can be seen that the current distortion reaches its peak THD value close to no load due to the small amplitude of the load current. With the increase of load, the THD gets smaller since the harmonics due to the cogging torque and other mechanical disturbances are relatively fixed in amplitude and are therefore a smaller percentage of the fundamental component. At above 20A load the THD increases by a small amount. However, by looking at the spectrum of the normalized stator current vector ($\underline{i}_s$), as shown in Figure 6.2, it is found that under 60A load a large second harmonic of the current is present as well as a DC component. The 2nd harmonic of current represents a torque disturbance at the frequency f_e with respect to the fundamental electromagnetic torque which is partly due to the cogging torque of the PMAC machine as it links to the pole number of the machine (8 poles). The DC component represents a $-f_e$ torque disturbance which is partly due to the commutation disturbance of brushes on the DC machine. Also there is a 3rd harmonic in the current in both conditions. This is due to imbalances in the PMAC machine phase impedances. Any variation in connections or windings will cause a noticeable imbalance.

With the increase of rotating speed, the THDs of the line currents decrease, as

shown in Figure 6.1. The double-sided FFT of the stator current vector has also been performed to analyse the spectrum, as shown in Figure 6.3. The frequency range of the FFT is zoomed from -40 Hz to 40 Hz as higher order distortions are below the noise level and are not the main source in the calculation of THD. It is noted that the dominant distortions are still the 2^{nd} harmonic and the DC components. Since their amplitudes are about 40% of those for the -60rpm condition, the resultant THDs decrease significantly.

It is also noted that the current THDs for the positive load levels are slightly bigger than the negative load levels. The reason for this is not clear and needs to be further investigated.

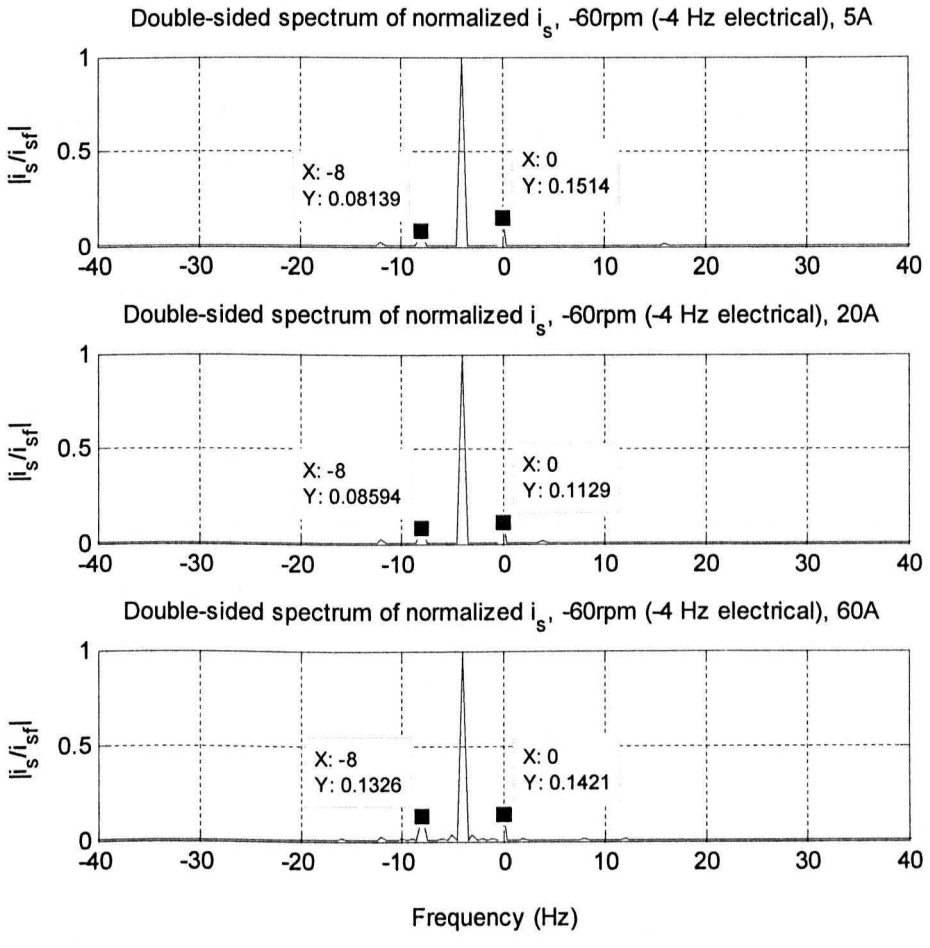

Figure 6.2: Normalized double-sided spectrum of $\underline{i}_s$ for a sensored drive running at -60rpm (-4 Hz electrical) under 5A, 20A and 60A loads

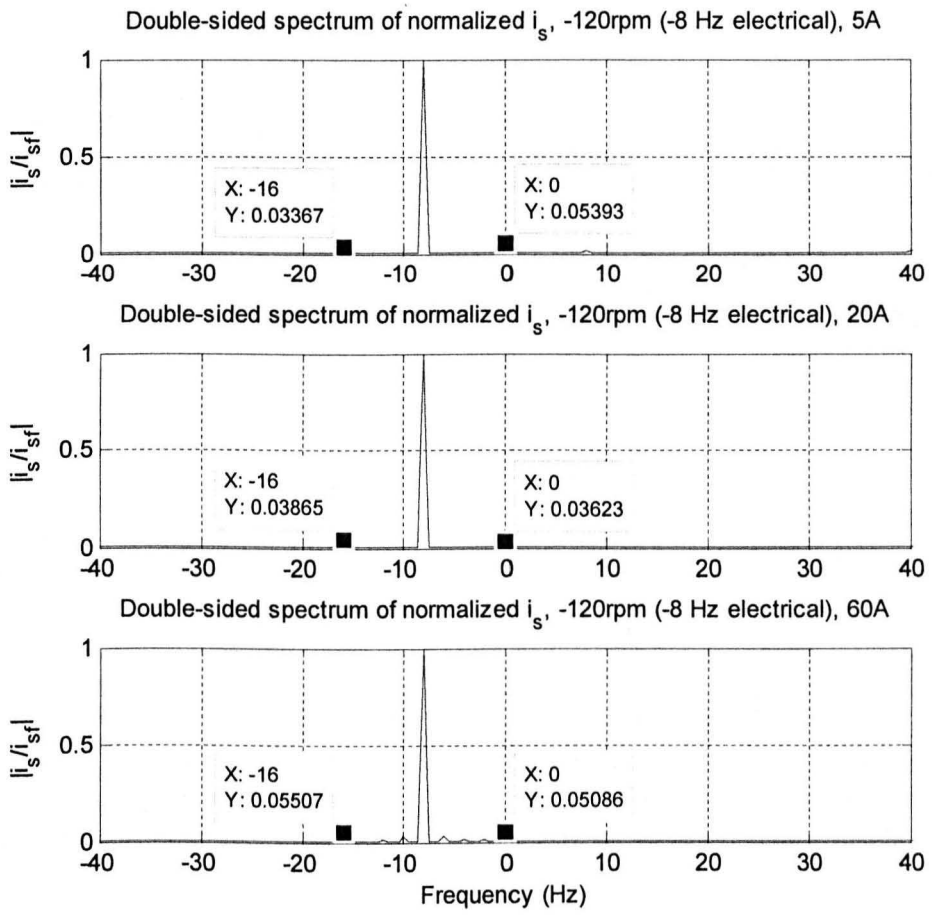

Figure 6.3: Normalized double-sided spectrum of $\underline{i}_s$ for a sensored drive running at -120rpm (-8 Hz electrical) under 5A, 20A and 60A loads

6.2.2 The effect of *hf* injection on the current distortion

To illustrate the effect of the *hf* signal injection *only* on the current distortion, position signals obtained from the encoder (θ) and from sensorless operation ($\hat{\theta}$) are used for the closed loop control with voltage injection applied in both cases. The THDs of the line currents for both cases are shown in Figure 6.4 at -60rpm and -120rpm under different load levels. The pulsating signals are 1.5 kHz and 2 kHz sinusoidal voltage vectors with amplitudes of 1.3V and 1.7 V respectively

into the estimated *d-axes*.

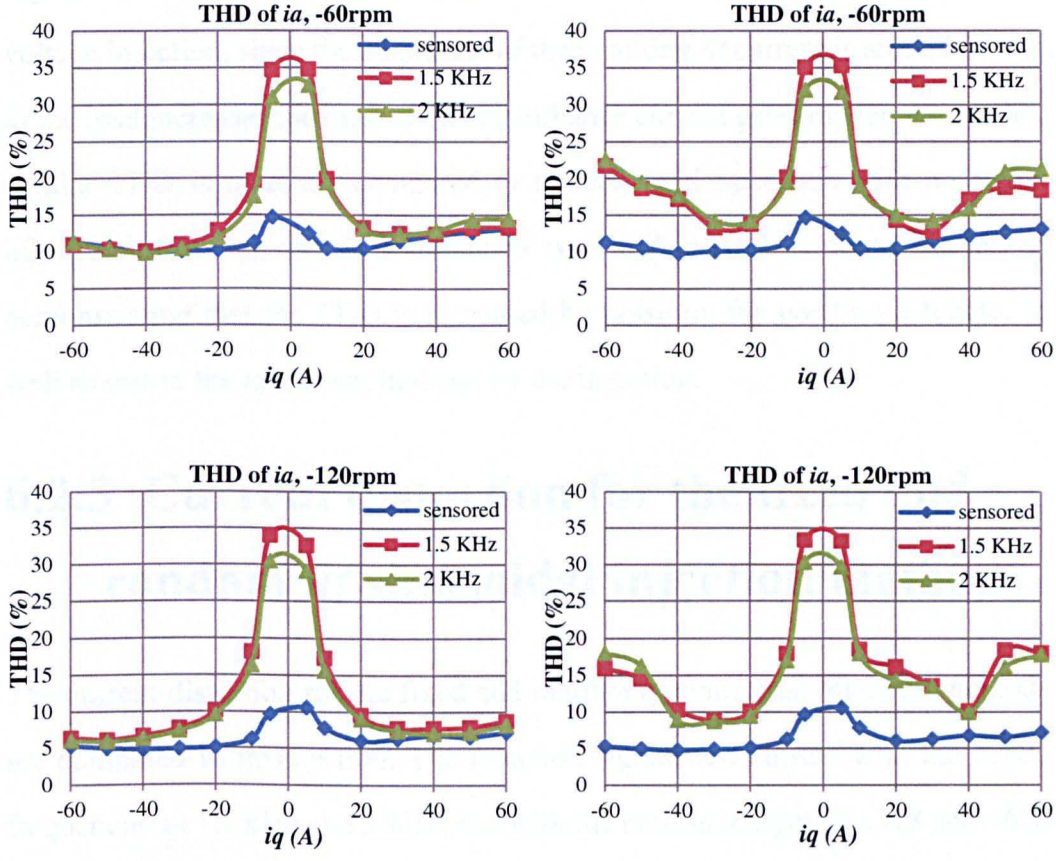

(a) Sensored, using θ (b) Sensorless, using $\hat{\theta}$

Figure 6.4: THDs of i_a for fixed frequency sinusoidal injection with sensored and sensorless operations at -60rpm and -120rpm under different load conditions

It is clear that when load current is below ±20A, there is an agreement between the current distortions for the sensored operation with *hf* voltage injection to the estimated *d-axis* and for the sensorless operation. However, when the load current is increased further, the distortion of the line current in sensored operation with voltage injection becomes close to that for sensored operation without voltage injection, and this is less distorted than the full sensorless operation. This is because at higher load levels, the motor has strong higher order saliencies [80] which will interfere with the tracking procedure in a

sensorless system and degrade the quality of the position estimate, and hence a higher distortion in current is expected. For the sensored operation with *hf* voltage injection, since the amplitude of the resulting *hf* current is around 1 Amp, as the load increases the ratio of this disturbance current gets smaller. As a result, similar THD is obtained compared to the sensored operation with no signal injection. However, the THD obtained with full sensorless control is larger, demonstrating that the THD is increased by noise on the position estimate, as well as due to the *hf* current induced by the injection.

6.2.3 Current distortion for the fixed and random *hf* sinusoidal injection methods

The current distortion for the fixed and random *hf* sinusoidal injection methods are compared in this section. The injection signals are chosen with the centre frequencies at 1.5 kHz and 2 kHz, and with the random ranges of ±328 and ±656 Hz. The results of the line current THDs are shown in Figure 6.5.

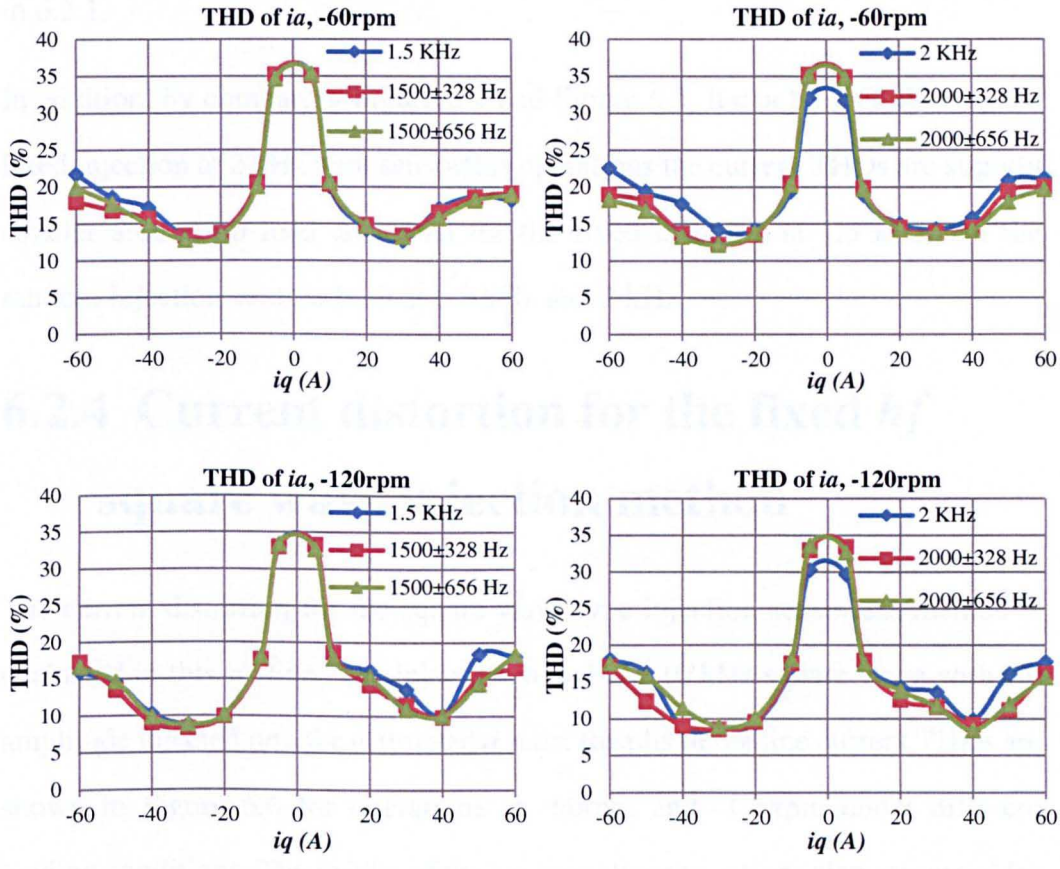

(a) injection centred at 1.5 kHz (b) injection centred at 2 kHz

Figure 6.5: THDs of i_a for fixed and random sinusoidal injection sensorless operations at -60rpm and -120rpm under different load conditions

As shown in Figure 6.5, the current distortion for fixed and random *hf* sinusoidal injection sensorless methods is similar. This is because the sum of power of the *hf* current components for the random injection method is comparable to that of the fixed injection method. It also indicates that for the same operating point and SNRs (Signal-to-Noise Ratio) the torque ripple due to the estimation error is not affected significantly by the injection types (fixed or random) or injection frequencies since otherwise the difference in estimation error will bring different ripple components to the current resulting in different THD values. As the speed increases, the current distortions decrease slightly as well since a lower amount of disturbances due to the construction of the machine itself appears as discussed

in 6.2.1.

In addition, by comparing Figure 6.4 and Figure 6.5, it can be seen that for the fixed injection at 2 kHz with sensorless operations the current THDs are slightly smaller around no load area than for the fixed injection at 1.5 kHz and the random injection centred both at 1.5 kHz and 2 kHz.

6.2.4 Current distortion for the fixed *hf* square wave injection method

The current distortion for the square wave type injection sensorless method is evaluated in this section. The injection signal is a 10 kHz square wave with 3V amplitude injected into the estimated *d-axis*. Results of the line current THDs are shown in Figure 6.6 for operations at -60rpm and -120rpm under different loading conditions. The results of the sensored benchmark are also presented for comparison.

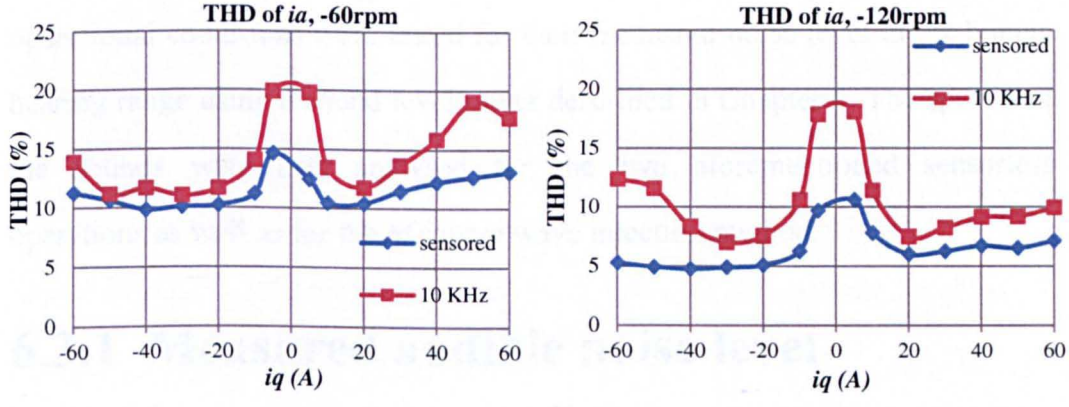

Figure 6.6: THDs of i_a for 10 kHz square wave injection sensorless operations at -60rpm and -120rpm under different load conditions

It is noted that under low loads, the current distortion for sensorless operation is much higher than those for the sensored benchmark due to the low values of the fundamental current. When the load increases, the distortion tends to decrease

and increase again above ±20A, which is quite similar to the behaviour of the sinusoidal injection described in 6.2.2. The increase of speed also results in lower THD as for the other sensorless methods mentioned previously.

By comparing the current distortions with those obtained through sinusoidal injection, it is found that the THDs are less for the square wave injection method. This is because the resultant *hf* currents are nearly 60% of the sinusoidal injection methods (around 0.6A). A higher injection voltage will result in control failure especially at high load as it is limited by the inverter output when a 12V DC-link voltage is used. However the consequence of this is that the maximum step change in load torque that can be achieved for the square wave injection method is lower than for the sinusoidal injection.

6.3 Audible noise

The sensored benchmark and sensorless operation using fixed *hf* sinusoidal injection methods and random *hf* sinusoidal injection methods with different operational conditions were tested for their meausred noise level in the human hearing range using a sound level meter described in Chapter 4. The spectra of the sounds were also analysed for the two aforementioned sensorless operations as well as for the *hf* square wave injection method.

6.3.1 Measured audible noise level

The results of the audible noise level measurements for the fixed and random *hf* sinusoidal injection methods are shown in Table 6.1 and Table 6.2 with loading from 0 to 60A at -60rpm and -120rpm respectively.

iq(A)	Sensored (dBA)	Fixed HF d-axis sensorless (dBA)		Random HF d-axis sensorless (dBA)			
		1500 Hz	2000 Hz	1500± 328 Hz	1500± 656 Hz	2000± 328 Hz	2000± 656 Hz
0	51.2	52.3	59.4	52.5	52.6	59.2	59.6
20	51.8	53.9	60	53.1	54.2	59.8	60.1
40	53.4	55.5	60.9	54.3	55.5	59.7	60.2
60	54.6	56.6	61.2	55.6	56.8	60.7	61.5

Table 6.1: Audible noise measured at -60rpm

iq(A)	Sensored (dBA)	Fixed HF d-axis sensorless (dBA)		Random HF d-axis sensorless (dBA)			
		1500 Hz	2000 Hz	1500± 328 Hz	1500± 656 Hz	2000± 328 Hz	2000± 656 Hz
0	52	53.4	62.1	53.6	53.8	60.7	60.7
20	53.4	54.7	62.5	54.7	55	61.2	61.6
40	54.1	57.1	63.3	56.6	57.2	62.4	62.8
60	55.5	58.1	65.1	57.2	57.7	63.7	64.6

Table 6.2: Audible noise measured at -120rpm

It should be noted that the audible noise measurements did not include those for the 10 kHz square wave injection method since the injection frequency and its related noise are beyond the measurement bandwidth of the sound meter (up to 8 kHz [73]). Measurement with higher bandwidth instrument is needed for future evaluation.

From Table 6.1 and Table 6.2, one can find that with the increase of speed, the sound level also tends to increase, which is obvious since the air displacement due to rotation increases and the commutation of brushes of the DC load machine is increased. In addition, the sound level is increased with the increase of load. This can be explained as more vibration will be produced due to the increased torque ripple with heavier loads. For the sensorless operation, the increase of the estimation error with load also contributes to the increase of the torque ripple, which was explained earlier in this chapter. Hence, an increased

audible noise is expected.

For the fixed *hf* injection method with the same amplitude of the *hf* current (set to around 1 Amp as described in Chapter 3) the measured sound level increases when the injection frequency is increased from 1500 to 2000 Hz as expected. For the random *hf* injection method, the measured audible noise is reduced slightly. However, with the increase of random frequency range, the measured audible noise shows a slight increase, which could be possibly due to the combined effect of the machine structure and the A-weighting scales for quantifying the noise. For frequency range further away from 1.5 kHz and 2 kHz, the less the noise components are obtained after the weighting scaling.

6.3.2 Frequency analysis of the recorded noise

The sounds of the noise were recorded using the sound level meter microphone and were input to the PC and captured by the Microsoft Sound Recorder programme sampled at 48 kHz with 16-bit mono type data for 4 seconds. A Matlab programme was then used to perform the FFT analysis of the captured sounds. The results for a sensored benchmark, a 1500 Hz fixed *hf* sinusoidal injection sensorless operation, two random *hf* sinusoidal injection sensorless operations with frequency ranges of (1500±328) Hz and (1500±656) Hz, and a 10 kHz square wave *hf* injection sensorless operation are shown from Figure 6.7 to Figure 6.11, with the motor running at -60rpm under 20A load.

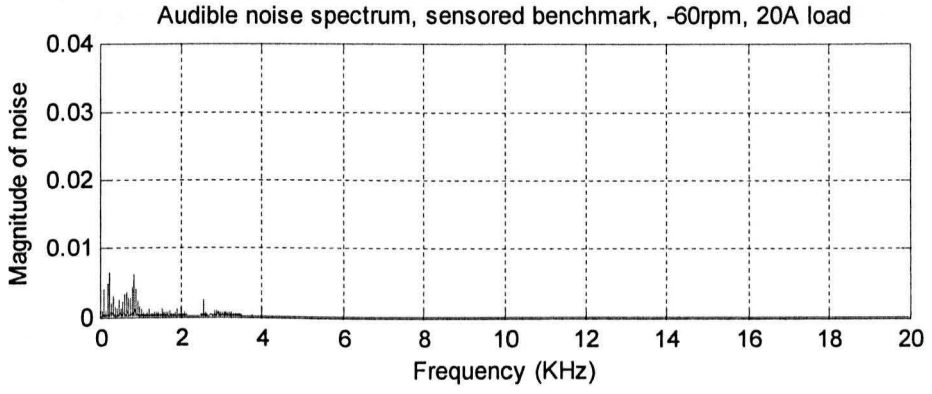

Figure 6.7: Audible noise spectrum of the sensored benchmark running at -60rpm under 20A load

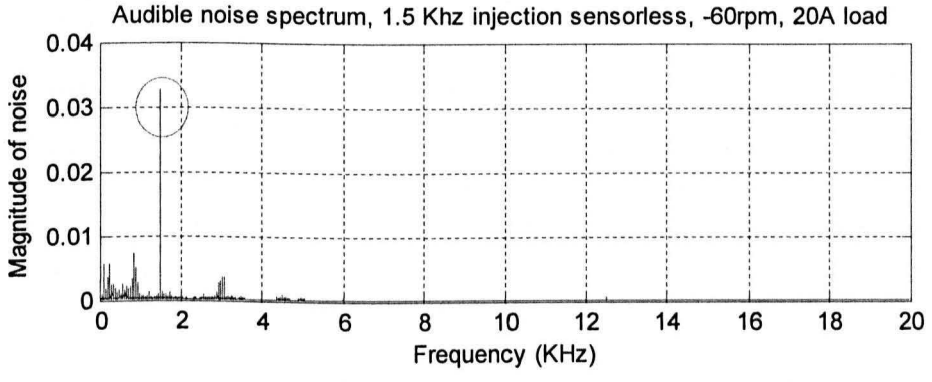

Figure 6.8: Audible noise spectrum for the 1.5 kHz fixed injection sensorless operation running at -60rpm under 20A load

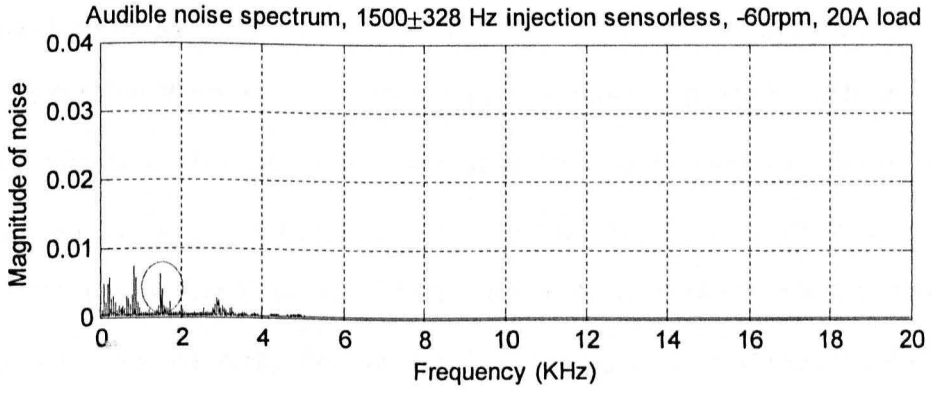

Figure 6.9: Audible noise spectrum for the (1500±328) Hz random injection sensorless operation running at -60rpm under 20A load

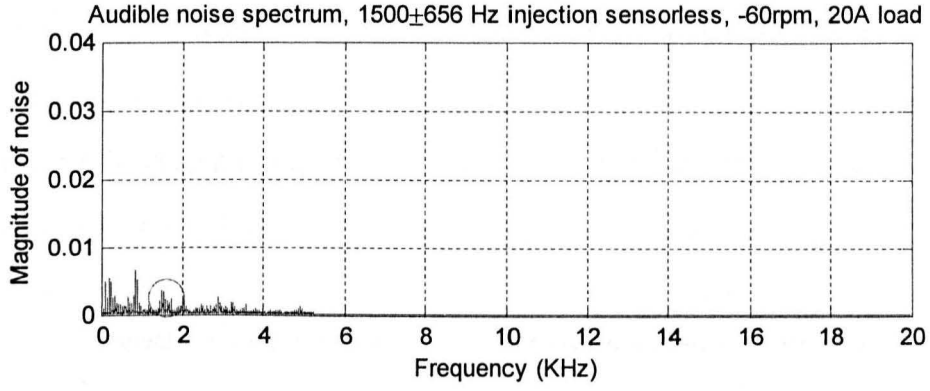

Figure 6.10: Audible noise spectrum for the (1500±656) Hz random injection sensorless operation running at -60rpm under 20A load

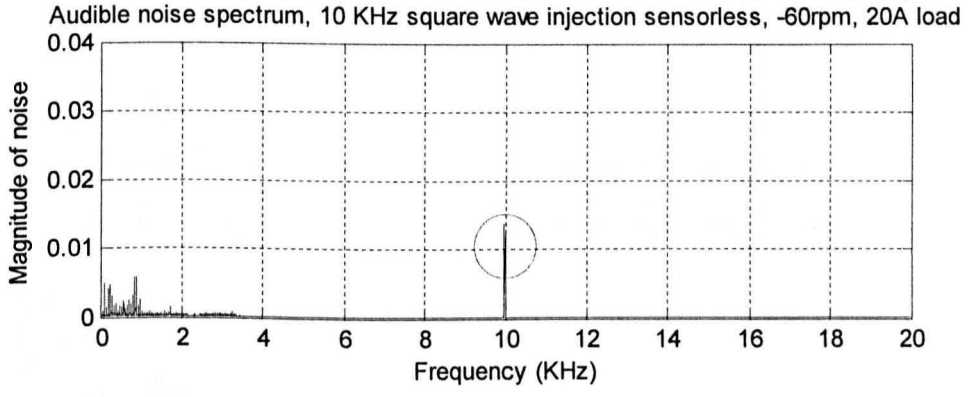

Figure 6.11: Audible noise spectrum for the 10 kHz square wave injection sensorless operation running at -60rpm under 20A load

From the spectra of the recorded noise for the different control operations, it can be found that there exists an identical low frequency noise band from 0 Hz to approximately 880 Hz, which originates from the vibrations due to various reasons including the DC brushes commutation, air displacement while rotating, etc. By comparing Figure 6.7 to Figure 6.10, it is obviously that the noise frequency related to the injection tends to spread wider and the magnitude gets flatter significantly, as marked by the red circles, which will result in a better hearing experience. However, as can be noted from Figure 6.10, some noise around 5 kHz is produced, which is an agreement with the previous finding that with a wider random frequency range (e.g. from 1500±328 Hz to 1500±656 Hz

in this case), the audible noise gets louder. This additional noise is more likely due to the machine construction rather than the injected high frequency current, as can be illustrated in Figure 6.12, since no noticeable current around 5 kHz is observed for the (1500±656) Hz random injection operation.

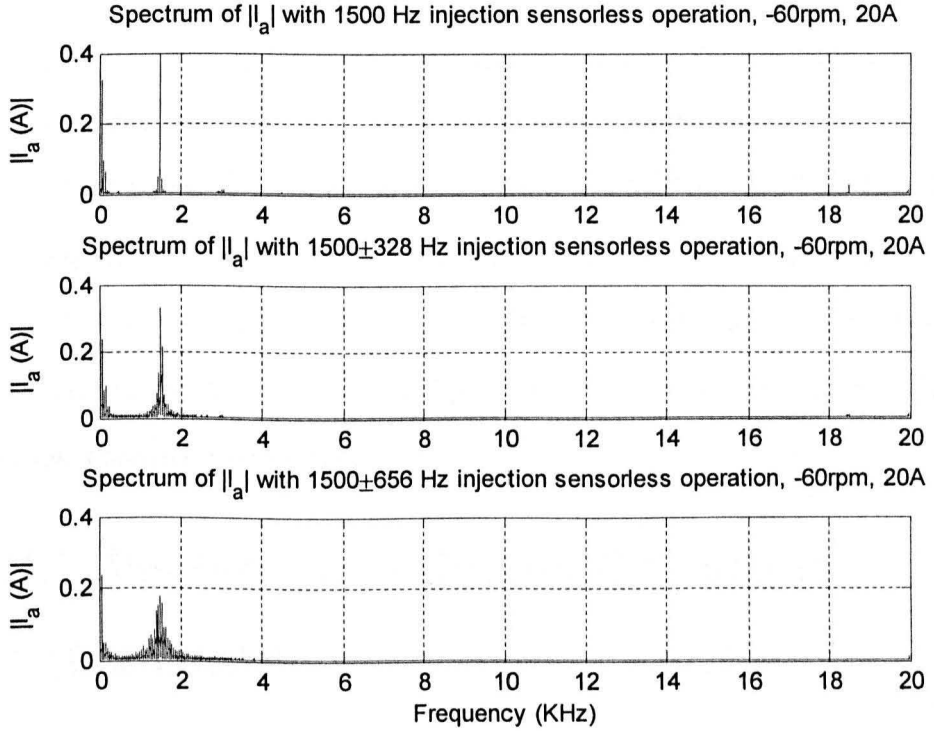

Figure 6.12: Zoomed spectra of the line currents for sensorless operations with 1500 Hz fixed injection, (1500±328) Hz random injection, and (1500±656) Hz random injection at -60rpm, 20A

The noise spectrum for the 10 kHz square wave injection sensorless operation, as shown in Figure 6.11, manifests similar distribution as that of the sensored benchmark, shown in Figure 6.7, despite for the sidebands around 10 kHz. With a proper sound level meter it is expected to give a rather low noise measurement since sounds around 10 kHz attenuate greatly after A-weighting. It is also noted that the magnitude of the noise components around 10 kHz is less than for the fixed *hf* sinusoidal injection methods since it has a lower injection current (about 0.5 A, which is approximately half of value for the sinusoidal injection methods)

is produced due to the limit of the voltage output from the inverter. Inevitably, this will give a reduced SNR (signal to noise ratio) and hence poorer estimation quality.

6.4 Dynamic performance

In order to provide the fast assistant torque response for the EPS system, the designed dynamics of the sensorless control needs to be fast, which is determined by the bandwidth of the tracking mechanism. A 90 Hz Luenberger observer was chosen in this research for all of the sensorless methods being adopted here and was described in Chapter 4. The dynamic performances of them were tested and the results are presented in this section in terms of torque transients and speed transients.

6.4.1 Performance during the torque transients

In the EPS applications, a fast torque response is required especially at the starting stage of the vehicles. The performance during the torque transients was tested when the motor was controlled at -60rpm (mechanical) steady speed. It is noted that all of the positions plotted in the figures in this section are electrical positions and the estimation errors are electrical position errors as well.

A step torque of 50A (56%) was demanded whilst operating with the 1.5 kHz and 2 kHz fixed injection methods, and for (1500 ± 328) Hz and (2000 ± 328) Hz random injection methods, as shown from Figure 6.13 to Figure 6.16. By comparing the results for the random injection methods to their fixed injection versions with the same centre frequencies, identical transient performances can be observed. For all the mentioned sensorless operations, at the instant when a step torque was demanded, a glitch in the estimated position appeared due to the

sudden change of torque which can be regarded as a disturbance with its frequency much larger than the bandwidth of the estimation tracking mechanism. A large overshoot of speed followed partly due to the low inertia of the drive system, and a better speed controller is expected to be designed in the future to overcome it. For a real EPS system, as the inertia is much larger than in the test rig, this large overshoot will not exist, which means a smoother speed response is expected. An electrical position error oscillation ranging from approximately -30 degrees to 5 degrees was then observed during the rest of the transient interval. It can be seen that the *d* and *q* axis currents are controlled accurately and correctly.

For the fixed frequency injection and for the (1500 ± 328) Hz and (2000 ± 328) Hz random injection, the transient operation is able to control a step change of 50A (56%) in torque current demand correctly. However for the (1500±656) Hz and (2000±656) Hz random injection sensorless methods, a step of 50A (56%) torque would result in failure in estimation, since the band pass filters used for extraction of the *hf* current components are of wider bandwidth compared to the fixed frequency injection methods (2^{nd} order band pass filters with 200 Hz bandwidth) and ±328 Hz random injection methods (4^{th} order bandpass filters with 660 Hz bandwidth), higher order of the filter is therefore needed to filter out the noise and other unwanted disturbances especially when loading, which inevitably introduces more delays and hence poorer dynamics. The band pass filters chosen for the (1500±656) Hz and (2000±656) Hz random injection methods are 6^{th} order butterworth type filters with 1320 Hz bandwidth. A torque step of 40A (44%) was demanded for both of the methods instead, with the results shown in Figure 6.17 and Figure 6.18. Similar transient performances can be found as expected.

For the 10 kHz square wave injection sensorless method, the step change of

torque demand was set also at 40A (44%). With 50A (56%) step torque demand, the control would fail as well, probably due to the lower SNR compared to the other methods, as mentioned ealier. The result for the 40A (44%) transient is shown in Figure 6.19 with similar performance in transient interval as for other methods.

In addition, it is found from Figure 6.17 to Figure 6.19 that with the 40A (44%) step change in torque current demand, the resultant position estimate shows much less position error once the transient has settled compared to that with 50A (56%) change in torque current demand as shown from Figure 6.13 to Figure 6.16. This is because the position estimate has been highly distorted by higher order saliencies when load increases.

For all the aforementioned methods, it is noted that the measured i_q contains much less distortion than i_d. This is because the most of the hf current is injected into the *d-axis* and the torque producing *q-axis* remains unchanged if a correct estimation has been achieved.

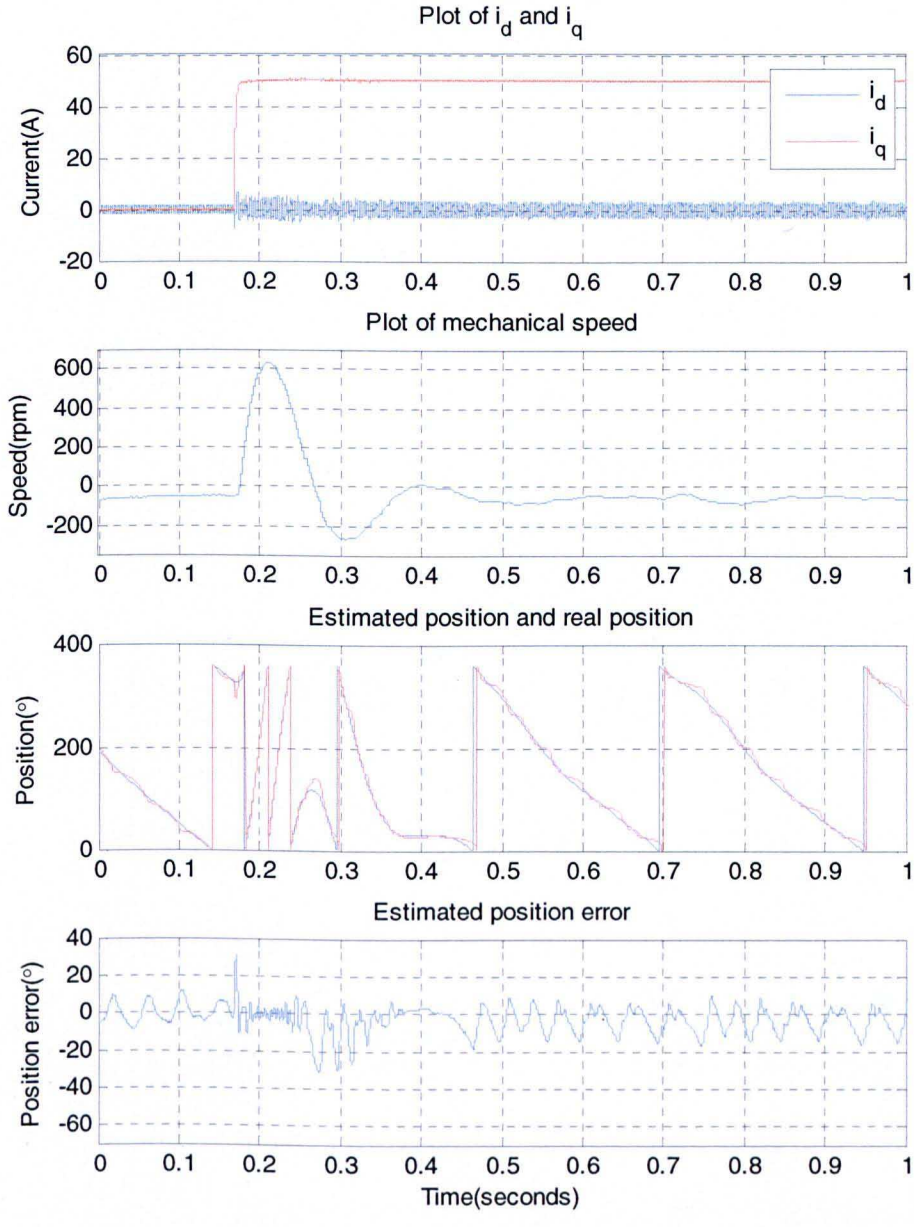

Figure 6.13: Torque transient, 0-50A (56%), 1.5 kHz fixed injection at -60rpm

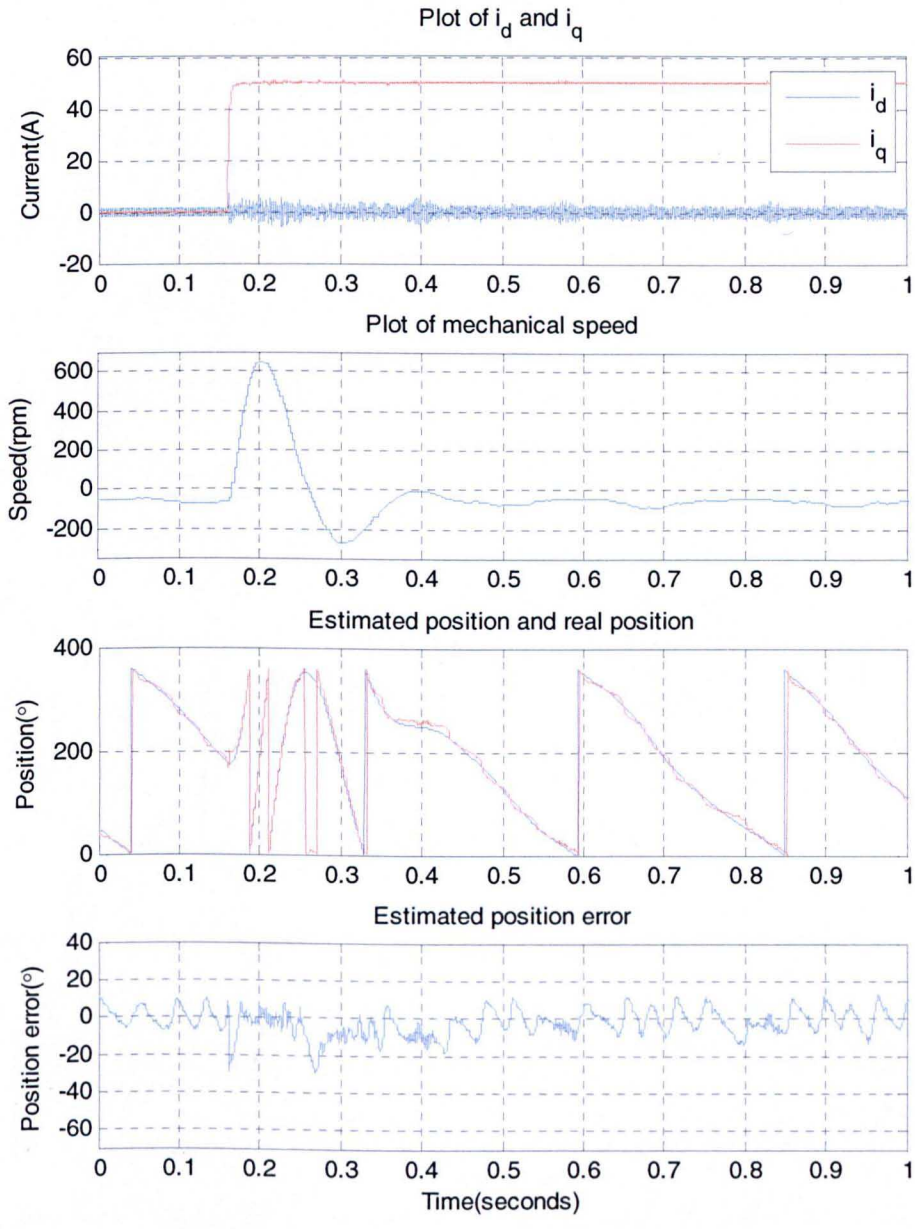

Figure 6.14: Torque transient, 0-50A (56%), (1500 ± 328) Hz random injection at -60rpm

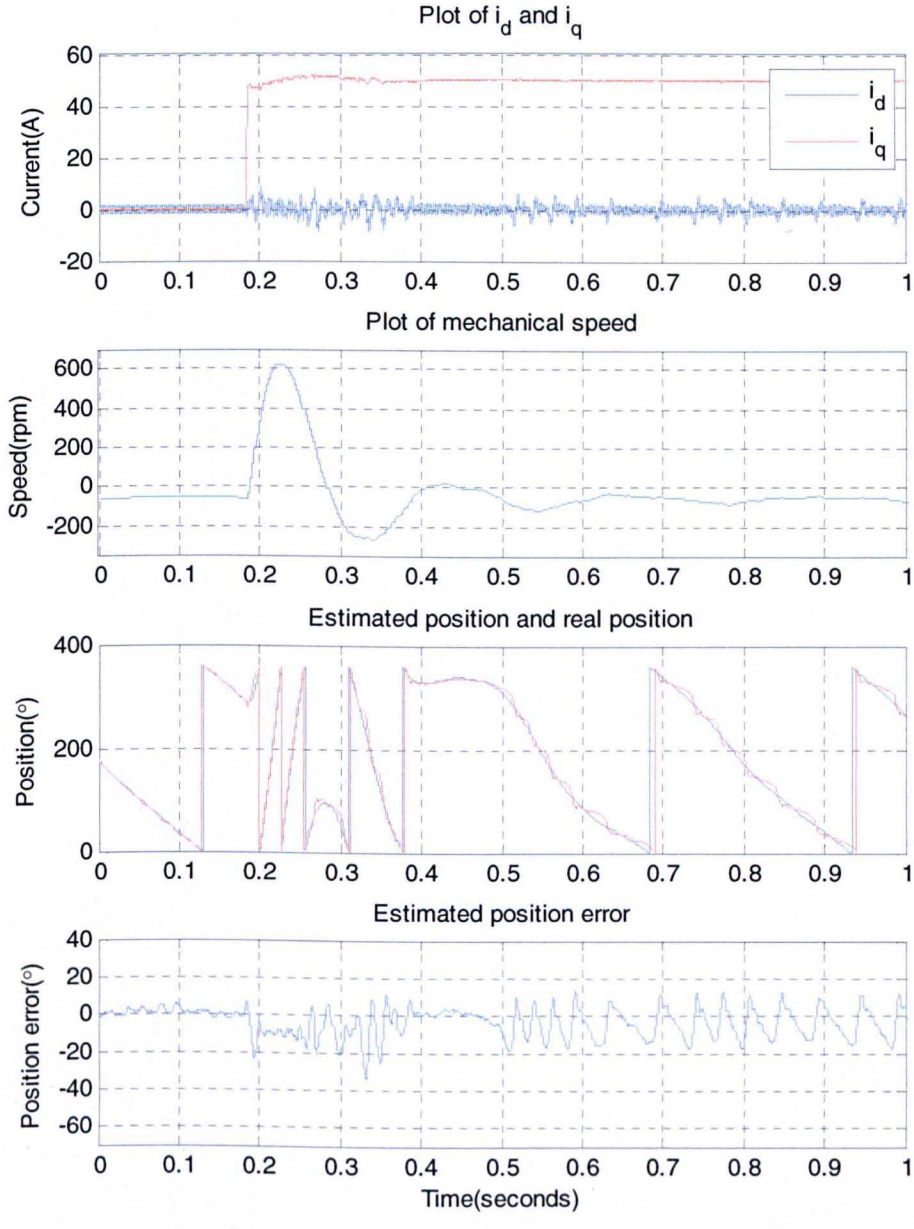

Figure 6.15: Torque transient, 0-50A (56%), 2 kHz fixed injection at -60rpm

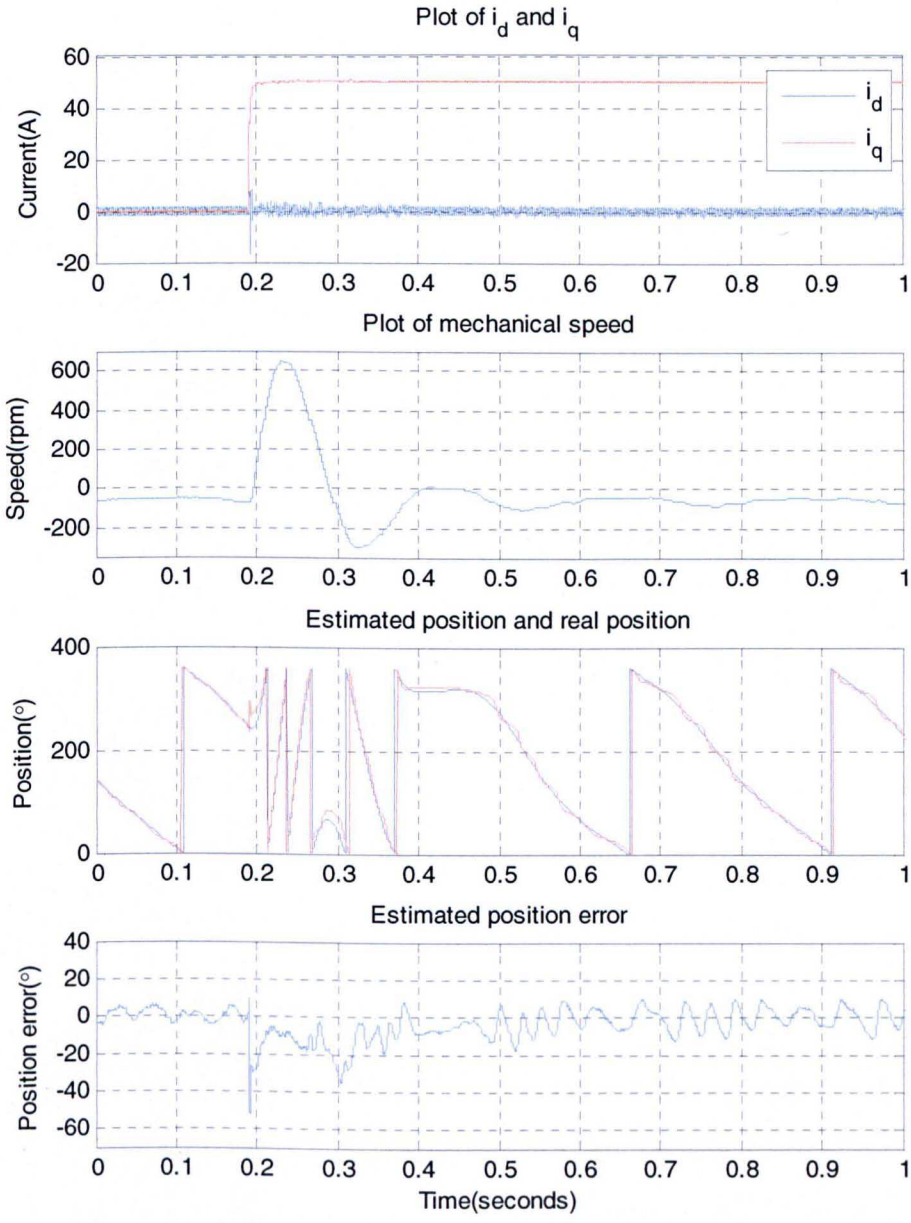

Figure 6.16: Torque transient, 0-50A (56%), (2000 ± 328) Hz random injection at -60rpm

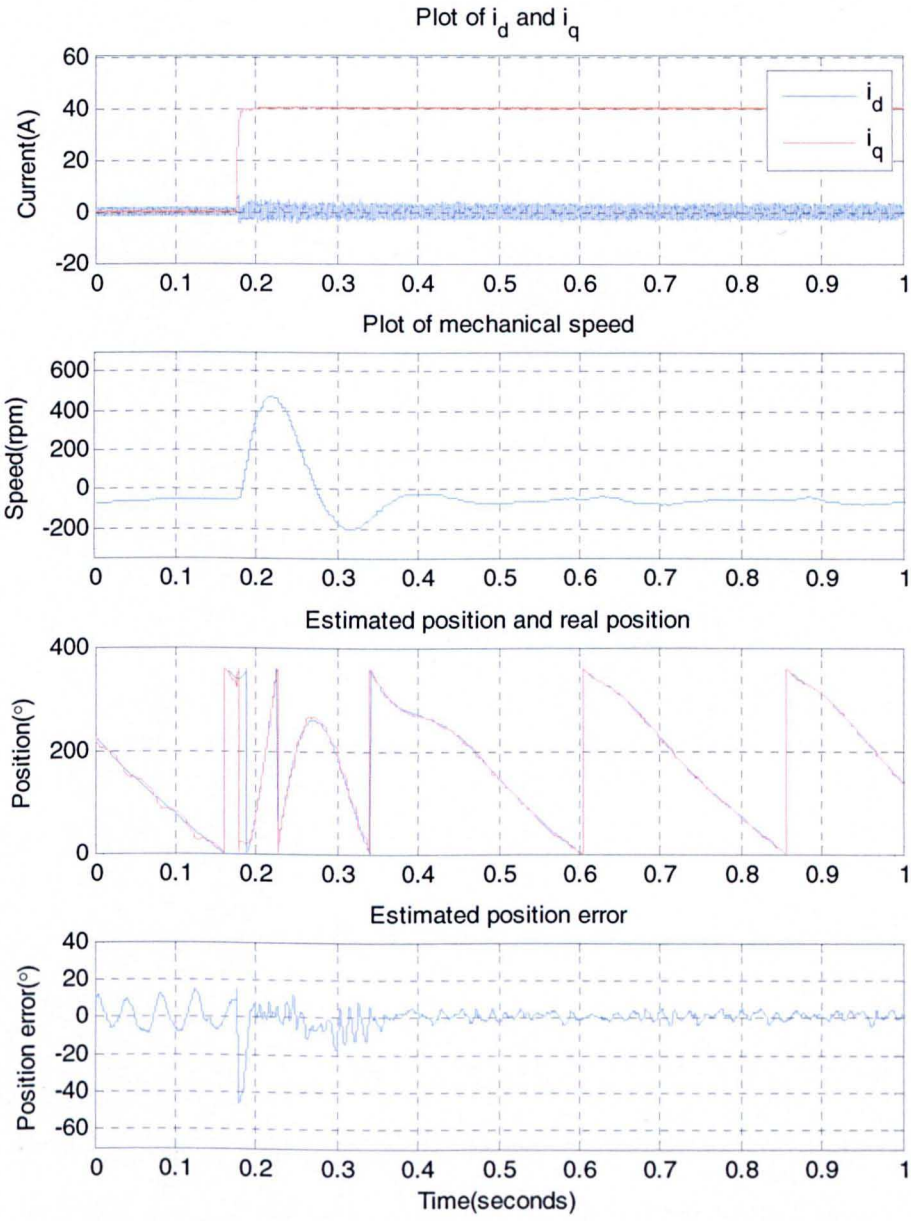

Figure 6.17: Torque transient, 0-40A (44%), (1500 ± 656) Hz random injection at -60 rpm

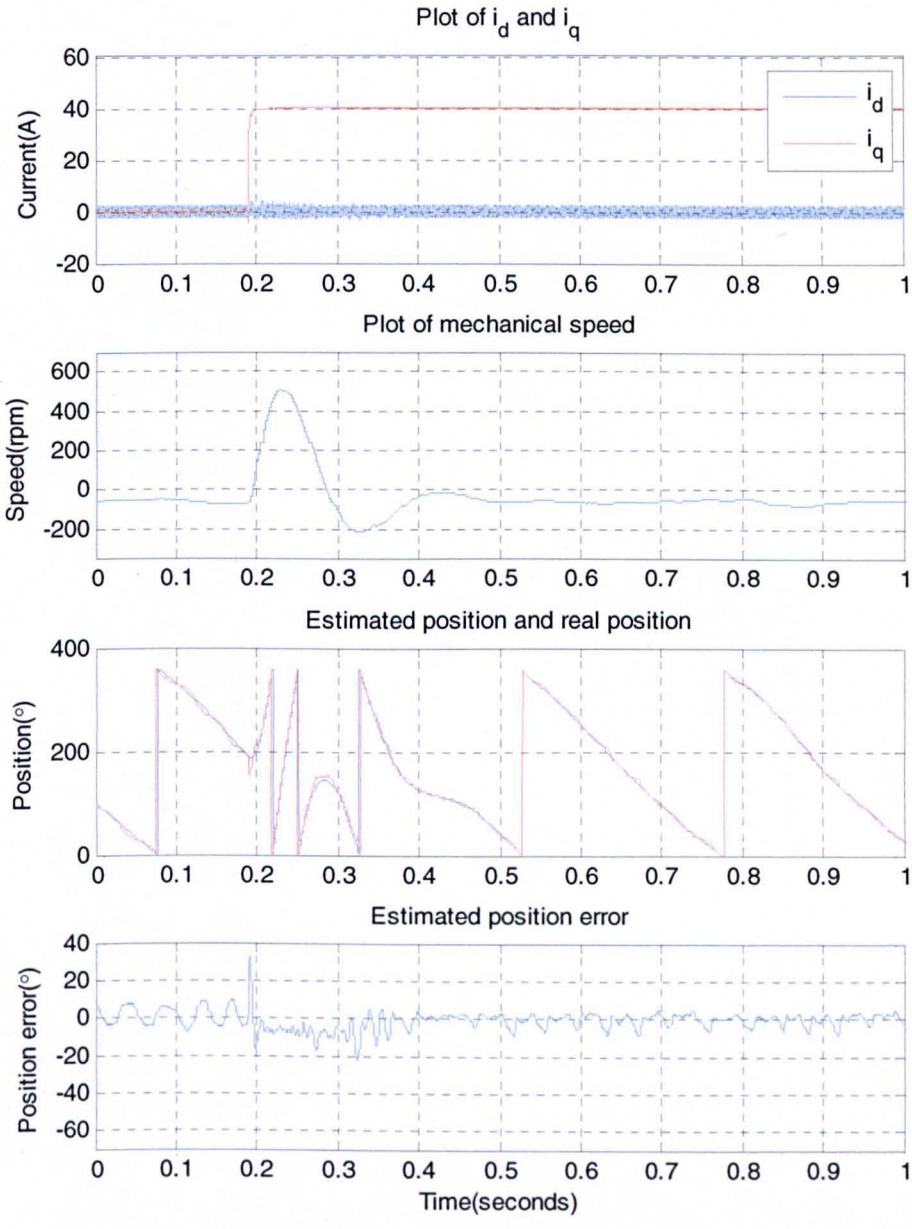

Figure 6.18: Torque transient, 0-40A (44%), (2000 ± 656) Hz random injection at -60 rpm

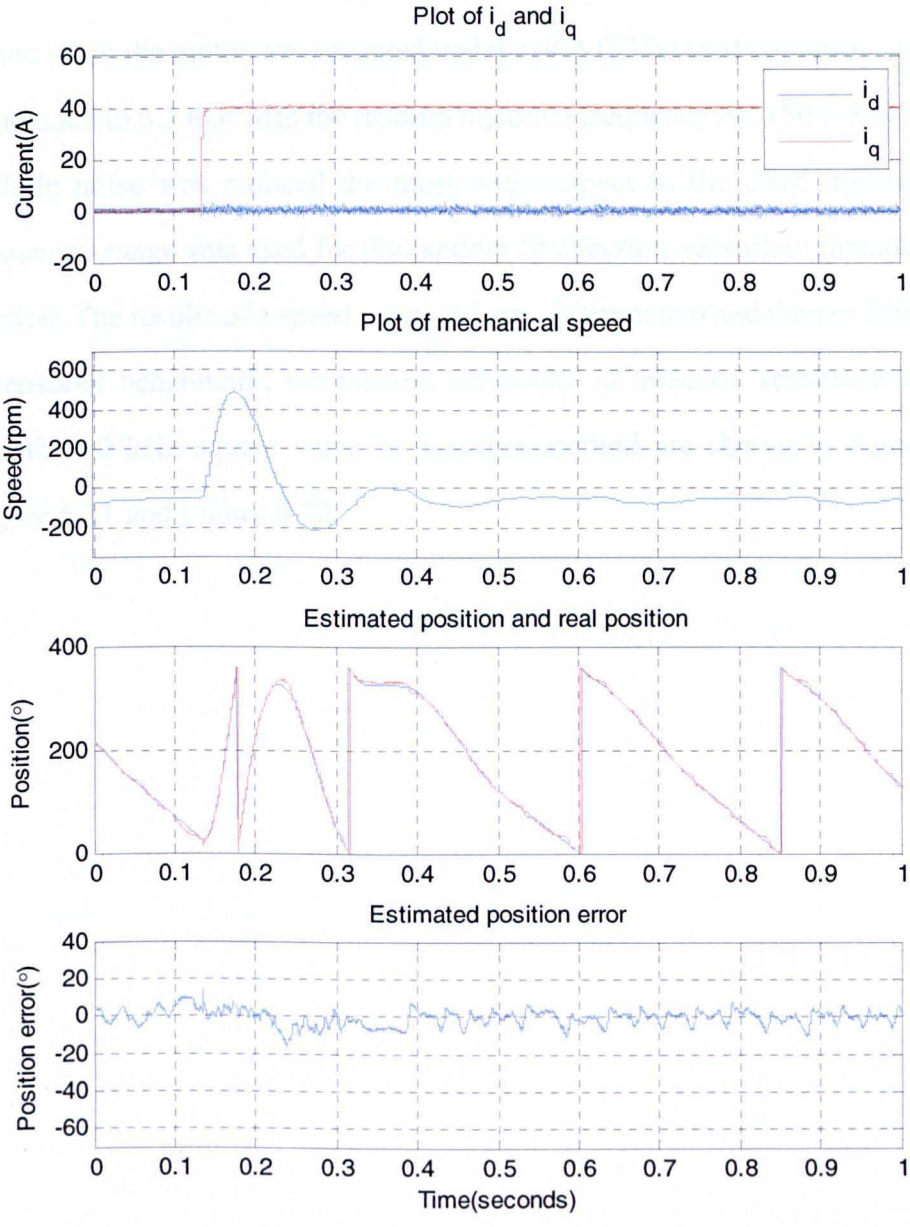

Figure 6.19: Torque transient, 0-40A (44%), 10 kHz square wave injection at -60rpm

6.4.2 Performance during speed transients

The response of the sensorless scheme to a speed change is also very important for EPS applications. For example, when drivers are parking their vehicles, fast speed steps of the EPS motors may occur as the drivers rotating the wheel quickly. It is essential to maintain accurate tracking of the position in order to

give the correct assistant torque. The performance during speed transients was tested when the motor was operated under a 30A (33%) load condition. As it was concluded in 6.3 that with the random injection frequency of (1500±328) Hz, the audible noise was reduced the most with respect to the fixed injection, this frequency range was used for the random *hf* injection sensorless method in this section. The results of a speed reversal from -240rpm to 0 and then to 240rpm for a sensored benchmark, the random sinusoidal *hf* injection sensorless method, and the 10 kHz square wave *hf* injection method are shown in Figure 6.20, Figure 6.21 and Figure 6.22.

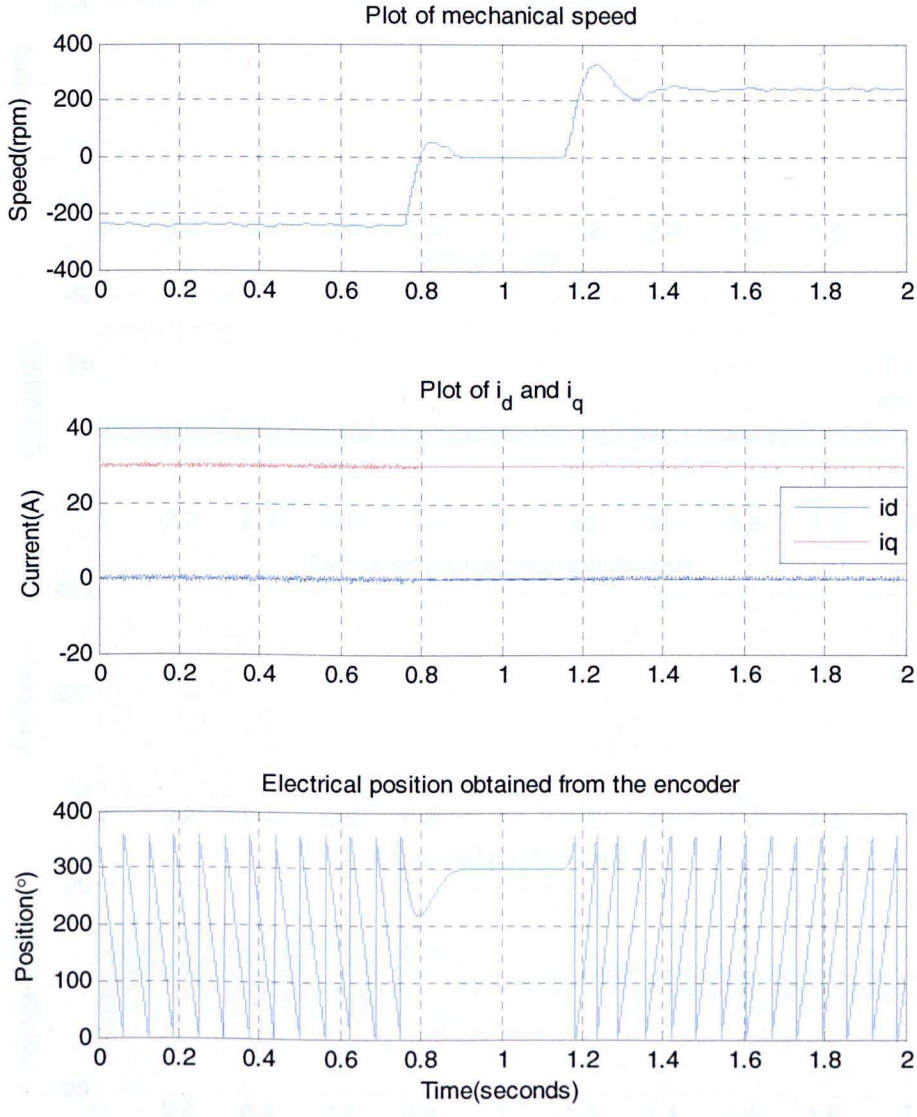

Figure 6.20: Speed reversal, -240rpm-0-240rpm, sensored benchmark under 30A (33%) load condition

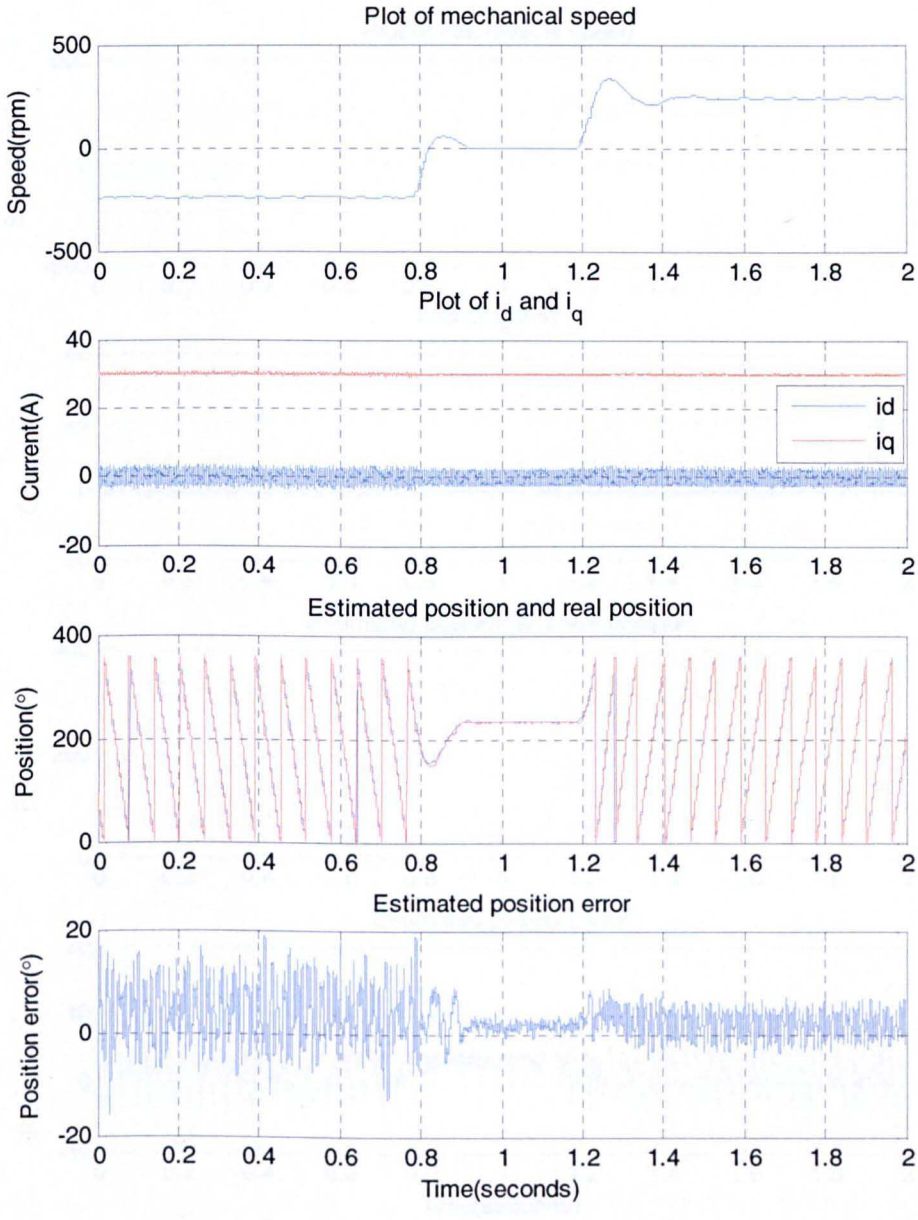

Figure 6.21: Speed reversal, -240rpm-0-240rpm, (1500±328) Hz random sinusoidal *hf* injection sensorless operation under 30A (33%) load condition

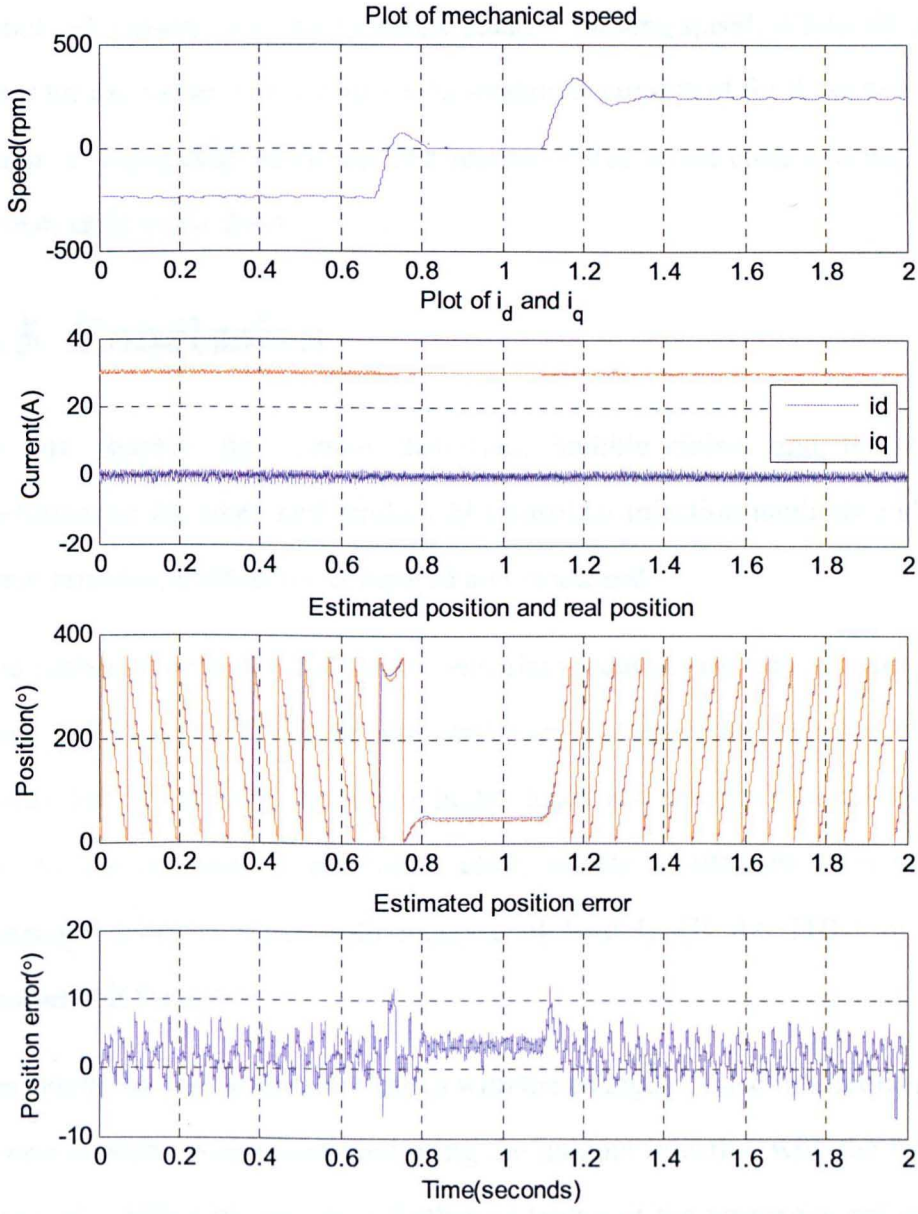

Figure 6.22: Speed reversal, -240rpm-0-240rpm, 10 kHz square wave *hf* injection sensorless operation under 30A (33%) load condition

As observed from Figure 6.20 to Figure 6.22, both the random sinusoidal *hf* injection and the square wave *hf* injection methods are able to track the position during the speed reversal and provide comparable assistant torque to the sensored benchmark. The average position error is however bigger for the random *hf* injection method, presented as uneven position error for positive and

negative speeds: about ±15° (electrical position) for the negative speed and about ±5° (electrical position) for the positive rotating speed. Whilst the position error for the square wave *hf* injection method is consistent for these two speeds: about ±5° (electrical position). The reason of this is not clear and needs to be investigated in the future.

6.5 Conclusion

In this chapter, the current distortion, audible noise, and the dynamic performance for fixed and random *hf* sinusoidal injection methods and square wave injection method are compared and discussed.

The current distortion for different sensorless methods are very similar with the same SNR (i.e. the *hf* current amplitudes are the same) for the same operating points. For this specific test motor, higher loads will cause additional distortions due to the increase of estimation error, which is different from the work presented in [13] where with increase of load levels the THDs of current decrease all the time.

Audible noise due to injection varies with the change of injection frequency. The lowest audible noise is obtained using the random injection with the frequency range of (1500±328) Hz. With further widening of the frequency ranges, some additional noise will occur in the around 5 kHz area, possibly due to motor construction and a resonant point being reached. For the 10 kHz square wave injection sensorless method, the audible noise level cannot be obtained properly due to the limitation of the instrumentation, and it requires a higher DC link voltage to give the same *hf* current levels in order to compare with the sinusoidal injection methods.

The dynamic performance of all the aforementioned sensorless methods is compared. The best is shown with fixed injection and with the random injection

of frequency range within ±328 Hz due to the band pass filter delay which affects the system dynamics. The square wave injection method has similar performance with ±656 Hz random injection methods due to the low SNR value.

Chapter 7 Conclusions and Future work

7.1 Introduction

This thesis has focused on the reduction of audible noise in sensorless controlled drives for automotive electrical power steering applications which use saliency tracking methods and in particular the *hf* injection methods. Three methods have been implemented, the fixed and random *hf* injection methods and the square wave *hf* injection method. The audible noise introduced by the *hf* injection and also the control performance of the three methods have been compared and contrasted.

The novel work presented in this thesis includes:

- Research and development of a novel random *hf* injection based sensorless control
- Research and implementation of a square wave type injection for sensorless control for power steering applications
- A comparison of the behaviour of the two techniques for power steering applications

7.2 Audible noise reduction

The audible noise created by *hf* injection sensorless control is mainly caused by the *hf* voltage injection itself. In the test rig, the chosen injection frequencies 1.5 kHz and 2 kHz for the fixed *hf* sinusoidal injection method create significant audible noise. The frequency of the induced noise is near the injection frequency and is perceived as a fixed tone. In an EPS system, the motor as well as its control unit is designed to be close to the driver. The audible noise produced by the fixed *hf* sinusoidal injection is not acceptable as it will cause passenger discomfort. The random *hf* sinusoidal injection method uses a randomised *hf* voltage injection to the machine. The resultant audible noise is a random spread of frequencies around the centre frequency and is perceived as a background hiss rather than a fixed tone. Frequency ranges of (1500±328) Hz, (1500±656) Hz, (2000±328) Hz and (2000±656) Hz have been compared. By analysing the A-weighting scales used to classify human perception of audible noise, the injection with a frequency of (1500±656) Hz was expected to have the lowest sound level. However, it was found that an injection frequency of (1500±328) Hz exhibits the lowest audible noise level, from direct measurement with a sound level meter. Frequency analysis of the recorded noise showed that some noise around 5 kHz is produced with (1500±656) Hz injection due to the resonance of the mechanical structure of the machine, which caused a higher sound level measurement compared to the (1500±328) Hz injection. The sound level measurement for the 10 kHz square wave *hf* injection has not been taken since the sound level meter used in this test rig has an upper frequency limit of 8 kHz. However, the frequency analysis of the recorded noise for this method was carried out for comparison. It was found that the noise introduced by the *hf* injection is around 10 kHz and creates no other noise in the low frequency region. It should in theory have a lower sound level than the fixed *hf* sinusoidal injection

at 1.5 kHz and 2 kHz. By using either of these two methods, the audible noise can be effectively reduced.

7.3 Control performance

Sensorless torque control with the three *hf* injection methods has been achieved from zero speed to ±240rpm with up to ±60A load (about 63% rated load). Similar position estimate quality for the three *hf* injection sensorless methods has been demonstrated. It was found that under no load conditions, the position estimate has been distorted significantly due to the non-linear behaviour of the inverter around zero current crossing points and manifests as a $6f_e$ disturbance. When load increases, the resultant *hf* current signals that contain the position information have fewer zero current crossing points compared to that under no load, and hence a lower distortion was observed. However, with the load between 30A and 60A, the distortion of the position estimate increased again. This is because the tracked saliency was affected by the higher order saliencies when the load increases. When the load increases, sensorless control could not be achieved since instability of control occurs due to these higher order saliencies.

The current distortion of the drive system caused by *hf* voltage injection is similar for the fixed and random *hf* sinusoidal injection sensorless control. The injection frequency also does not affect the current distortion significantly. The 10 kHz *hf* square wave injection sensorless control has smaller current distortion than that for the other two methods, since the resultant *hf* current for the square wave injection is much less due to the limitation of the inverter output when a 12V DC-link voltage is used. Under load levels less than 30A, the sensored control with *hf* injection and sensorless control result in identical current distortion. However, above 30A the position estimation is affected by the higher

order saliencies and additional torque ripple is produced resulting in more distorted current.

Fast torque response is required for automotive power steering applications. Torque transients for the three sensorless methods have been performed to test the dynamic performance. It was found with both the fixed and random *hf* sinusoidal injection methods, when a 50A torque transient was applied, the position estimate still tracked the real position with a maximum ±25 degrees error during the transient intervals. However, with the 10 kHz *hf* square wave injection method, the largest torque transient that can be applied is 40A. This is because the method has a lower SNR compared to that for the *hf* sinusoidal injection. This is due to the limit of the inverter output voltage and affects the saliency tracking in a high torque transient. Dynamic response for the speed transient has also been performed for random sinusoidal *hf* injection and square wave *hf* injection sensorless methods. Comparable results have been demonstrated with a sensored control result as the benchmark for analysis.

7.4 Summary of Project Achievements and and Future Work

Refering to the aims and objectives set in Chapter 1, the following goals have been achieved:

- Audible noise reduced compared to a traditional fixed injection type sensorless method
- Low speed sensorless torque control from 0-240 rpm
- Angle error below 10 electrical degrees under 40A (44%) load conditions
- Up to 60A (67%) load sensorless operation

- Large torque transient, up to 50A (56% load) step change

Future work on the following aspects needs to be carried out:

- To investigate the relationship between the machine structure and the minimum audible noise with respect to the applied injection frequency in order to further optimise the random injection method
- To investigate possibility of rearranging the PWM sequence to apply a square wave at the switching frequency to further improve the square wave injection method
- To extend the low speed sensorless operation to full load (90A)
- Combining model based sensorless operation at high speed to achieve full speed region sensorless torque control
- To investigate the method for reducing the ripple of the angle error at higher loading conditions (especially above 40 A, 44% load) by compensating for the loading effects and inverter non-linearities.

Appendix A Phase currents reconstruction through DC link current measurement

For a general 3-phase balanced PMAC drive system as shown in Figure A.1, when different voltage vectors are applied to the machine, the DC link current can be split as combinations of different phase currents, as shown in Table A.1.

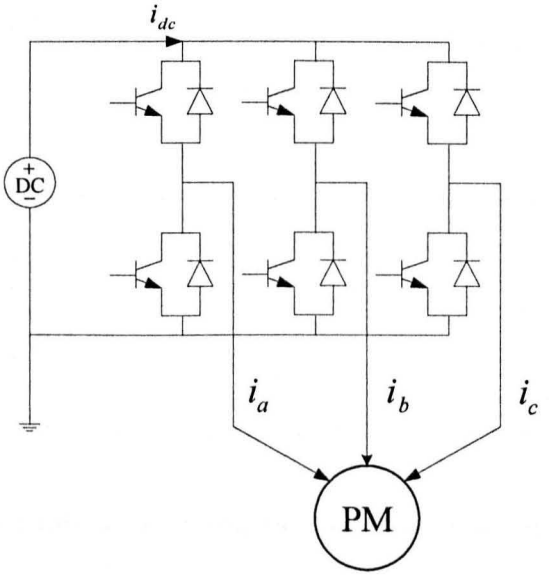

Figure A.1: A general 3-phase PMAC drive system

Voltage Vector	DC link current
100 (V1)	i_a
110 (V2)	$(i_a + i_b) = -i_c$
010 (V3)	i_b
011 (V4)	$(i_b + i_c) = -i_a$
001 (V5)	i_c
101 (V6)	$(i_a + i_c) = -i_b$
000/111 (V0/V7)	0

Table A.1: DC link current values during each of the vectors

As a result, it is possible to work out the phase currents by measuring the DC link current when corresponded vectors are applied. For example, when the demanded voltage vector is within sector I, as shown in Figure A.2, it can be decomposed of active vectors V1 and V2. With high switching frequency implemented, the interval between the two DC link current samples for the two active vectors is sufficiently small and the measured phase currents can be assumed to be sampled at a same instant, and then the third phase current can be calculated due to the balance property of the drive system.

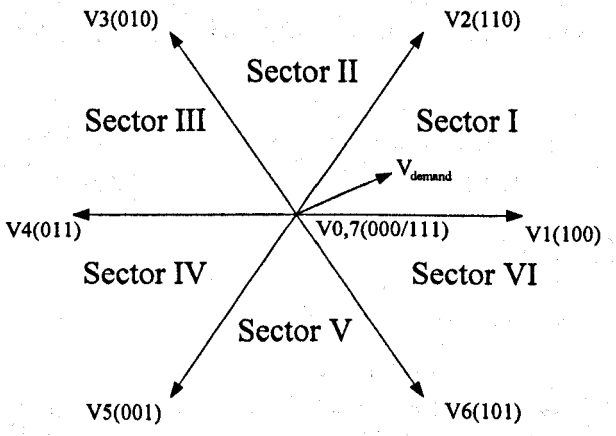

Figure A.2: Vector diagram when the demanded voltage resides in Sector I

However, due to the dead time, the diode reverse-recovery and the ADC acquisition delay, a minimum time of T_{min} is required for an accurate current sample after an active vector is applied. This will cause problems when the demanded vector passes through the boundaries of the adjacent sectors and when the demanded vector is below certain threshold, where in both cases, the durations of one or more of the active vectors in a switching period will be shorter than T_{min}. As a result, pulse extension is applied in these situations. For example, when the demanded vector is very low in Sector I, both of the active vectors (V1 and V2) need to be extended and the additional active vectors need to be compensated by applying opposite vectors (V4 and V5) to keep the volt-second balanced, as illustrated in Figure A.3. For the implementation, the extension of the active vectors could be done within the first half of the switching period, and the compensation could be made during the second half of the period. Other arrangements of allocating the extension and compensation could also be used to optimize the performance with respect to computation efforts and the cost reduction. For instance, in order to reduce the sample rate, the current measurements could be made with several adjacent switching periods, especially at low speed where the vector almost remains the same during the adjacent switching periods. By doing so, the extension is also needed only when

relevant measurement needs to be made, resulting in reduced torque ripple as well.

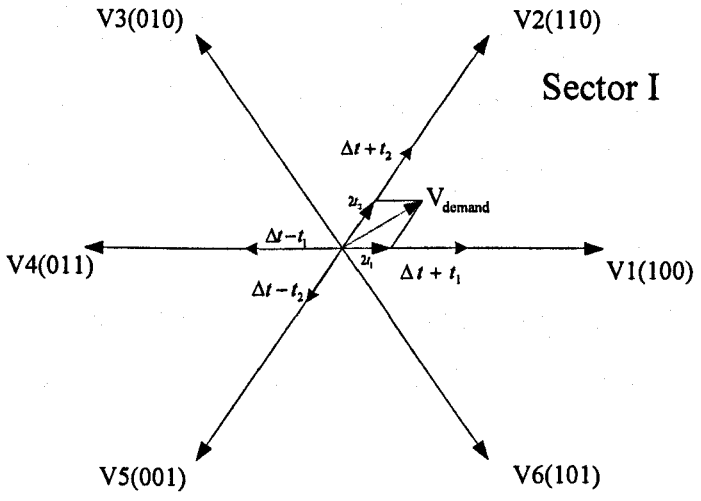

Figure A.3: Vector extension and compensation when V_{demand} is small in Sector I

Appendix B The schematic of the gate drive circuit

The schematic of the gate drive circuit is shown in Figure B.1.

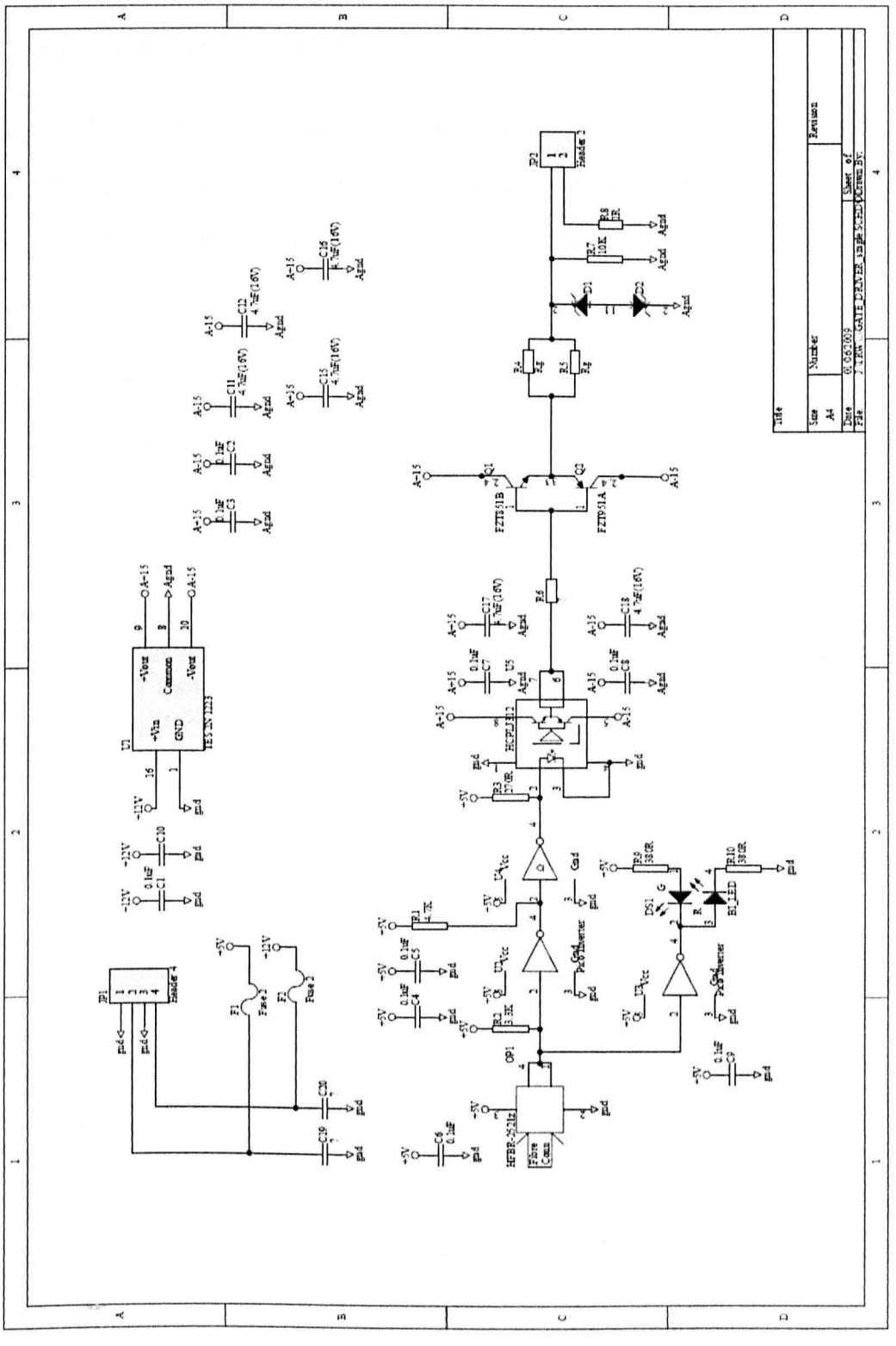

Figure B.1: Schematic of the gate drive circuit

Appendix C Publications

1. Hui J., Sumner M.: *Sensorless torque control of PM motor using modified HF injection method for audible noise reduction*, 14th European Conference on Power Electronics and Applications, Birmingham, 2011

References

1. Nunney, M.J., *Light and Heavy Vehicle Technology*. Fourth Edition ed. 2006: Butterworth-Heinemann.
2. TRW, *EPHS--Electrically Powered Hydraulic Steering*. 2011.
3. TRW, *Electrically powered steering - column drive*. 2008.
4. T.Sebastian, M.S.I., and S.Mir, *Application of permanent magnet synchronous machines in automotive steering systems.* Electrical Machinery and Energy Conversion Systems, KIEE International Transactions on, 2005. **5B**(2): p. 111-117.
5. Christopher, E., et al. *Power boost unit for automotive Electric Power Steering systems.* in *Power Electronics, Machines and Drives (PEMD 2010), 5th IET International Conference on*. 2010.
6. Aihara, T., et al., *Sensorless torque control of salient-pole synchronous motor at zero-speed operation.* Power Electronics, IEEE Transactions on, 1999. **14**(1): p. 202-208.
7. Andreescu, G.D., *Robust sliding mode based observer for sensorless control of permanent magnet synchronous motor drives*, in *PEMC conference*. 1998. p. 172-177.
8. Andreescu, G.D., *Position and speed sensorless control of pmsm drives based on adaptive observer*, in *EPE*. 1999.
9. Ben-Brahim, L., *Motor speed identification via neural networks.* Industry Applications Magazine, IEEE, 1995. **1**(1): p. 28-32.
10. C.M. Bingham, B.S.B., *Nonlinear state-observer techniques for sensorless control of automotive pmsm's, including load-torque estimation and saliency*, in *EPE Conference*. 2003.
11. Chan-Hee, C. and S. Jul-Ki, *Pulsating Signal Injection-Based Axis Switching Sensorless Control of Surface-Mounted Permanent-Magnet Motors for Minimal Zero-Current Clamping Effects.* Industry Applications, IEEE Transactions on, 2008. **44**(6): p. 1741-1748.
12. Corley, M.J. and R.D. Lorenz, *Rotor position and velocity estimation for a salient-pole permanent magnet synchronous machine at standstill and high speeds.* Industry Applications, IEEE Transactions on, 1998. **34**(4): p. 784-789.
13. Curson, A., *Low Speed Encoderless Control of Permanent Magnet AC Machines for Automotive Applications*, in *Electrical and Electronics Engineering*. 2009, University of Nottingham.
14. E. Robeischl, M.S., and K. Salutt. *Improved INFORM measurement sequence and evaluation for sensorless permanent magnet synchronous motor drives.* in *10th International Power Electronics and Motion Control Conference*. 2002.
15. Holtz, J. *Initial Rotor Polarity Detection and Sensorless Control of PM*

Synchronous Machines. in *Industry Applications Conference, 2006. 41st IAS Annual Meeting. Conference Record of the 2006 IEEE*. 2006.

16. Ji-Hoon, J., H. Jung-Ik, and S. Seung-Ki. *Vector control of surface mounted permanent magnet motor without any rotational transducer*. in *Applied Power Electronics Conference and Exposition, 2001. APEC 2001. Sixteenth Annual IEEE*. 2001.
17. Gao, Q., et al. *Position Estimation of AC Machines at all Frequencies using only Space Vector PWM based Excitation*. in *Power Electronics, Machines and Drives, 2006. The 3rd IET International Conference on*. 2006.
18. Raute, R., et al. *Operation of a sensorless PMSM drive without additional test signal injection*. in *Power Electronics, Machines and Drives, 2008. PEMD 2008. 4th IET Conference on*. 2008.
19. Silva, C.A., *Sensorless Vector Control of Surface Mounted Permanent Magnet Machines Without Restriction of Zero Frequency*, in *Electrical and Electronics Engineering*. 2003, University of Nottingham.
20. Yahan, H., et al. *Sensorless Control of Surface Mounted Permanent Magnetic Machine Using the Standard Space Vector PWN*. in *Industry Applications Conference, 2007. 42nd IAS Annual Meeting. Conference Record of the 2007 IEEE*. 2007.
21. Curson, A. and M. Sumner. *A comparison of low speed sensorless control techniques for low voltage PM machines*. in *Power Electronics and Applications, 2009. EPE '09. 13th European Conference on*. 2009.
22. Krause, P.C., *Analysis of Electric Machinery*. 1994: New York: McGraw-Hill.
23. Novotny, D.W. and T.A. Lipo, *Vectror Control and Dynamics of AC Drives*. 1996, Oxford, UK: Clarendon Press.
24. Blasco-Gimenez, R., et al., *Dynamic performance limitations for MRAS based sensorless induction motor drives. I. Stability analysis for the closed loop drive*. Electric Power Applications, IEE Proceedings -, 1996. **143**(2): p. 113-122.
25. Holtz, J. *Developments in Sensorless AC Drive Technology*. in *Power Electronics and Drives Systems, 2005. PEDS 2005. International Conference on*. 2005.
26. Hu, J. and B. Wu. *New integration algorithms for estimating motor flux over a wide speed range*. in *Power Electronics Specialists Conference, 1997. PESC '97 Record., 28th Annual IEEE*. 1997.
27. Holtz, J. and Q. Juntao, *Sensorless vector control of induction motors at very low speed using a nonlinear inverter model and parameter identification*. Industry Applications, IEEE Transactions on, 2002. **38**(4): p. 1087-1095.
28. Jansen, P.L. and R.D. Lorenz. *Accuracy limitations of velocity and flux*

estimation in direct field oriented induction machines. in *Power Electronics and Applications, 1993., Fifth European Conference on.* 1993.

29. Gao, Q., *Sensorless Vector control of Induction Machines at zero and low frequencies*, in *Electrical and Electronics Engineering.* 2006, University of Nottingham.
30. Kubota, H., K. Matsuse, and T. Nakano, *DSP-based speed adaptive flux observer of induction motor.* Industry Applications, IEEE Transactions on, 1993. **29**(2): p. 344-348.
31. Jones, L.A. and J.H. Lang, *A state observer for the permanent-magnet synchronous motor.* Industrial Electronics, IEEE Transactions on, 1989. **36**(3): p. 374-382.
32. Lascu, C., I. Boldea, and F. Blaabjerg, *Very-low-speed variable-structure control of sensorless induction machine drives without signal injection.* Industry Applications, IEEE Transactions on, 2005. **41**(2): p. 591-598.
33. Tursini, M., R. Petrella, and F. Parasiliti, *Adaptive sliding-mode observer for speed-sensorless control of induction motors.* Industry Applications, IEEE Transactions on, 2000. **36**(5): p. 1380-1387.
34. Kim, Y.R., S.K. Sul, and M.H. Park. *Speed sensorless vector control of an induction motor using an extended Kalman filter.* in *Industry Applications Society Annual Meeting, 1992., Conference Record of the 1992 IEEE.* 1992.
35. Harnefors, L. *A comparison between directly parametrised observers and extended Kalman filters for sensorless induction motor drives.* in *Power Electronics and Variable Speed Drives, 1998. Seventh International Conference on (Conf. Publ. No. 456).* 1998.
36. Armstrong, G.J., D.J. Atkinson, and P.P. Acarnley. *A comparison of estimation techniques for sensorless vector controlled induction motor drives.* in *Power Electronics and Drive Systems, 1997. Proceedings., 1997 International Conference on.* 1997.
37. Kereszty, T., V.M. Leppanen, and J. Luomi. *Sensorless control of surface magnet synchronous motors at low speeds using low-frequency signal injection.* in *Industrial Electronics Society, 2003. IECON '03. The 29th Annual Conference of the IEEE.* 2003.
38. Cilia, J., et al., *Sensorless position detection for vector-controlled induction motor drives using an asymmetric outer-section cage.* Industry Applications, IEEE Transactions on, 1997. **33**(5): p. 1162-1169.
39. Jansen, P.L. and R.D. Lorenz, *Transducerless position and velocity estimation in induction and salient AC machines.* Industry Applications, IEEE Transactions on, 1995. **31**(2): p. 240-247.
40. Teske, N., et al., *Encoderless position estimation for symmetric cage induction machines under loaded conditions.* Industry Applications,

IEEE Transactions on, 2001. **37**(6): p. 1793-1800.

41. Teske, N., Asher G.M., Bradley, K. J. and Sumner M., *Encoderless position control of induction machines*, in *EPE conference*. 2001.
42. Holtz, J., *Sensorless Control of Induction Machines-With or Without Signal Injection?* Industrial Electronics, IEEE Transactions on, 2006. **53**(1): p. 7-30.
43. Gao, Q., G. Asher, and M. Sumner, *Sensorless Position and Speed Control of Induction Motors Using High-Frequency Injection and Without Offline Precommissioning.* Industrial Electronics, IEEE Transactions on, 2007. **54**(5): p. 2474-2481.
44. A.E. Fitzgerald, C.K., and S. Umans, *Electric Machinery*. 6th edition ed. 2003: McGraw-Hill Higher Education.
45. Teske, N., *Sensorless position control of induction machines using high frequency signal injection*, in *Electrical and Electronics Engineering*. 2001, University of Nottingham.
46. Holtz, J. and P. Hangwen, *Elimination of saturation effects in sensorless position-controlled induction motors.* Industry Applications, IEEE Transactions on, 2004. **40**(2): p. 623-631.
47. Makys, P., et al. *Shaft Sensorless Speed Control of Induction Motor Drive*. in *Power Electronics and Motion Control Conference, 2006. EPE-PEMC 2006. 12th International*. 2006.
48. Linke, M., R. Kennel, and J. Holtz. *Sensorless position control of permanent magnet synchronous machines without limitation at zero speed*. in *IECON 02 Industrial Electronics Society, IEEE 2002 28th Annual Conference*. 2002.
49. Caruana, C., et al., *Flux position estimation in cage induction machines using synchronous HF injection and Kalman filtering.* Industry Applications, IEEE Transactions on, 2003. **39**(5): p. 1372-1378.
50. Yu-seok, J., et al., *Initial rotor position estimation of an interior permanent-magnet synchronous machine using carrier-frequency injection methods.* Industry Applications, IEEE Transactions on, 2005. **41**(1): p. 38-45.
51. Young-doo, Y., et al. *High bandwidth sensorless algorithm for AC machines based on square-wave type voltage injection*. in *Energy Conversion Congress and Exposition, 2009. ECCE 2009. IEEE*. 2009.
52. Young-Doo, Y., et al., *High-Bandwidth Sensorless Algorithm for AC Machines Based on Square-Wave-Type Voltage Injection.* Industry Applications, IEEE Transactions on, 2011. **47**(3): p. 1361-1370.
53. Young-doo, Y. and S. Seung-ki. *Sensorless control for induction machines using square-wave voltage injection*. in *Energy Conversion Congress and Exposition (ECCE), 2010 IEEE*. 2010.
54. Kim, S. and S.-K. Sul. *High performance position sensorless control*

using rotating voltage signal injection in IPMSM. in *Power Electronics and Applications (EPE 2011), Proceedings of the 2011-14th European Conference on.* 2011.

55. Schroedl, M. *Sensorless control of AC machines at low speed and standstill based on the INFORM method.* in *Industry Applications Conference, 1996. Thirty-First IAS Annual Meeting, IAS '96., Conference Record of the 1996 IEEE.* 1996.
56. Robeischl, E. and M. Schroedl, *Optimized INFORM measurement sequence for sensorless PM synchronous motor drives with respect to minimum current distortion.* Industry Applications, IEEE Transactions on, 2004. **40**(2): p. 591-598.
57. Holtz, J. and J. Juliet, *Sensorless acquisition of the rotor position angle of induction motors with arbitrary stator windings.* Industry Applications, IEEE Transactions on, 2005. **41**(6): p. 1675-1682.
58. Holtz, J. *Sensorless position control of induction motors. An emerging technology.* in *Advanced Motion Control, 1998. AMC '98-Coimbra., 1998 5th International Workshop on.* 1998.
59. Caruana, C., G.M. Asher, and J. Clare. *Sensorless flux position estimation at low and zero frequency by measuring zero-sequence current in delta connected cage induction machines.* in *Industry Applications Conference, 2003. 38th IAS Annual Meeting. Conference Record of the.* 2003.
60. Raute, R., et al. *A zero speed operation sensorless PMSM drive without additional test signal injection.* in *Power Electronics and Applications, 2007 European Conference on.* 2007.
61. Ki-Seon, K., J. Young-Gook, and L. Young-Cheol, *A New Hybrid Random PWM Scheme.* Power Electronics, IEEE Transactions on, 2009. **24**(1): p. 192-200.
62. Habetler, T.G. and D.M. Divan, *Acoustic noise reduction in sinusoidal PWM drives using a randomly modulated carrier.* Power Electronics, IEEE Transactions on, 1991. **6**(3): p. 356-363.
63. Paul Horowitz, W.H., *The Art of Electronics.* 1980: Cambridge University Press.
64. Holtz, J., *Acquisition of Position Error and Magnet Polarity for Sensorless Control of PM Synchronous Machines.* Industry Applications, IEEE Transactions on, 2008. **44**(4): p. 1172-1180.
65. C.Silva, G.A., and M.Sumner. *Influence of dead-time compensation on rotor position estimation in surface mounted pm machines using hf voltage injection.* in *IEEE Power Conversion Conference.* 2002.
66. J.Holtz, *Pulsewidthmodulation for electronic power conversion.* Proceeding of the IEEE, 1994. **82**: p. 1194-1214.
67. J-L.Lin, *A new approach of dead-time compensation for pwm voltage*

inverters. Circuits and Systems -I: Fundamental Theory and Applications, IEEE Transactions on, 2002. **49**(4): p. 476-483.

68. M.Linke, R.K., and J.Holtz. *Sensorless speed and position control of synchronous machines using alternating carrier injection.* in *Electrical Machines and Drives Conference*. 2003.
69. V.Szokolay, S., *Introduction to ARCHITECTURAL SCIENCE: the basis of sustainable design*. 2004: Architectural Press.
70. Standard, I., *IEC 61672*. 2003.
71. Standard, I., *ISO 226*. 2003.
72. DiracDelta.co.uk. *A Weighting*.
73. Testo, *Testo 816 Sound Level Metre Instruction Manual*.
74. Crocker, M.J., ed. *Handbook of noise and vibration control*. 2007, Hoboken, N.J. : John Wiley & Sons.
75. de Lillo, L., et al., *Multiphase Power Converter Drive for Fault-Tolerant Machine Development in Aerospace Applications.* Industrial Electronics, IEEE Transactions on, 2010. **57**(2): p. 575-583.
76. Inc, S.D. *TMS320C6713 DSK Technical Reference*. May 2003.
77. Educational DSP, L. http://www.educationaldsp.com/.
78. Wu, B., *High-Power Converters and AC Drives*. 2006, Wiley & IEEE Press.
79. Mohan, N., Undeland, T. M. , Robbins, W. P. , ed. *Power Electronics: Converters, Applications, and Design*. 3rd ed. 2002, John Wiley & Sons.
80. Gerada, C., et al. *Loading effects on saliency based sensorless control of PMSMs.* in *Electrical Machines and Systems, 2009. ICEMS 2009. International Conference on*. 2009.
81. Yi, L., et al., *Improved Rotor-Position Estimation by Signal Injection in Brushless AC Motors, Accounting for Cross-Coupling Magnetic Saturation.* Industry Applications, IEEE Transactions on, 2009. **45**(5): p. 1843-1850.
82. Guglielmi, P., M. Pastorelli, and A. Vagati, *Cross-Saturation Effects in IPM Motors and Related Impact on Sensorless Control.* Industry Applications, IEEE Transactions on, 2006. **42**(6): p. 1516-1522.
83. LeCroy, *Current probes*. 2005.
84. LeCroy, *WaveSufer 400 Series*. 2006.